The Relationship Between Marine Aerosol Particles and Satellite-Detected Radiance

By
Philip A. Durkee

Department of Atmospheric Science
Colorado State University
Fort Collins, Colorado

Department of Atmospheric Science

Paper No. 380

THE RELATIONSHIP BETWEEN MARINE AEROSOL PARTICLES AND SATELLITE-DETECTED RADIANCE

by

Philip A. Durkee

Department of Atmospheric Science

Colorado State University

Fort Collins, CO 80523

May, 1984

Atmospheric Science Paper No. 380

This paper was also submitted in partial fulfillment of the requirements for the Degree of Doctor of Philosophy.

ABSTRACT

Brightness variations in satellite images of cloud-free, ocean regions have been hypothesized to be caused by marine aerosol particle variations. The objective of this dissertation is to quantitatively examine the relationship between marine aerosol particles and satellite-detected radiance. Further, the causes of particle variations which lead to upwelling radiance variation, particularly relative humidity effects, are investigated.

Both theoretical and experimental approaches are taken to attain these objectives. First, a two-stream radiative transfer model is used to calculate upwelling radiance variations caused by calculated aerosol particle variations. Variations of particle scattering characteristics due to composition, total number (due to wind speed variation), and size (due to relative humidity variation) are investigated.

Second, an experiment designed to relate near-simultaneous satellite images to marine boundary layer characteristics was conducted off shore of southern California from 20 September to 7 October, 1982. Satellite images were analyzed in real-time and used to direct an aircraft to regions of brightness variations detected in the images. The aircraft measured atmospheric state variables and aerosol particle characteristics in the regions of interest. This set of measurements is used to compare satellite-detected radiance with known aerosol particle characteristics and atmospheric state variables.

From the theoretical and experimental results it is concluded that satellite-detected radiance is positively correlated with aerosol optical depth. Also, marine boundary layer radiative extinction is related to relative humidity. Therefore, since satellite-detected

radiance is related to total extinction (optical depth) and extinction is related to relative humidity, satellite-detected radiance is related to relative humidity.

The relationship between boundary layer relative humidity and satellite-detected radiance is limited by significant numbers of particles above the boundary layer. Upper level particles are shown to result from a mixture of marine, terrestrial and possibly urban sources. Due to composition and size distribution differences, the wavelength dependence of the particle scattering characteristics is greater for situations influenced by upper level particles than those where only marine particles are present. Following this reasoning, the ratio of satellite-detected radiance at red and near infrared wavelengths is shown to detect the presence of significant amounts of upper level particles.

ACKNOWLEDGEMENTS

The author wishes to thank Professor Thomas H. Vonder Haar for his support and advice throughout this study. Professors Thomas B. McKee and James A. Smith, and Dr. Richard Pearson are thanked for their service as committee members and for their careful review of this dissertation.

Miss Loretta Stevens is thanked for her patient typing and processing of the manuscript. Also, for drafting of many of the figures, Judy Sorbie is thanked.

The author wishes to specially thank Dr. Edward E. Hindman for his efforts in planning and execution of the experiment, and for his particle composition analysis. Dr. Hindman also contributed greatly to the review of the text.

The collaboration with the Ocean and Atmospheric Sciences Division of the Naval Ocean Systems Center, and particularly the careful work of Dr. Douglas R. Jensen in executing the aircraft measurements, is gratefully acknowledged. Also, Gibbs Flying Service and J. B. Milton, our pilot, are acknowledged for support that made the aircraft measurements possible.

The members of the Scripps Institute of Oceanography Satellite Oceanography Facility, particularly Mr. Robert Whritner, are thanked for their support in collection and analysis of the satellite imagery. Also, Mr. Robert W. Fett of the Naval Environmental Prediction Research Facility is thanked for his inspiration and guidance at the initiation of this study.

This research was sponsored by ONR Contract No. N00014-C-79-0793 administered through the Research Institute of Colorado, Fort Collins, CO.

TABLE OF CONTENTS

TABLE OF CONTENTS
(cont.)

LIST OF FIGURES

LIST OF TABLES

1.0 INTRODUCTION

Recent improvements in the sensitivity of satellite-borne visible-wavelength sensors have made it possible to detect variations in aerosol optical depth from space. Griggs (1979) has shown a positive relationship between aerosol optical depth measured by surface-based sun photometers, and upwelling radiance measured by the Landsat satellite. Further, Carlson, et al. (1979) and Norton, et al. (1980) have investigated the relationship between satellite-detected upwelling radiance and desert aerosol particles advected off the African coast. They have shown that turbidity can be mapped when the aerosol optical depth is large.

Clouds typically have an albedo of 60 to 80% and are easily seen in satellite images against the earth's surface albedo of 5 to 40%. Aerosol optical depth variations, however, result in albedo variations of tenths to a few percent (Griggs, 1979). The meteorological satellites have been primarily designed to detect clouds so that their sensitivity to low albedo scenes is small. It is, therefore, stretching these sensors to their limits to use them for detection of aerosol optical depth variations.

The various meteorological satellite sensors differ in their abilities to detect aerosol variations. Koepke and Quenzel (1979) and Koepke and Quenzel (1981) discuss the optimal view geometrics and radiation wavelengths for measuring aerosol optical depths. From these results and information on sensor response characteristics, Durkee, et

al. (1982) have summarized the ability of the meteorological satellites to detect marine aerosol particle variations.

Fett and Isaacs (1979) first described brightness variations, termed 'anomalous gray-shades', observed in DMSP (Defense Meteorological Satellite Program) images of marine environments. These 'anomalous gray-shades' where hypothesized to be caused by variations of aerosols in the marine boundary layer. They concluded from simple calculations that marine aerosol variations affect the reflection of solar irradiance. Patterns of the brightness variations were related to cloud edges, island wakes, etc. where aerosol variations could be expected.

Variation of relative humidity was thought by Fett and Isaacs (1979) to be the main cause of the aerosol variations which result in 'anomalous gray-shades'. Appendix A presents a high amplitude, regional scale brightness variation which corresponded to boundary layer humidity variation during Santa Ana conditions off the coast of southern California. Isaacs (1980) theoretically investigated the effect of low-level haze on DMSP imagery and found the initial hypothesis to be plausible; that aerosol variations resulting from relative humidity variations significantly affect upwelling radiance. To this point, no direct measurements had yet been made to link known relative humidity and aerosol variations with satellite-detected brightness variations.

In 1980, the apparent relationship between aerosol variations and coincident satellite-detected brightness variations was tested using near-simultaneous satellite and boundary layer measurements. Hindman, et al (1984) describe these experiments. A positive relationship was found between measured aerosol particle variations in the marine boundary layer and satellite-detected brightness variations. Only a few

cases were collected, however, so that firm conclusions could not be drawn.

1.1 Objectives.

The first objective of this study is to characterize and understand the relationship between aerosol particles and satellite-detected upwelling radiance in the marine environment. The relationship will be investigated theoretically as well as with near-simultaneous satellite and aerosol measurements.

The theoretical relationship will be examined with simple radiative transfer calculations. A single-scattering model will be used to identify the important radiative parameters. Variations of upwelling radiance caused by these parameters will be described using a two-stream approximation described by Kaufman (1979) and Isaacs (1980).

In 1982, a second set of aircraft flights were made in conjunction with the Ocean and Atmospheric Sciences Division at the Naval Ocean Systems Center (NOSC). These flights were made coincident with overpasses of the NOAA-7 Advanced Very High Resolution Radiometer (AVHRR) and the NIMBUS-7 Coastal Zone Color Scanner (CZCS). A total of 10 aircraft flights were executed between 20 September and 7 October, 1982. The aircraft was equipped to measure sizes, numbers and composition of aerosol particles and atmospheric state variables. The resulting relationship between measured aerosol properties and satellite-detected radiance will be presented.

The second objective of this study is to determine the impact of relative humidity variations on aerosol particle variations and subsequent variations of upwelling radiance. If a relationship between relative humidity and the scattering characteristics of marine particles

holds, satellite-detected radiance may be used to remotely sense relative humidity variations within the marine boundary layer. Investigations of relative humidity variations would then be possible at high temporal and spacial resolution.

To persue these objectives, it must be understood that the distribution of aerosol particles can vary in three ways to affect a change in reflected solar irradiance. First, an increase in relative humidity causes marine particles to grow. The growth will result in more large particles and an increase in light scattering. Second, a source of new particles, increases the total number of particles, thus increasing the scattered light. Third, a difference in the composition of the particles results in a different index of refraction of the particles and thus different scattering characteristics.

The variation of upwelling radiance resulting from these three variations are theoretically calculated and compared. Also, the abilities of the NOAA-7 AVHRR and NIMBUS-7 CZCS to measure the resulting radiance variations are determined. Results from aircraft measurements are used to test the relationship between aerosol growth and relative humidity. Further, aerosol variations due to local sources and different compositions of particles were found from the aircraft measurements. Finally, relative humidity, particle sources and composition variations, are shown to relate to satellite-detected upwelling radiance.

1.2 Organization.

In Chapter 2, the theory of solar radiative transfer in the presence of marine particles is presented. The dependence of particle size, number and composition on scattered radiance is examined.

Further, the effect of relative humidity on particle characteristics is discussed.

In Chapter 3, the experimental plan and procedures are described. The details of the satellite and aircraft measurement systems are presented. Also, procedures are developed for calculation of the critical scattering characteristics of the measured particles.

The results of the field experiment are presented in Chapter 4. Relationships between relative humidity and aerosol optical depth, and aerosol optical depth and satellite-detected radiance are developed and discussed.

In Chapter 5, the conclusions drawn from the experimental results are summarized. Also, the uses of these results to characterize the marine boundary layer via satellite-detected radiance are discussed.

2.0 THEORY AND MECHANISMS

The cloud-free, marine environment presents a manageable solar-radiation transfer problem; especially in the presence of a subsidence-induced, low-level inversion. The radiation field is influenced by molecular (Rayleigh) scattering throughout the atmosphere, but aerosol (Mie) scattering is often confined to the marine boundary layer. Also, at red-visible to near-infrared wavelengths the ocean surface albedo is nearly zero; away from regions of turbid water and sunglint (described in Section 3.4.2). Therefore, satellite-detected upwelling radiance is determined by a combination of Rayleigh scattering, Mie scattering by particles within the boundary layer and a small contribution from sea-surface reflectance.

Rayleigh scattering depends on the concentration of molecular constituents within the atmosphere. Away from strong temperature or pressure gradients, molecular constituents do not vary horizontally. Mie scattering depends on sizes and numbers of aerosol particles which can exhibit large horizontal variations due to sources of particles and relative humidity fluctuations (to be descried in Section 2.3). Therefore, since sea-surface reflection is small, horizontal variations of upwelling radiance are normally caused by variations of particles below the inversion.

In this chapter, a theoretical framework to predict upwelling radiance caused by aerosol particle variations is developed. This requires a brief discussion of general radiative transfer. From this

discussion, an approximation for single scattering is used to identify the important radiative parameters for the marine environment. Finally, a two-stream radiative transfer model (Kaufman, 1979 and Isaacs, 1980) is used to examine the variation of upwelling radiance causd by alterations of the particle scattering characteristics. The variation of marine particle size caused by changes in relative humidity will be shown to be the dominant contributor to variations of satellite-detected radiance.

2.1 Radiative Transfer in a Marine Environment.

The general form of the radiative transfer equation for scattering of solar radiation in a plane parallel atmosphere is as follows (Liou, 1980):

$$\mu \frac{dL(\tau,\Omega)}{d\tau} = L(\tau,\Omega) - \frac{\tilde{\omega}}{4\pi}\int_{4\pi} L(\tau,\Omega')p(\Omega,\Omega')d\Omega' - \frac{\omega_o}{4\pi}\pi F_o\, p\,(\Omega,-\Omega_o)\, e^{-\tau/\mu_o} \qquad (2.1)$$

where

L = diffuse intensity or radiance

τ = optical depth

ω_o = single scattering albedo

μ = $\cos\theta$ (θ = observation zenith angle)

μ_o = $\cos\theta_o$ (θ_o = solar zenith angle)

$\underset{\sim}{\Omega}$ = solid angle (θ,ϕ) (ϕ = azimuth angle)

$p(\underset{\sim}{\Omega},\underset{\sim}{\Omega}')$ = scattering phase function in scattering from solid angle $\underset{\sim}{\Omega}'$ to $\underset{\sim}{\Omega}$

πF_o = incoming radiative flux.

The first term on the right side of Equation (2.1) accounts for the intensity absorbed or scattered from the beam. The second term

describes the intensity added to the beam by multiple scattering from all directions into the solid angle Ω. The third term is the contribution of singly scattered intensity.

For satellite applications, Equation (2.1) must be solved at the top of the atmosphere. Given the geometry of the sun-earth-satellite system the necessary imputs to Equation (2.1) for solution are the optical depth, single scattering albedo, and scattering phase function. These inputs are derived from knowledge of the scattering medium as follows.

In a cloud-free marine environment the scattering medium is often dominated by surface-generated aerosol particles. Given the size distribution of these particles, the extinction and scattering coefficients (in units of per length) are defined as

$$\beta_{ext} = \int_0^\infty \pi r^2 \, Q_{ext}(m,r) \, \frac{dN(r)}{dr} \, dr$$
$$\beta_{scat} = \int_0^\infty \pi r^2 \, Q_{scat}(m,r) \, \frac{dN(r)}{dr} \, dr \qquad (2.2)$$

where Q_{ext} and Q_{scat} are the extinction and scattering efficiencies of a particle with radius r and complex index of refraction ($m = k - i\lambda$) and $dN(r)/dr$ describes the size distribution of the particles. Using Equation (2.2) the vertical optical depth is defined as

$$\tau = \int_0^H \beta_{ext} dz \qquad (2.3)$$

and is just the sum of the extinction coefficient from the surface to satellite altitude H.

As seen in Equation (2.2), the extinction coefficient is the sum of the product of three terms; the cross-sectional area (πr^2), the

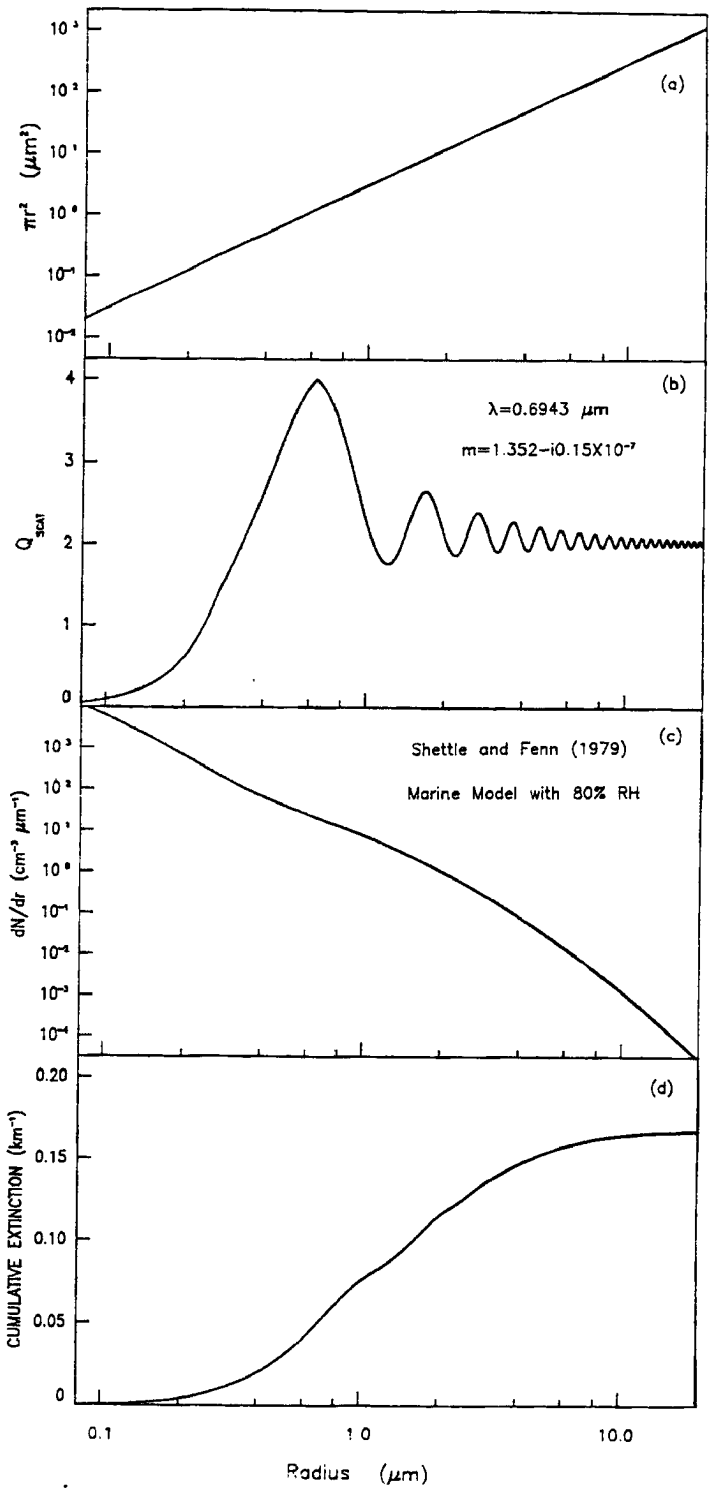

Figure 2.1 The terms from the extinction calculation of Equation (2.2) as a function of radius: (a) πr^2, the cross sectional area; (b) Q_{scat}, the scattering efficiency of sea-salt particles at $\lambda = 0.6943$ μm; (c) dN/dr, the size distribution of marine particles at 80% relative humidity after Shettle and Fenn (1979); (d) cumulative extinction with increasing radius.

extinction efficiency (Q_{ext}) and the size distribution (dN/dr). Figure 2.1 shows these terms as a function of radius for a model distribution of marine particles at 80% RH (Shettle and Fenn, 1979). At small radius, πr^2 and Q_{ext} values are small and values of dN/dr are large. Conversely, πr^2 becomes large at large radius and dN/dr becomes small. The result of these characteristics is a bounded range of particle sizes which contribute to the extinction coefficient. The cumulative sum of the terms in Equation (2.2) is shown in Figure 2.1d. Where the cumulative sum has slope, the particles at that radius contribute to the extinction. The area of largest slope in Figure 2.2 indicates the particles which contribute the most to the extinction coefficient. For this case, these are the 0.5 to 5.0 μm radius particles which account for 67% of the extinction.

Absorption by particles is controlled by the complex part of the index of refraction, \). For marine particles \) is less than 10^{-4} at wave lengths less than 1 μm (Shettle and Fenn, 1979). Therefore, β_{ext}, which is the sum of extinction by scattering and absorption, is nearly equal to β_{scat}. The single scattering albedo, defined as $\omega_o = \beta_{scat}/\beta_{ext}$, is therefore nearly 1 for marine aerosol particles; they are efficient scatterers.

The scattering phase function $p(\theta)$ describes the angular distribution of radiation scattered by particles. If the particles are spherical, Mie scattering theory can be used to calculate $p(\theta)$. Figure 2.2 shows $p(\theta)$ for the model of marine particles at 80% RH used to construct Figure 2.1 (Shettle and Fenn, 1979). A scattering angle of 0^o

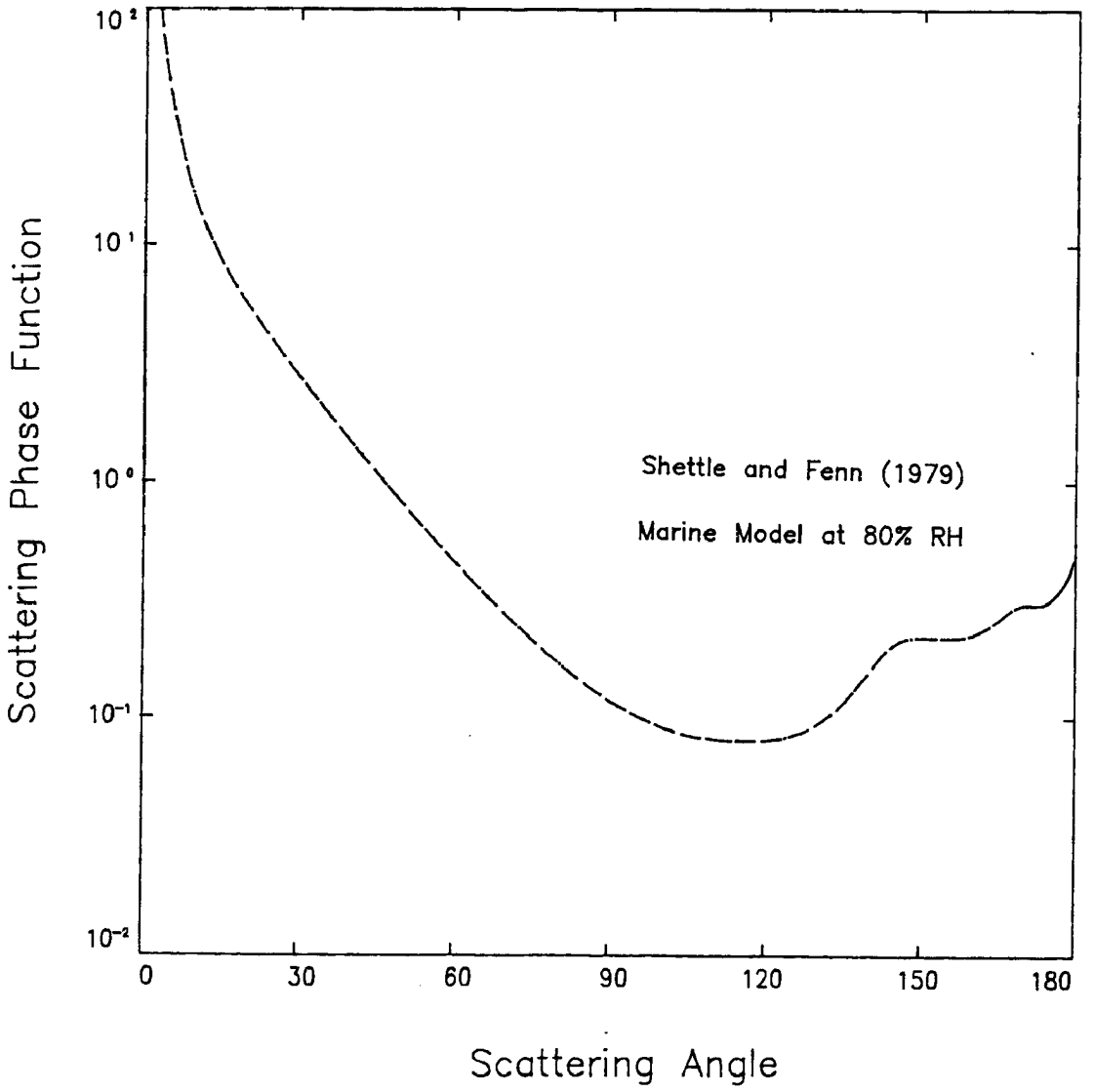

Figure 2.2 **The single scattering phase function for the model of marine particles at 80% relative humidity after Shettle and Fenn (1979).**

corresponds to forward scattering, while a 180^{o} scattering angle corresponds to backward scattering. From Figure 2.2, it is clear that marine particles scatter primarily in the forward direction.

2.2 Single Scattering Solution of the Radiative Transfer Equation.

The difficulty in solving Equation (2.1) arises in the multiple scattering term. This term is an integration over all wavelengths of the intensity field. Therefore, a prior knowledge of the intensity field is needed to solve Equation (2.1) for the upwelling radiance. Solution of Equation (2.1) requires either numerical techniques or an approximation of the multiple scattering term.

In the single scattering approximation, incident solar radiation is considered as the only intensity source and the intensity field due to single scattering of the source is calculated. If we consider the radiation which is scattered only once by marine aerosols, the radiative transfer equation for the upward intensitites becomes (Liou, 1980)

$$L(\tau;\mu,\phi) = L(\tau_1;\mu,\phi)\, e^{-(\tau_1-\tau)/\mu} + \frac{\omega_o}{4\pi}\pi F_o\, p(\mu,\phi;-\mu_o,\phi_o) \int_{\tau}^{\tau_1} \exp\{-[(\tau'-\tau)/\mu + \tau'/\mu_o]\}d\tau'/\mu \tag{2.4}$$

If we assume that the upward intensity at the bottom of the atmosphere, $L(\tau_1;\mu,\phi)$, is zero, then from Equation (2.4) the reflected intensity for a finite atmosphere with a total optical depth of τ_1, is

$$L(0;\mu,\phi) = \frac{\omega_o \mu_o F_o}{4(\mu+\mu_o)}\, p(\Theta)\{1-\exp[-\tau_1(\frac{1}{\mu}+\frac{1}{\mu_o})]\} \tag{2.5}$$

For a given geometry in Equation (2.5), the reflected intensity is directly proportional to the phase function, $p(\Theta)$, where Θ is the single scattering angle.

The single scattering approximation applies for atmospheres with small optical depths. If $\tau_1(\frac{1}{\mu} + \frac{1}{\mu_o}) \ll 1$, Equation (2.5) reduces to

$$L(0;\mu,\varphi) \simeq \frac{\omega_o F_o}{4\mu} P(\Theta)\tau_1 \qquad (2.6)$$

It is clear from Equation (2.6) that the reflected intensity due to single scattering by an optically thin atmosphere is a nearly linear function of τ_1. Since $\omega_o \sim 1$, the slope of the relationship depends on $p(\Theta)$ and the satellite view geometry through μ.

2.3 Effects of Particle Characteristics on Upwelling Radiance.

It is clear from Equation (2.2) that the characteristics of particles can vary in three ways to affect the extinction coefficient. First, the composition of particles may change, which changes the index of refraction and the value of Q_{ext}. Second, the size distribution of particles may change by a change of the total number of particles. Third, a change of the size of the particles may change the size distribution.

In this Section, the effect of the three variations of particle characteristics on upwelling radiance is presented. First, the effect of composition change on the scattering efficiency of particles is discussed. Second, the effect of variations of the total number of particles is described. The magnitude of variations of particle numbers due to wind speed variations will be estimated. Third, the effect of relative humidity on particle size and composition is examined and the subsequent effect on upwelling radiance calculated.

A two-stream radiative transfer routine is used to calculate upwelling radiance in this section. The two-stream approximation

simplifies the diffuse intensity field into an upward and downward stream of radiation (two-streams). Equation (2.1), then, becomes a set of two integro-differential equations in two unknowns; the upward and downward diffuse intensity. The solution of the two-stream approximation reduces to analytical expressions, which results in small computation requirements.

Various approaches to the two-stream approximation have been applied to optically thin atmospheres (Meador and Weaver, 1978). Kaufman (1979) has modified a scheme by Coakley and Chylek (1975) to account for azimuth and zenith angular dependence. Isaacs (1980) has used this method to investigate the effect of marine haze on DMSP imagery. In this section, the method described by Kaufman (1979) and Isaacs (1980) is used to calculate upwelling radiance. The geometry used in the calculations presented in this section was the average geometry of the experiment described in Chapter 3, (satellite zenith angle, $\theta = 40^{o}$; solar zenith angle, $\theta_{o} = 45^{o}$; relative azimuth, $\phi - \phi_{o} = 70^{o}$).

2.3.1 Composition Effects.

The real part of the index of refraction, k, designates the intensity of reflection by a medium. At visible to near-infrared wavelengths, k ranges from 1.53, for dust-like substances, to 1.33, for pure water (Shettle and Fenn, 1979). Figure 2.3 shows the resulting variation of upwelling radiance values as a function of k. The size distribution was held constant so that all variation of radiance in Figure 2.3 is due to composition variation. The sensitivity of the AVHRR and CZCS sensors are also shown in Figure 2.3. The sensitivity is defined as the change in radiance which results in one brightness count

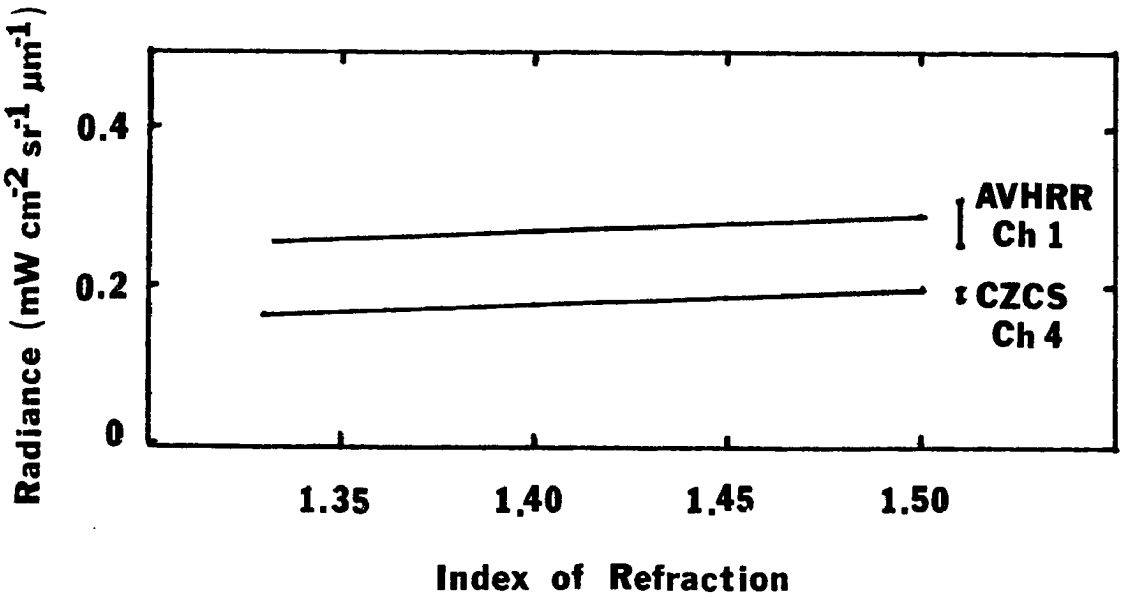

Figure 2.3 Variation of upwelling radiance as a function of the real part of the index of refraction. The size distribution is held constant. The sensitivities of the AVHRR and CZCS sensors, defined as the change of radiance which results in one brightness count change, are also shown.

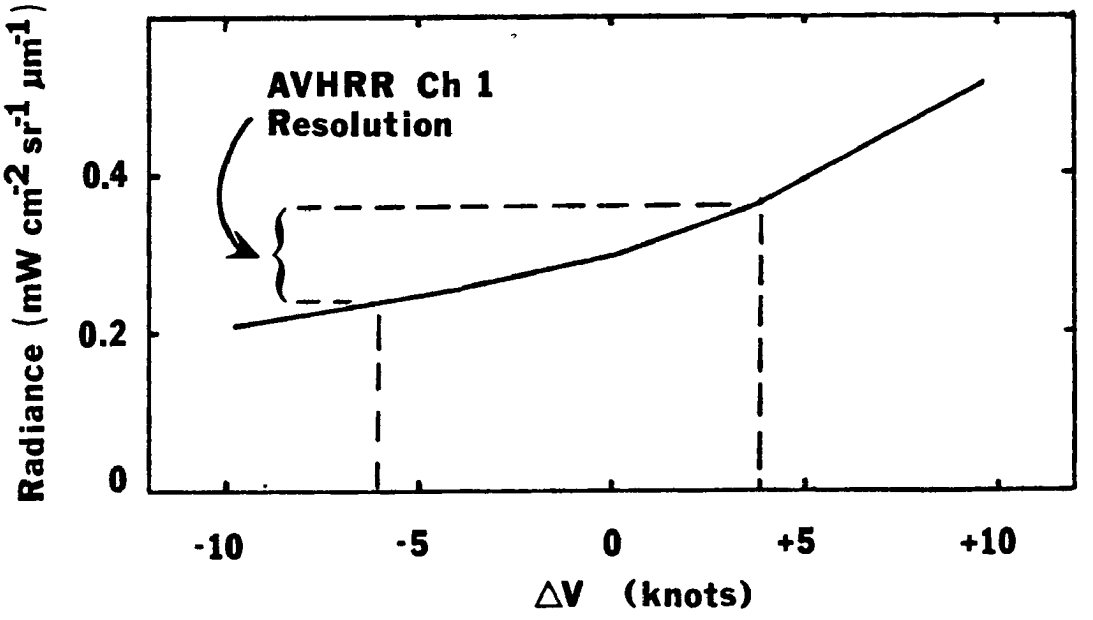

Figure 2.4 Upwelling radiance variation for particle size variations which result from wind speed variations according to Equation (2.7) ($\Delta v = v - v_o$).

change. It can be seen from Figure 2.3. that particle composition variations cause small variations in upwelling radiance relative to the sensitivity of the AVHRR and CZCS sensors. That is, the sensors cannot detect upwelling radiance variations due to the most drastic variations in the real part of the complex index of refraction.

The single scattering albedo, ω_o, depends on the complex part of the index of refraction, \). For materials which are found in aerosols, \) varies over many orders of magnitude; from 0.5 for soot to 10^{-8} for pure water. Therefore, ω_o will vary greatly with particle composition. As discussed in Section 2.1, $\omega_o \sim 1$ for marine particles. For the Shettle and Fenn (1979) model of urban aerosols (contains 20% soot particles), $\omega_o \sim 0.6$-0.7. Since ω_o is a direct multiplier in Equation 2.5, a 30-40% drop in ω_o will decrease the upwelling radiance by 30-40%. The effect of non-conservative scattering ($\omega_o < 1$) will be discussed in terms of experimental results in Chapter 4.

2.3.2 Particle Source Effects.

Aerosol particles within the marine boundary layer are primarily generated near the sea surface when wind-generated bubbles burst and the subsequent droplets evaporate (Woodcock, 1953). The total number of marine aerosol particles is, therefore, dependent on windspeed. In addition, β_{scat}, τ_A and thus, upwelling radiance, should be dependent on windspeed.

The Shettle and Fenn (1979) aerosol models can be modified for wind speed effects. Following Lovett (1975), Shettle and Fenn (1979) suggest

that the total number of particles be adjusted for wind speed by the relation:

$$N(v) = N(v_o) \exp [0.16(v-v_o)] \qquad (2.7)$$

where v_o is the initial wind speed and v is the new wind speed. The prevailing wind speed should be used in Equation (2.7) rather than an instantaneous value since marine aerosols have a lifetime of several days.

The variations in N(v), when applied to Equations (2.2) and (2.3), lead to optical depth variations. Upwelling radiance was then calculated for the variations in optical depth. Figure 2.4 shows the results of calculating upwelling radiance for various particle number variations which result from wind speed variations ($\Delta v = v-v_o$) according to Equation (2.7). The Shettle and Fenn (1979) marine model at 80% relative humidity was used as the base size distribution (applies at $\Delta v = 0$). The sensitivity of the AVHRR channel 1 sensor, shown in Figure 2.4, is a bound for determining the change in wind speed which will result in a detectable change in upwelling radiance. It can be seen from Figure 2.4 that a prevailing wind speed variation of 4 to 6 knots is necessary to cause a change in the size distribution which would be expected to result in a detectable variation of upwelling radiance.

Isaacs (1980) showed with theoretical calculations that DMSP-detected upwelling radiance depends on surface wind speed. However, he showed that typical radiance variations due to wind speed were less than those due to relative humidity variations.

2.3.3 Relative Humidity Effects.

Fett and Isaacs (1979) hypothesized that certain satellite-detected brightness variations may be caused by variations of sizes and numbers of marine aerosol particles. Particle size can change significantly when relative humidity varies if the particle is composed of water soluble material (Hänel, 1976). Since, as described above, marine aerosol particles result from evaporating droplets, they are therefore composed primarily of water soluble material.

Figure 2.5 shows results of measurements and calculations of particle growth for increasing relative humidity from Fitzgerald, et al. (1979). From Figure 2.5 it is seen that as relative humidity reaches about 80%, particle size depends strongly on relative humidity. Figure 2.6 is a composite of nephelometer measurements of aerosol scattering coefficient variation due to relative humidity variation from Fitzgerald, et al. (1982). From Figure 2.5 it is demonstrated that relative humidity increase causes particle size increase which, in turn, enhances the scattering ability of the particle population as demonstrated in Figure 2.6.

Figure 2.7 shows the variation of the marine model size distribution of Shettle and Fenn (1979) with relative humidity. Since $n(r) = dN/dr$ is a decreasing function with increasing radii, as all particles grow the number at a given radius increases. As particles grow with relative humidity, their composition also changes; their index of refraction approaches that of water. The real part of the index of refraction of sea salt and pure water is about 1.49 and 1.33, respectively. Therefore, as relative humidity increases the real part of the index of refraction decreases. The scattering efficiency of a

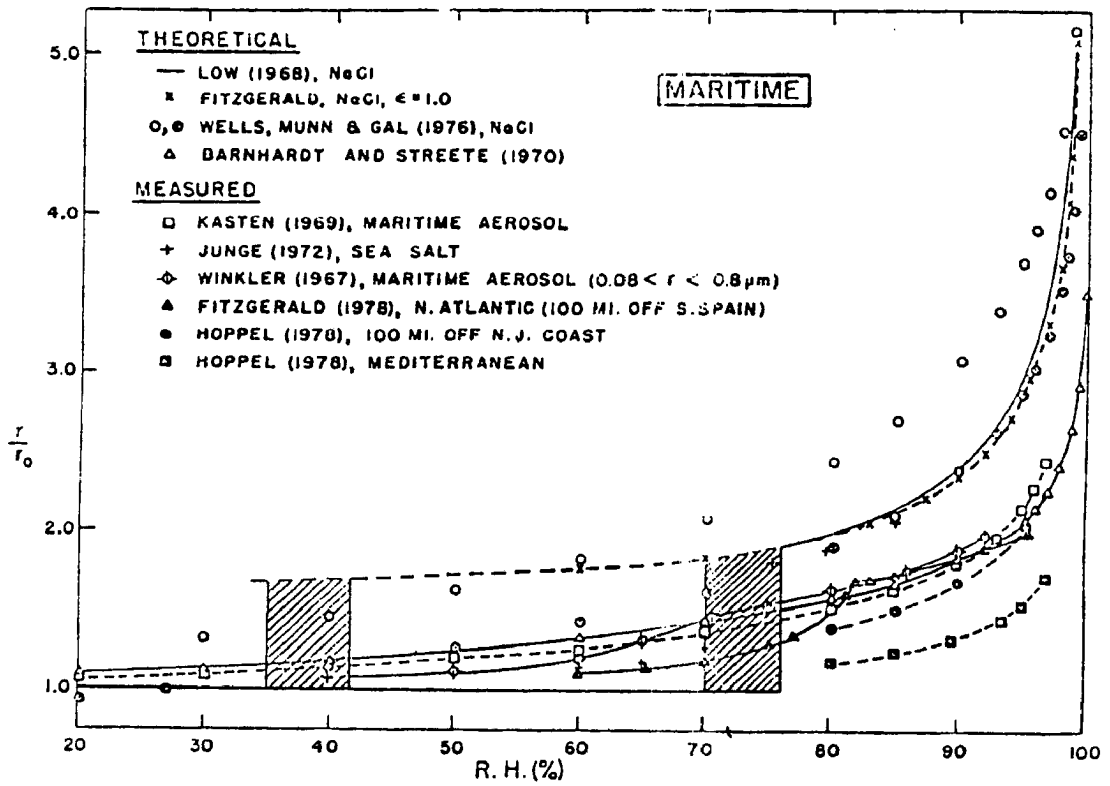

Figure 2.5 Measurements and calculations of particle growth for increasing relative humidity from Fitzgerald, et al (1979).

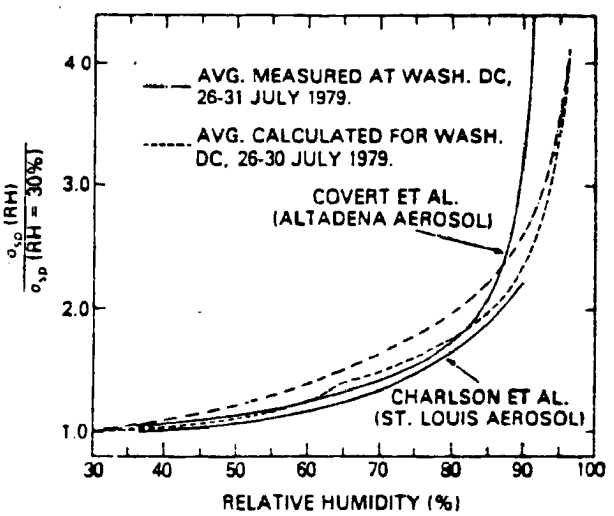

Figure 2.6 Composite of nephelometer measurements of aerosol scattering coefficient variation due to relative humidity variation from Fitzgerald, et al (1982).

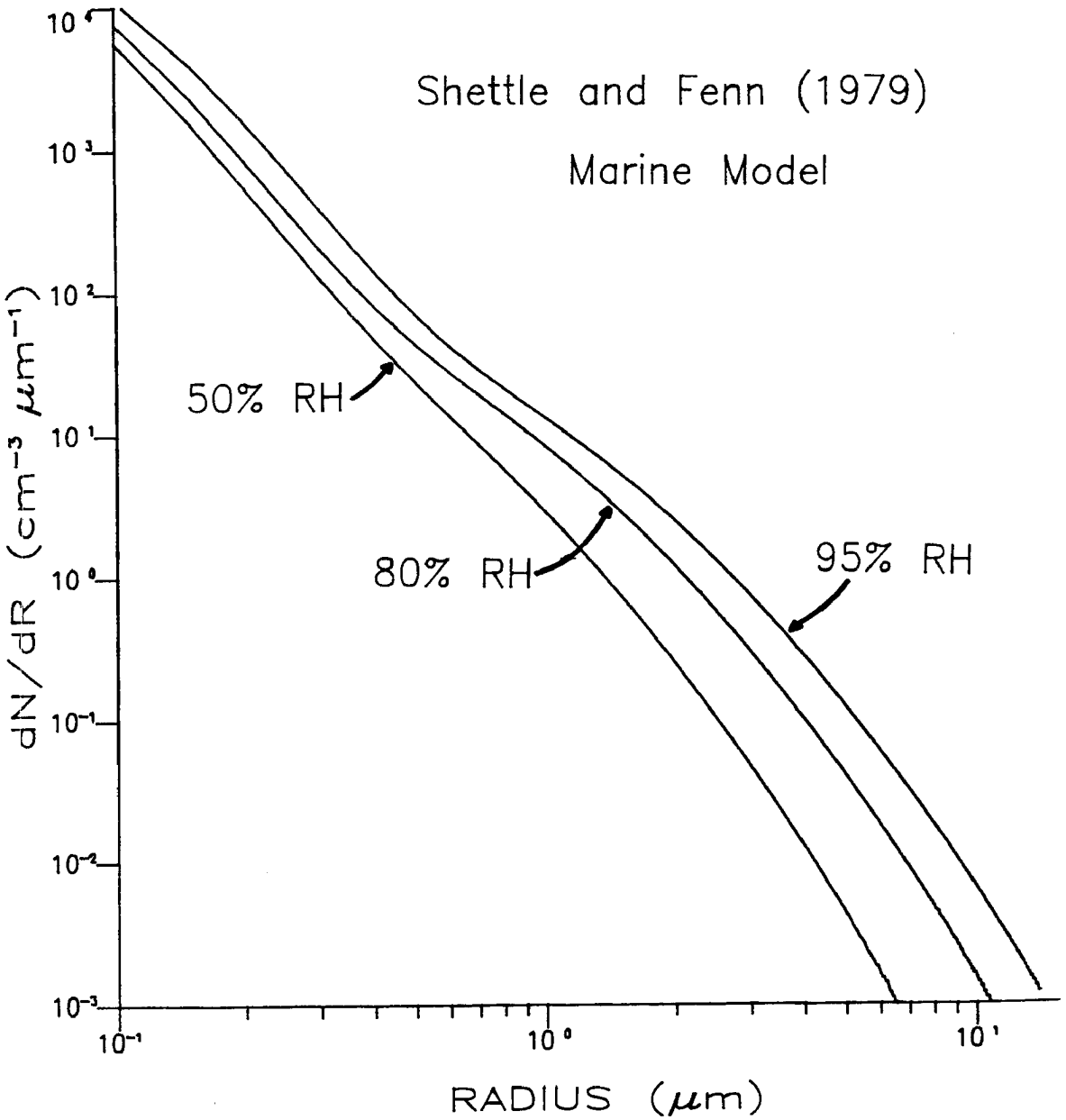

Figure 2.7 **Variation of the marine model size distribution of Shettle and Fenn (1979) with relative humidity.**

Table 2.1 Scattering Coefficient vs. Relative Humidity
$\lambda = 0.694$

	50% RH	80% RH	95% RH
β_{scat}	0.059	0.183	0.379

medium is described by the real part of the index of refraction. So the effect of increasing relative humidity, and thus, the water content of the particles, is to decrease the scattering efficiency of the particles. However, from Section 2.3.1, the effect on upwelling radiance of composition variation is small.

Table 2.1 lists the extinction coefficients for the size distributions shown in Figure 2.7. The affects of increasing the size of particles and decreasing the scattering efficienty with increasing relative humidity are accounted for. From Table 2.1, as relative humidity increases, the extinction coefficient and thus, optical depth, increase. Therefore, the affect of size increase with relative humidity must be larger than the affect of decreasing scattering efficiency.

From Equation 2.6, an increase of optical depth implies that the upwelling radiance should increase. However, due to the size distribution change with relative humidity, $p(\theta)$ also changes. Figure 2.8 shows $p(\theta)$ variation with relative humidity, calculated from the Shettle and Fenn (1979) model size distributions. At side angles and most backward angles of scatter, $p(\theta)$ decreases slightly with increasing relative humidity. This affect is due to the change in particle size with relative humidity. As particle size increases, the scattering function becomes more forward peaked. As particle size decreases, the scattering function should approach that of Rayleigh scattering (when particles are much smaller than the wavelength of light). The Rayleigh phase function is also shown in Figure 2.8.

From Table 2.1, a change in relative humidity from 50% to 95% causes nearly an order of magnitude change in β_{ext}. The largest change in $P(\theta)$ seen in Figure 2.8 between the 50% and 95% curves is less than a

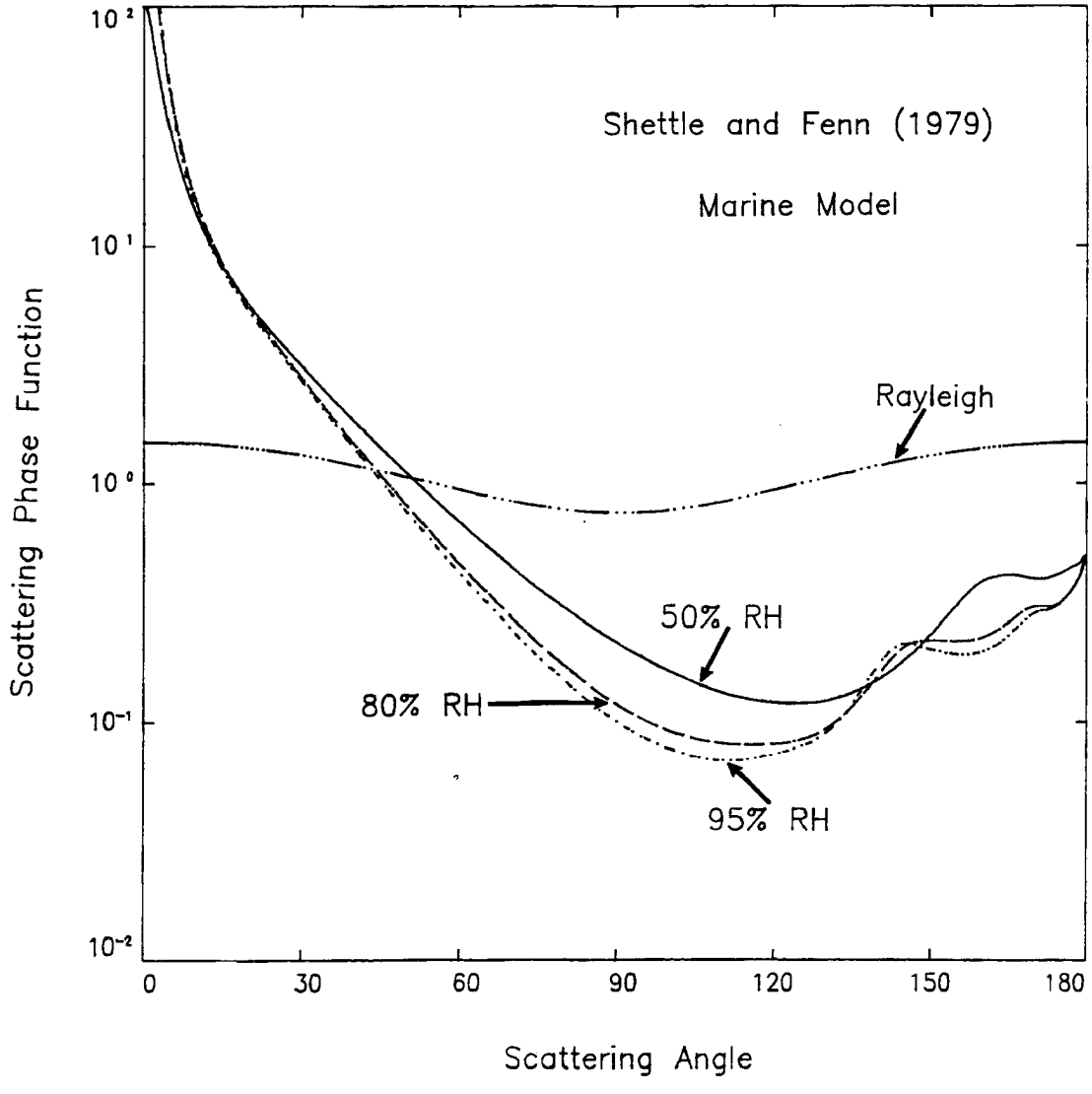

Figure 2.8 **Single scattering phase function variation with relative humidity, calculated from the Shettle and Fenn (1979) model size distributions shown in Figure 2.7.**

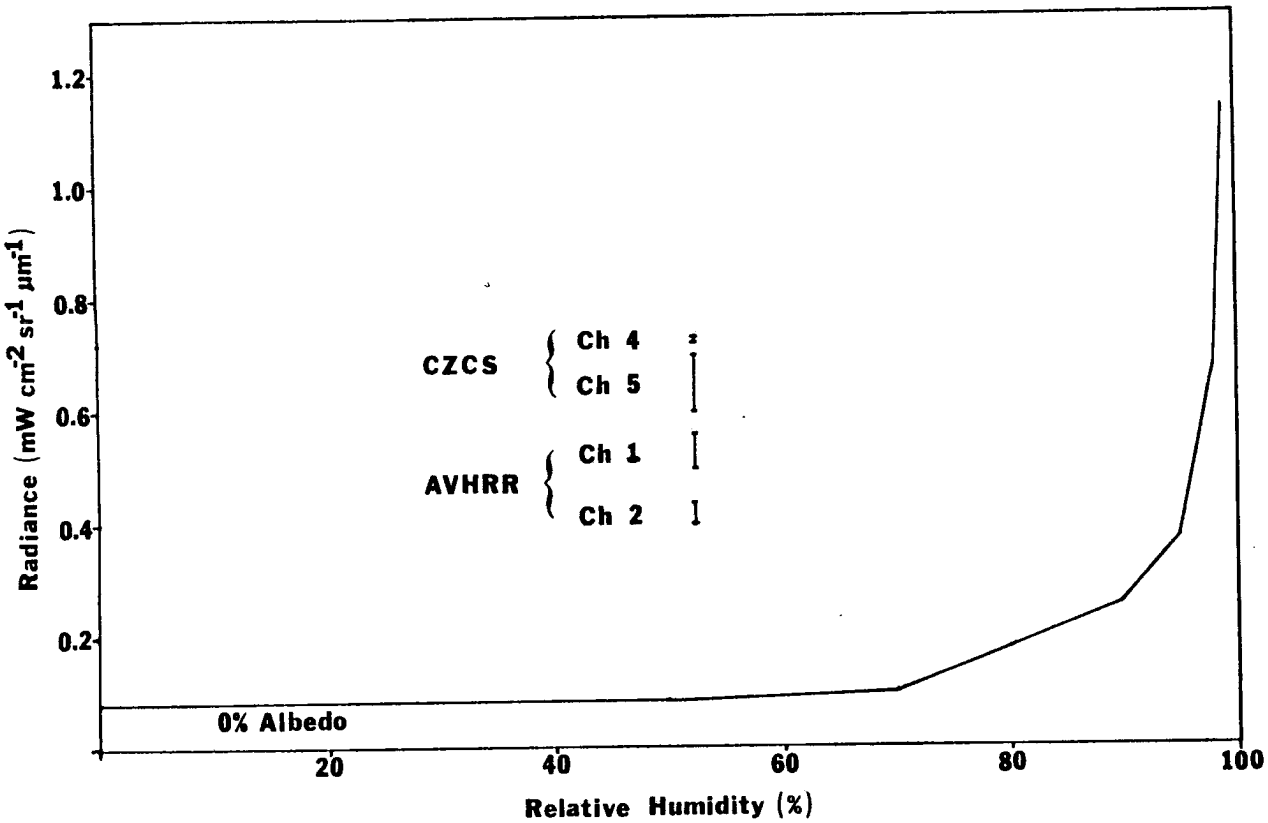

Figure 2.9 Variations of upwelling radiance as a function of relative humidity.

factor of 2. Therefore, although at some scattering angles the affect of increasing relative humidity is reduced by a decrease in $p(\theta)$, the increase of β_{ext} with increasing relative humidity is large enough to increase upwelling radiance.

Figure 2.9 shows upwelling radiances as a function of relative humidity for the average sun-earth-satellite geometry of the experiment to be described in Chapter 3. The radiances were calculated using the two-stream routine described by Kaufman (1979) and Isaacs (1980). The effects of increasing particle size and decreasing refractive index with increasing relative humidity are accounted for in the calculations. The sensitivity of the AVHRR and CZCS sensors are also shown in Figure 2.9 in terms of the change in radiance implied by one brightness count change. It is concluded from the results in Figure 2.9 that the changes in upwelling radiance due to relative humidity changes are large enough to be detected by the AVHRR and CZCS sensors.

2.3.4 Conclusions.

It can be seen from Sections 2.3.1, 2.3.2 and 2.3.3, that relative humidity variations within the marine boundary layer cause greater expected variations of upwelling radiance than particle composition variations or wind speed variations (for wind speed variations less than about 5 knots). This result is consistant with the results of Isaacs' (1980) analysis of maritime haze effects on DMSP imagery. This conclusion will be corroborated by analysis of experimental results in Chapter 4.

3.0 MEASUREMENTS AND PROCEDURES

During the period 20 September through 7 October, 1982, a set of aircraft flights were conducted off the coast of southern California. The flights were conducted coincident with overpasses of the NOAA-7 AVHRR and NIMBUS-7 CZCS. Satellite images were used to locate regions of brightness variation which were expected to be caused by aerosol variations. The aircraft was directed to these regions by radio. This data set demonstrates efficient use of satellite images to guide field measurements and is the largest set of near-simultaneous satellite and boundary layer aerosol measurements made to date. In order to properly understand the results and conclusions from these measurements, careful attention is given to the experimental instruments, measurement procedures, data reduction and analyses.

3.1 The Aircraft Measurement System.

The aircraft, a twin-engine Piper Navajo, was instrumented to measure state variables as well as aerosol properties as described by Noonkester (1981). A listing of the aircraft instrumentation is given in Table 3.1. The T, T_d, P, SST, ASSP, LWC and radiation flux measurements listed in the table were obtained continuously throughout the flights. The wand collections, CN and LIDAR measurements were made systematically at specific intervals during the flights.

Table 3.1 Aircraft Instrumentation

State Variables:

temperature, T - Rosemount sensor, HP Quartz sensor
dew point, T_d - EG and G cooled-mirror hydrometer
static pressure, P - Rosemount sensor
sea surface temperature, SST - PRT-5

Aerosol and Cloud Particles:

size distribution - ASSP (Axially Scattering Spectrometer Probe), 0.23 - 14.7 μm radius particles
particle composition - particle composition wand (Hobbs et al., 1976)
cloud liquid water, LWC - hot wire device (King et al., 1978)
condensation nuclei, CN - rapid expansion counter (Hobbs et al., 1976)

Radiometers and Lidar

shortwave and longwave radiative flux - Eppley pyranometers, both up- and down-pointing
1.06 μm LIDAR, down-pointing (Lentz, 1982)

Table 3.2 Accuracies of state variable measurement and errors in the calculation of relative humidity (from Noonkester, 1980)

T		$\pm$ 0.1°C
T_d		$\pm$ 0.5°C
P		$\pm$ 1mb
RH:	95%	$\pm$ 7.1 %
	90	6.8
	80	6.1
	70	5.9
	60	4.2
	45	3.1

3.1.1 State Variables.

Temperature (T) and pressure (P) were obtained directly from the Rosemount sensors on the aircraft. Relative humidity (RH), however, was calculated from measurements of T, P and dew-point temperature (T_d).

RH is defined as:

$$RH = 100 \times \frac{w}{w_s}$$

where w is the water vapor mixing ratio and w_s is the water vapor mixing ratio at saturation.

w and w_s are defined as:

$$w = \varepsilon \frac{e_s}{p-e}$$

and

$$w_s = \varepsilon \frac{e_s}{p-e_s}$$

where $\varepsilon = 0.622$, e is the vapor pressure and e_s is the saturation vapor pressure. From Bolton (1980), e_s at a temperature T (in ^oC) can be approximated by:

$$e_s(T) = 6.11 \times 10^{(7.5T/(T + 237.3))}.$$

For $T > 0^oC$ this expression yields errors of less than 0.1%. Also, $e(T) = e_s(T_d)$ so:

$$RH = 100 \times \frac{e}{e_s} \frac{p-e_s}{p-e}.$$

The accuracies of the T, T_d and P sensors are given in Table 3.2. Also shown in Table 3.2 are the total errors accumulated in the RH calculation (from Noonkester, 1980).

3.1.2 Particle Characteristics.

The size distributions of aerosol particles, n(r) (units $cm^{-3}\mu m^{-1}$), were measured by a Particle Measuring Systems (PMS) ASSP-100 as described by (Noonkester, 1981). The ASSP detects particles in the

Table 3.3 Channel Characteristics of ASSP-100

	SIZE RANGE			
	(3)	(2)	(1)	(0)
1	[0.23-0.38]	0.25-0.45	0.35-0.70	0.60-1.25
2	0.38-0.53	0.45-0.65	0.70-1.10	1.28-2.20
3	0.53-0.68	0.65-0.88	1.10-1.55	2.20-3.25
4	0.68-0.83	0.88-1.10	1.55-2.05	3.25-4.33
5	0.83-0.98	1.10-1.33	2.05-2.60	4.33-5.35
6	0.98-1.13	1.33-1.55	2.60-3.25	5.35-6.30
7	1.13-1.30	1.55-1.78	3.25-3.85	6.30-7.23
8	1.30-1.50	1.78-2.00	[3.85-4.40]	7.23-8.15
9	1.50-1.68	2.00-2.23	4.40-4.95	[8.15-9.10]
10	1.68-1.85	2.23-2.45	4.95-5.50	9.10-10.03
11	1.85-2.05	2.45-2.70	5.50-6.00	10.03-10.95
12	2.05-2.25	2.70-2.98	6.00-6.50	10.95-11.93
13	2.25-2.48	[2.98-3.28]	6.50-7.00	11.93-12.80
14	2.48-2.70	3.28-3.60	7.00-7.50	12.80-13.75
15	[2.70-2.95]	[3.60-3.95]	[7.50-8.00]	[13.75-14.70]

[ ] used in construction of size distribution

range 0.23 μm to 14.7 μm. The probe resolves particle sizes in 15 subranges within four major size ranges. The characteristics of the subranges used in this study are described in Table 3.3. Beginning with range 3, which is identified in Table 3.3, counts from successive non-overlapping subranges are used to create a size distribution. The result is that subranges 1-15 in range 3, 13-15 in range 2, 8-15 in range 1 and 9-15 in range 0 are used to define the size distribution. The probe cycled through ranges 0-3 sampling each range for one second. Therefore a complete distribution was measured every four seconds.

The size distribution, n(r) is defined as:

$$n(r) = dN/dr$$

where N(r) represents the total number of particles of radius greater than r. The counts measured by the ASSP divided by the volume sampled is interpreted as ΔN. The size distribution n(r) is just ΔN divided by the width at each subrange, Δr.

The many advantages and problems of particle spectrometry via light-scattering techniques have been presented by Dytch and Carrera (1976). One of the major sources of error in the technique employed by the ASSP is coincidence error. Coincidence errors result when more than one particle is present in the sampling volume. An estimate of the coincidence error is given by the ratio of multiple scattering events to single scattering events:

$$\frac{P_m}{P_s} = \frac{1 - e^{-\mu}(1+\mu)}{\mu e^{-\mu}}$$

where μ is the average number of particles in the scattering volume. The scattering volume, V, of the ASSP is $3.1 \times 10^{-4} cm^3$ (given an airspeed 54 m/s). If the concentration of particles, N, is $100 cm^{-3}$ (a

typical value for marine particles), then $\mu = NV = 0.031$ and P_m/P_s = 1.5%. Therefore, for marine aerosol particles, coincidence error is not significant.

Jensen, et al. (1980) has compared various PMS particle size spectrometers in a side by side experiment under marine conditions. Factory-calibrated PMS probes measured size distributions within an order of magnitude during the experiment. Also, extinction coefficients calculated from measurements by the various probes were within a factor of 2. Although the absolute value of the extinction calculation may be accurate only to a factor of 2, Jensen, et al. (1980) showed that relative variations of extinction determined by the spectrometers were consistant. Since the ASSP used in this study was one of the probes in the comparison of Jensen, et al. (1980), the relative differences between extinction values should be accurate.

The chemical properties of particles were determined from particle collections. Particles were collected physically during the experiment on impaction slides exposed to the airstream. Collections were made during 5 minute periods while flying constant altitude patterns. The aerosol particles collected on the slides were analyzed for their elemental composition using a scanning electron microscope (SEM) equipped with an energy-dispersive-analysis of x-ray (EDAX) capability. The supermicron particles were also tested for their deliquescent behavior using an optical microscope equipped with a humidity chamber that could reproduce the humidity at which the particles were collected.

The analysis of impaction slides yielded information on composition and deliquescence behavior of the particles. Composition of the particles was used to determine their refractive index. Also, from the

composition results, the sources of particles could be inferred. The deliquescent nature of the particles was applied to confirm the relationship between particle growth and relative humidity which is developed later. Further, the deliquesing particles were solution droplets at high relative humidity and thus spherical particles. A 'dry' particle cannot be assumed spherical. Thus, knowledge of the particle shapes was obtained from the deliquesence studies.

3.2 The Satellite Systems.

Satellite data from two systems were used in this study. The NOAA-7 AVHRR (Advanced Very High Resolution Radiometer; Schwalb, 1978) and the NIMBUS-7 CZCS (Coastal Zone Color Scanner; Hovis, 1978) are polar orbiting satellite systems capable of imaging the earth in multiple wavelength bands. For this study, emphasis is put on the red-visible and near-infrared wavelength regions since upwelling radiance at these wavelengths is less contaminated by sea surface reflectance and Rayleigh scattering (Koepke and Quenzel, 1981).

The AVHRR and CZCS images were collected in real-time (as the satellite passed overhead) at the Scripps Satellite Oceanography Facility (SSOF). The images were displayed and enhanced on the SSOF image display system during the experiment and used to direct the aircraft to regions of brightness variations. Post-experiment analysis of the images was done on the CSU Department of Atmospheric Science IRIS (Interactive Research Imaging System).

3.2.1 The NOAA-7 AVHRR

The AVHRR sensor is in sun-synchronous polar orbit. It crosses the equator at about 0300 (ascending; increasing north latitude) and 1500 (descending; decreasing north latitude) Local Time. Since the orbit

does not cross at the same position each day, the afternoon passage time over southern California varied from 1430 to 1600 PDT (Pacific Daylight Time).

The sensor images a path measuring about 3000 km across. At middle latitudes this path is broad enough so that the coverage of successive orbits overlap slightly. Thus, the southern California region was within the AVHRR coverage every day; although some days the region was at the far edges of the coverage. The sensor collects data at 2048 discrete points across its path. The surface resolution of each 'picture element' or 'pixel' is 1.1 km at the subsatellite point and expands to several kilometers at the edges of the coverage.

The AVHRR measures radiance in 5 spectral bands. Figure 3.1 illustrates the spectral response of the AVHRR channels 1(red-visible) and 2(near-infrared). In this study Channel 1 and 2 of the AVHRR were used for analysis of aerosol features. The infrared channels of the AVHRR (4 and 5) were used to interogate a scene for the presence of cold, upper level cloudiness which may not be visible at shorter wavelengths.

3.2.2 The NIMBUS-7 CZCS

The CZCS is also in sun-synchronous polar orbit with equator crossings at about noon (ascending) and midnight (descending) Local Time. The near-noon passage time varied from about 1140 to 1300 PDT for southern California.

The sensor swath-width is about 1600 km and does not overlap with successive orbits at middle latitudes. Therefore, the southern California region was not within the CZCS coverage every day. Also, in September - October 1982 the NIMBUS-7 satellite was approaching the end

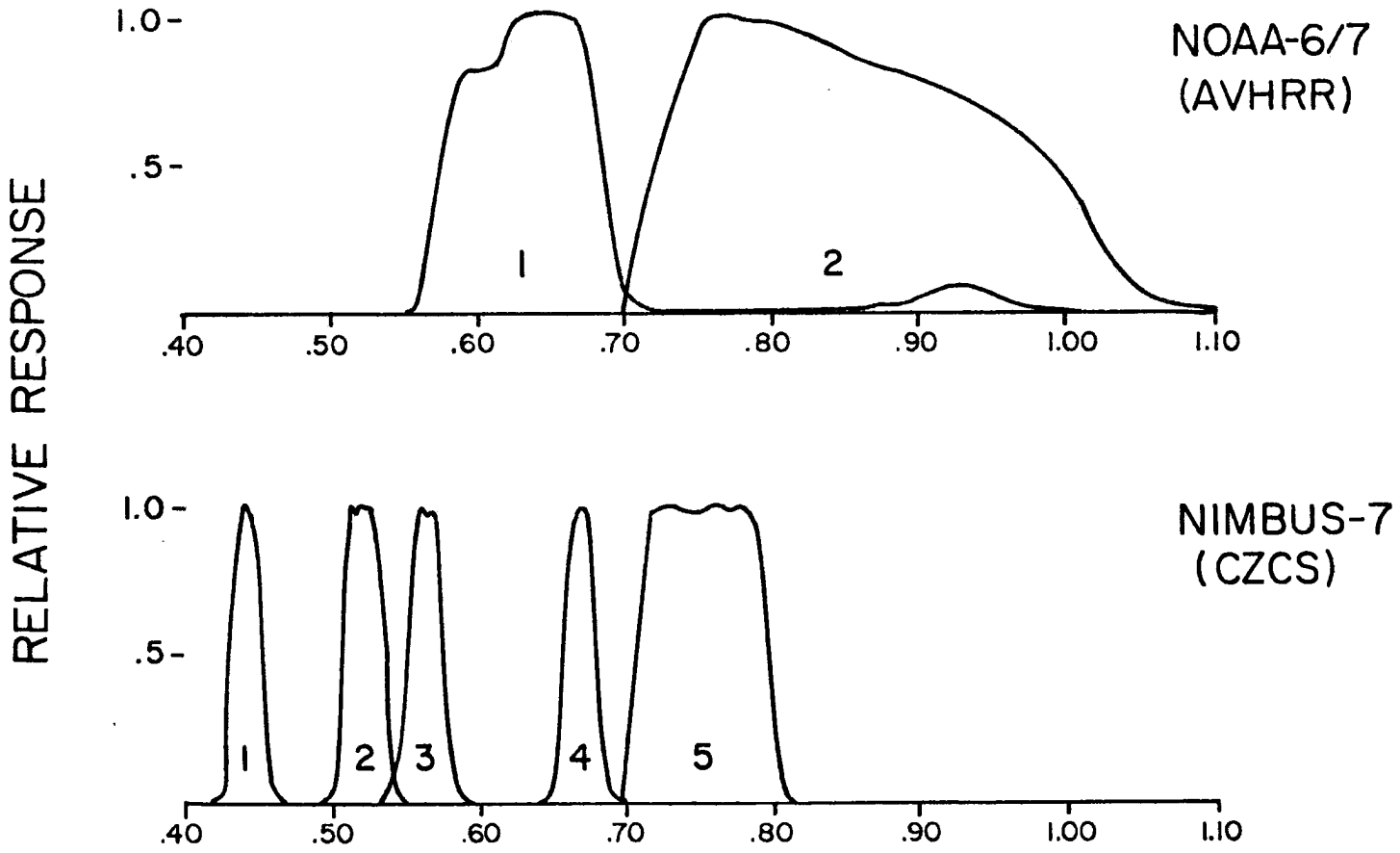

Figure 3.1 Spectral response of the AVHRR Channels 1 and 2 (red-visible and near-infrared) and CZCS Channels 4 and 5 (red-visible and near-infrared).

of four years of operation, well past its expected lifetime. The sensors were, therefore, being used sparingly to save power and the CZCS sensor was not activated every day over southern California. The result was that only eight CZCS passes were collected over the 18 days of the experiment.

The CZCS measures radiance in four visible spectral bands, one near-infrared and one infrared spectral band. Figure 3.1 illustrates the spectral response of CZCS channels 1 (blue), 2 (green), 3 (yellow), 4(red) and 5(near-infrared).

Channels 1-4 of the CZCS instrument were designed to investigate ocean color variations. Channels 1-4 are, therefore, sensitive to small radiance changes. In fact, clouds and land surfaces saturate these channels. The blue and green bands are used specificaly to sense chlorophyl concentration in the ocean's near-surface water. The red band (Channel 4) was designed to estimate the atmospheric 'contamination' by aerosol particles (Gordon, 1978). The red band provides the 'signal' of interest to this study. Channel 5 is sensitive to near-infrared wavelengths and was designed to detect clouds and ocean - land boundaries. It is, therefore, less sensitive than Channels 1-4. Although Channel 5 provides less sensitive measurements, some information is available regarding aerosol variations.

3.3 Experiment Procedures.

As a result of the 1980 experiment, described by Hindman, et al. (1984), two improvements to the experiment design were identified. First, the time delay between the satellite overpass and the aircraft measurement period should be minimized. To accomplish this objective in 1982, the aircraft was initially directed to a cloud-free region with

the aid of GOES (Geosynchronous Operational Environmental Satellite) imagery displayed on the CSU IRIS. AVHRR and CZCS images were, then, used to direct the aircraft to a region of brightness variation. With the plane in the air at the time of the satellite overpass, the time delays were kept quite small. During the experiment, time delays between satellite overpass and the initiation of a measurement period ranged from no delay to a maximum of one hour.

A second necessary improvement was to maximize the sampling density of the measurement region. The main control on this was the distance the aircraft could fly during a given period. Also, the flight patterns used provided thorough two-dimensional cross-sections as well as some high vertical resolution measurements. The aircraft normally flew at 54 m/s airspeed during the measurement periods. With an 'on-station' flight time of about four hours, the aircraft could sample up to 800 km of airspace in one flight.

Two flight pattern types were developed for the experiment described in this study. First, stacked constant altitude legs were flown to provide two-dimensional cross-sections of a region. Second, vertical spirals were flown to sample with high resolution in the vertical. The 14 flights conducted between 20 September and 7 October produced 74 constant altitude legs and 35 vertical spirals; 25 of the vertical spirals were within one hour of a satellite overpass.

The aircraft was directed to regions of brightness variation observed on CZCS and AVHRR images by voice communications from Scripps using a hand held, short-wave radio. Once a gradient in brightness was identified in the satellite image, two points about 35 kilometers apart, one in the dark region and one in the light region, were radioed to the

aircraft. The aircraft then flew a vertical spiral at each of the points and a series of constant altitude legs between the points. The constant altitude legs were positioned in the vertical according to the depth of the boundary layer as determined by temperature and dew-point temperature measurements made during the vertical spirals. Generally, at least two constant altitude legs were flown within the boundary layer and up to three legs above the boundary layer up to about 1550 m altitude.

3.4 Data Analysis.

In Chapter 2.0, the important radiative parameters of the cloud-free, marine environment were identified: $\beta_{ext}, \omega_o, p(\Theta), \tau$. Values for these parameters were derived from the aircraft measurements of aerosol characteristics. Also, the satellite data were corrected for contributions other than scattering due to aerosols. Then, the best estimate of satellite-detected radiance and upwelling radiance predicted from the scattering characteristics of particles were compared.

3.4.1 Extinction Calculation.

As described in Section 2.1, the extinction coefficient is defined as:

$$\beta_{ext} = \int_0^\infty \pi r^2 \, Q_{ext}(m,r) \, n(r) \, dr \qquad (3.1)$$

The size distribution, n(r) was determined from the ASSP measurements aboard the aircraft. The extinction efficiency, Q_{ext} was calculated from Mie theory and is a function of the complex index of refraction ($m = k - i\psi$), wavelength (λ), and particle radius.

In this study, calculations of Q_{ext} were made using a program written by Wiscombe (1979, 1980). The index of refraction used is from Shettle and Fenn (1979) for marine aerosol paticles. The index of refraction depends on relative humidity in Shettle and Fenn (1979). Therefore, the aircraft measurements of relative humidity provide more flexibility in determining the index of refraction. Further, the particle composition analysis described in Section 3.1.2 was used to corroborate the model assumptions of composition.

The optical depth was obtained from the vertical integration of β_{ext} (see Equation 2.3). The single scattering albedo and phase function were calculated by the program by Wiscombe (1979, 1980).

3.4.2 Satellite Data.

The CZCS and AVHRR sensors return image information in digital form. A digital number (which is proportional to the amount of radiation received at the satellite) is assigned to each image element. This inserts some uncertainty since only integers are used in the digitizing process. On the CZCS instrument, eight binary bits are available for digitization of the signal. This allows numbers from 0-255. On the AVHRR instrument, 10 bits are available, thus allowing numbers from 0-1023.

The conversion of digital counts to physical units for the CZCS and AVHRR is presented in detail in Appendix B. Figure 3.2 shows the counts to radiance curves for the equations discussed in Appendix B. It is clear from Figure 3.2 that CZCS Channel 4 is much more sensitive than Channel 5 or AVHRR Channels 1 and 2.

Once the digital satellite data has been converted to physical units, various contributions to the upwelling radiance must be removed

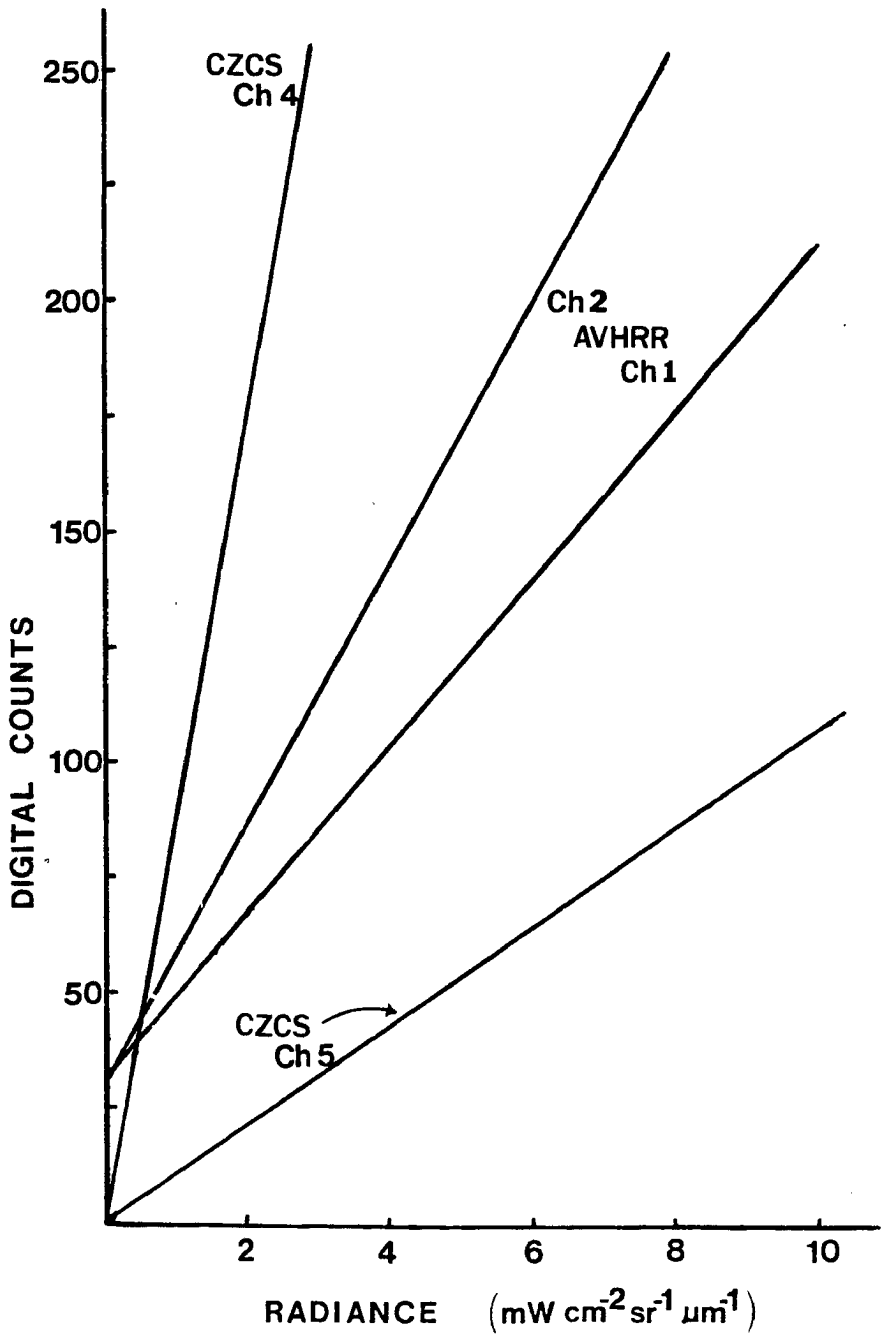

Figure 3.2 Counts vs. radiance curves for the AVHRR and CZCS sensors.

to determine the contribution from scattering by aerosols. After Gordon and Clark (1980), the radiance at satellite altitude (L_S) can be approximated as a sum of independent terms:

$$L_S = (L_W + L_G)T + L_R + L_A \qquad (3.2)$$

where L_W is the 'water-leaving' radiance caused by sub-surface reflectance, L_G is the 'glitter' radiance caused by specular reflection at the ocean surface, and T is the atmospheric transmittance. L_R is the path-added radiance due to Rayleigh scattering in the atmosphere and L_A is the path-added radiance due to aerosol scattering. L_A is the term of interest here so the magnitude and variation of the remaining terms are needed to estimate L_A from measurements of L_S.

L_W is a strongly varying function of wavelength. Figure 3.3 shows ocean albedo vs. wavelength from Ramsey (1968). At blue wavelengths the albedo of the ocean is about 5 to 10%. At red wavelengths the albedo is less than 0.5% and is zero for $\lambda = 0.7$ μm and greater. Since in this study red to near-infrared wavelengths will be usd, L_W will generally be a small contribution to upwelling radiance.

L_G is mirror-like reflection off the sea surface often called 'sun-glint'. L_G can be estimated from knowledge of sun-earth-satellite geometry and surface roughness. McClintock, et al (1971) describe a procedure for estimating the contribution of L_G to the upwelling radiance. The technique, after Cox and Munk (1956), characterizes surface roughness as a distribution of wave facets which depend on wind speed. L_G is negligible under all but certain geometries. This technique was used to test a scene's contamination by sun-glint.

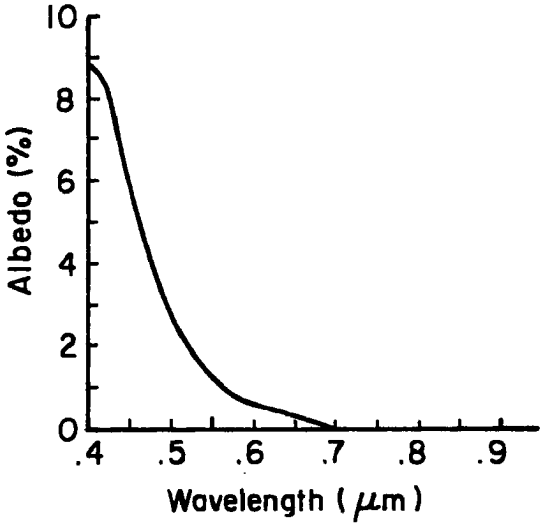

Figure 3.3 Ocean albedo vs. wavelength from Ramsey (1968).

L_R varies with wavelength but is spatially quite constant. That is, the contribution to L_S by L_R will not cause variations in L_S except over large regions where geometry changes appreciably.

To estimate L_R , the radiative transfer equation was solved (Equation 2.1). The Rayleigh optical depth, τ_R, and the scene geometry were known. Then the two-stream model described by Kaufman (1979) and Isaacs (1980) were used with τ_R and scene geometry values to estimate L_R.

Rayleigh optical depth, τ_R, depends on the concentration of gasious constituents of the atmosphere. The Rayleigh optical depth is defined as:

$$\tau_R = \int_o^H \beta_m(z,\lambda)dz$$

where H is the satellite height and $\beta_m(z,\lambda)$ is the molecular extinction coefficient. The vertical variation of β_m is due to temperature and pressure variations. The molecular extinction coefficient is then (from McCarthy, 1976):

$$\beta_m(z,\lambda) = \frac{T_o}{P_o} \frac{P(z)}{T(z)} \beta_m^o(\lambda)$$

where $\beta_m^o(\lambda)$ is the molecular extinction coefficient at T_o = 288.15 K and P_o = 1013 mb. The Rayleigh optical depth is then

$$\tau_R = \overline{\beta_m^o} \frac{T_o}{P_o} \int_o^H \frac{P(z)}{T(z)} dz$$

where $\overline{\beta_m^o}$ is the weighted average of $\beta_m(\lambda)$ over the spectral response of the satellite sensor. An estimate of τ_R can then be made from a vertical profile of pressure and temperature. Vertical soundings from the Pacific Missile Test Center, Pt. Mugu, California and Montgomery Field, San Diego were used to estimate the vertical profiles.

For each satellite image used in this study, Equation (3.2) was applied to determine L_A values. These L_A values were then used to compare with the airborne measurements as discussed in the next section.

4.0 RESULTS AND DISCUSSION

An analysis of the aircraft and satellite measurements made between 20 September to 6 October, 1982 is presented in this Chapter. First, a case from the 5th of October, 1982 is presented. Second, the composite results from the vertical aircraft spirals over the entire experiment period are discussed. A positive correlation between marine aerosol particles and satellite-detected radiance is shown. Also, the relationship between boundary layer relative humidity and extinction is examined. Third, the 6 October 1982 measurements are used to illustrate an example where a varying boundary layer depth caused uncertainty in the relationship between satellite-detected radiance and boundary layer extinction and relative humidity. Finally, the effect of significant numbers of particles above the boundary layer is examined.

4.1 5 October, 1982 Case

4.1.1 Satellite Data.

Figure 4.1 shows the AVHRR images collected at 1432 PDT (Pacific Daylight Time) on 5 October, 1982. The images have been corrected for radiance added by Rayleigh scattering, as described in Section 3.4.2. Further, the expected contribution to backscattered radiance by sunglint (specular surface reflection) was calculated as described in Section 3.4.2. It was found that the images were not significantly affected by sunglint. Also, infrared images from AVHRR and time-series images from the GOES satellite were examined for indications of high cirrus and other cloudiness. No areas of cloudiness of any type were observed.

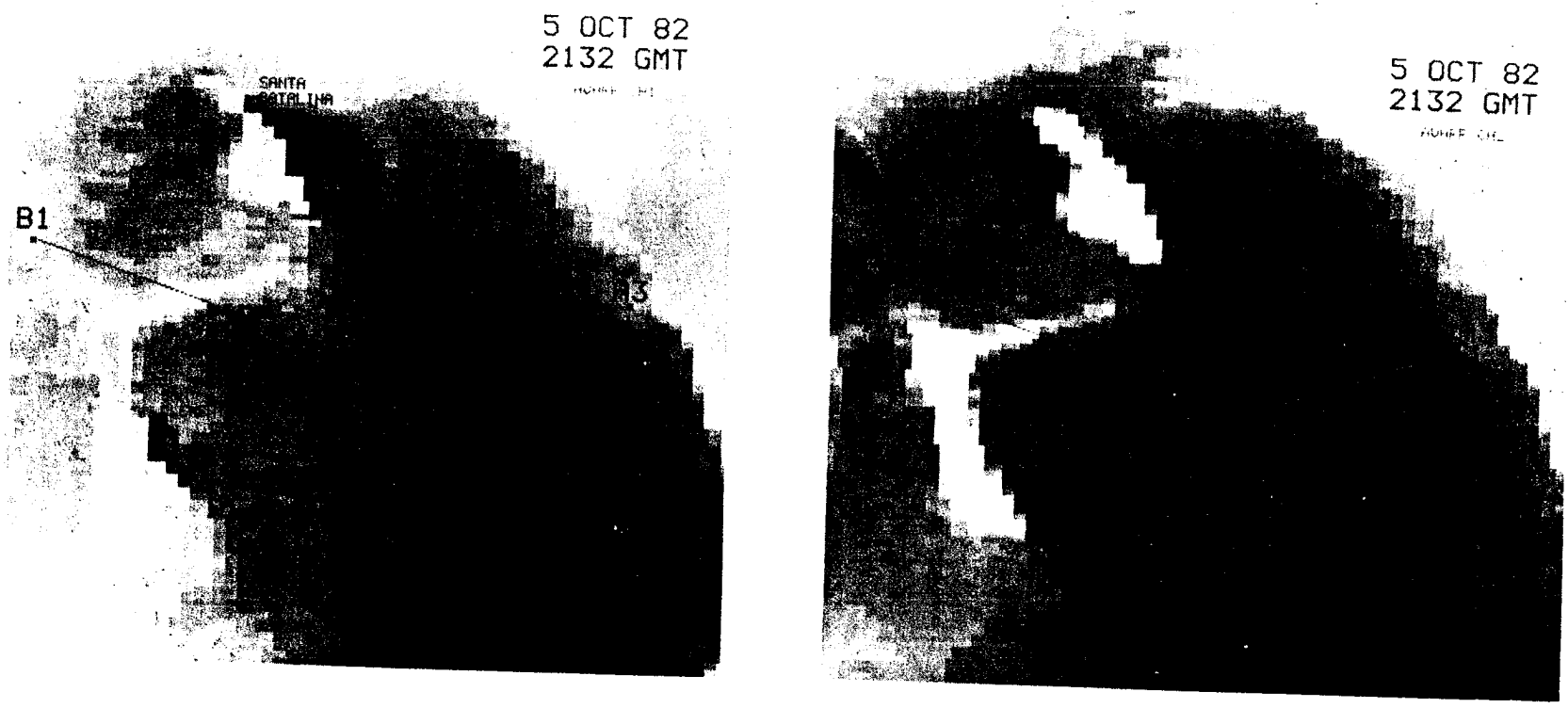

Figure 4.1 NOAA-7 AVHRR satellite images collected at 1432 PDT (Pacific Daylight Time) on 5 October 1982.

Finally, contribution to the images by non-specular reflection from the surface was left uncorrected. At red-visible and near-infrared wavelengths (corresponding to the AVHRR channels) this component of the upwelling radiance can be assumed to be negligible (Gordon and Clark, 1980). The assumption is not always adequate in coastal regions where sediment concentrations may be high. However, we employ the assumption here since the non-specular reflection component could only be characterized to the extent possible through visual observation. However, none of the regions discussed here were observed from the aircraft to be contaminated by sediments. Therefore, the images in Figure 4.1 represent a best estimate of the brightness variations due to backscatter of solar irradiance due to aerosol particles.

The flight patterns executed on 5 October 1982 are indicated on the images in Figure 4.1. Vertical spirals were flown at points A1, B1, A3, and B3. Constant altitude legs were flown at 61 m, 274 m, 488 m, 610 m, and 1524 m between both A1-B1 and A3-B3. The observers on the aircraft reported that the A1-B1 region was contaminated by small cloud elements while the A3-B3 region was cloud-free. Figure 4.2 is a two-dimensional view of the A3-B3 flight tracks.

4.1.2 Meteorology.

On 5 October 1982 the southern California coastal region was dominated by sub-tropical high pressure, which is characteristic of the summer and fall seasons. The result was a subsidence-induced, low-level inversion in the temperature profile. This stable layer traps ocean-generated particles and is often topped with stratocumulus clouds. Figure 4.3 shows the vertical profiles of potential temperature, θ, and relative humidity, RH, at points A3 and B3 on 5 October 1982. Note the

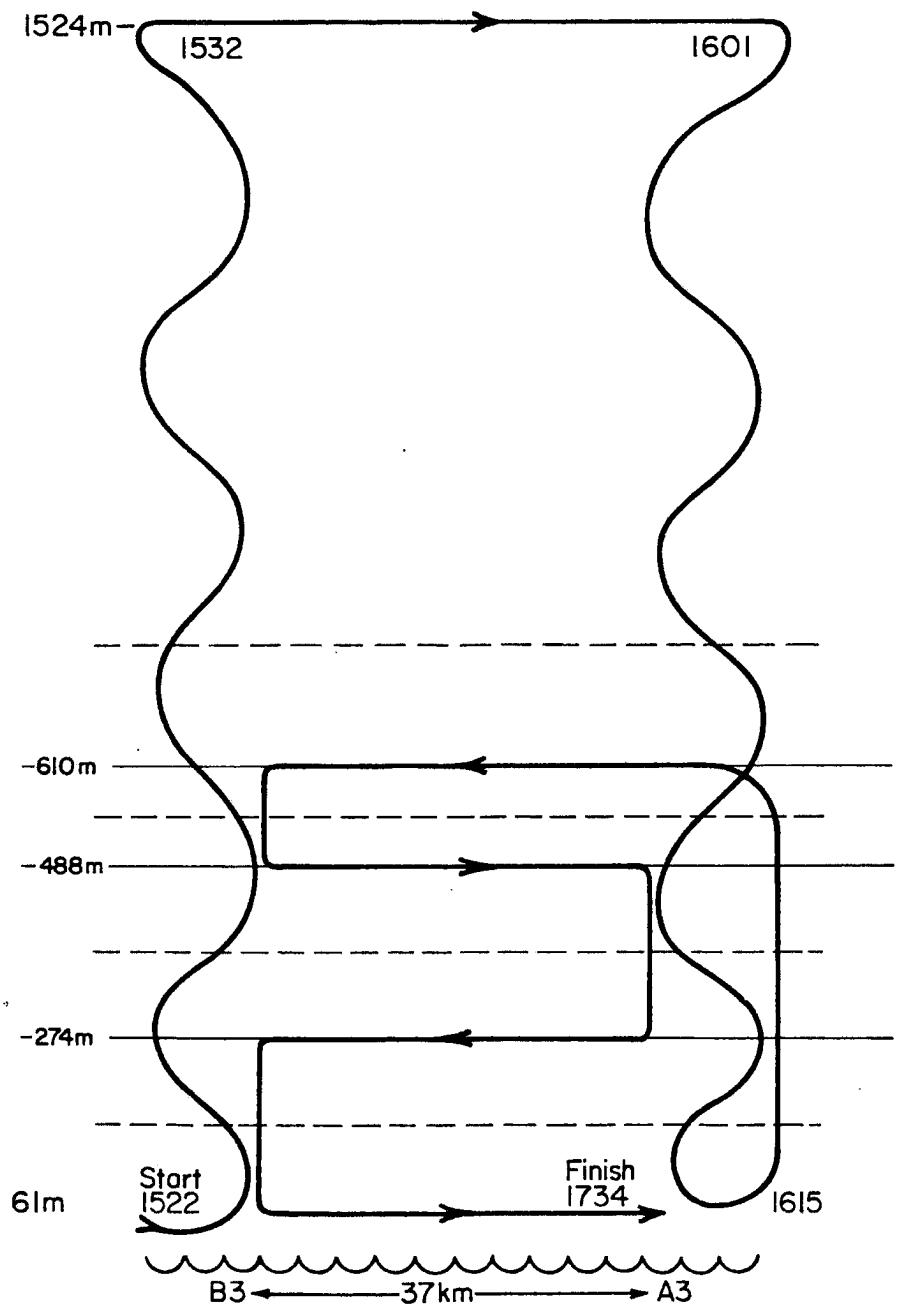

Figure 4.2 A two-dimensional view of the flight track executed between points A3 and B3 on 5 October 1982. The solid lines are the constant altitude flight levels and the dashed lines indicate the layers used for integration of the extinction values in Figure 4.4. Times at the various points along the track are given in Pacific Daylight Time.

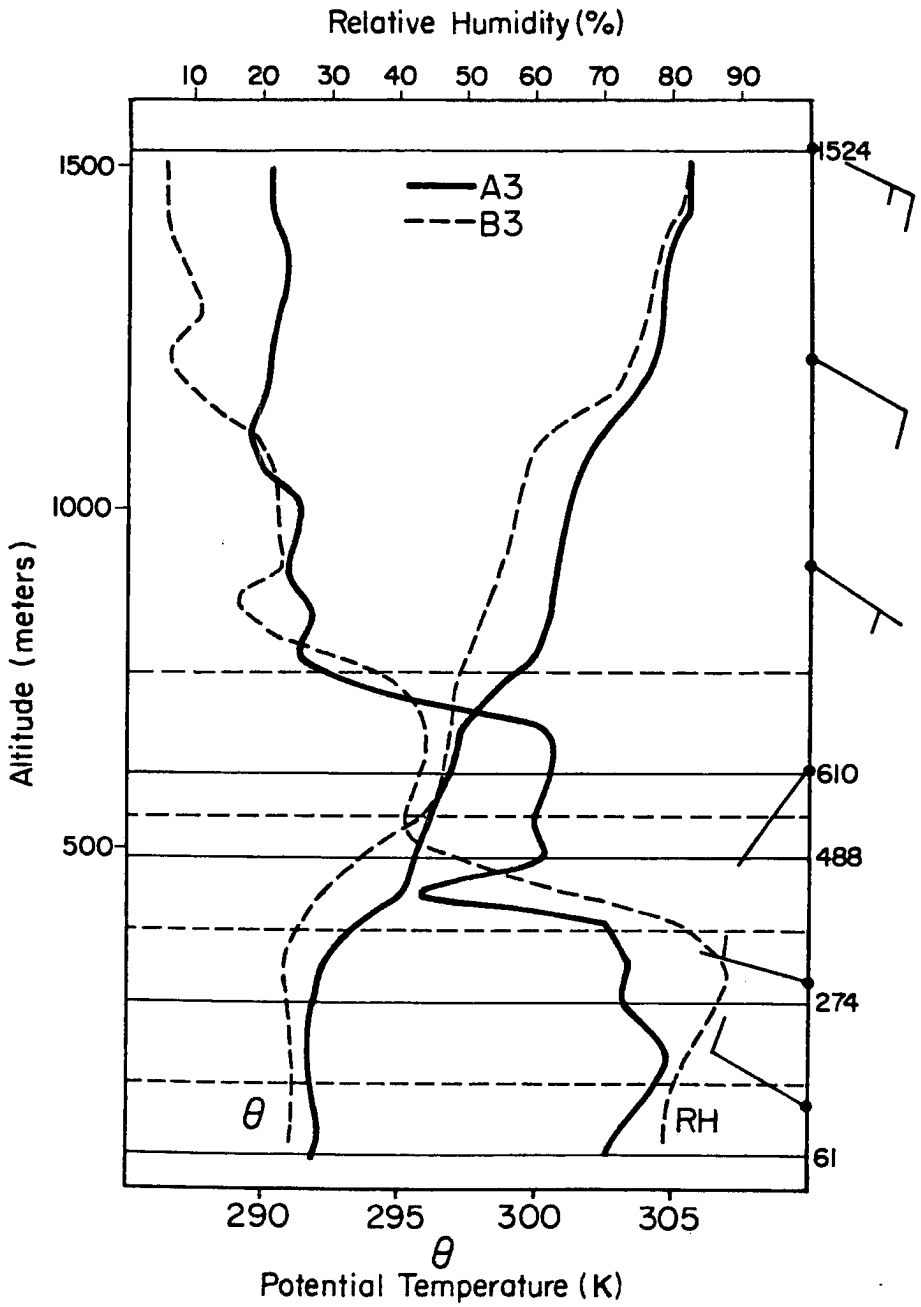

Figure 4.3 Vertical profiles of potential temperature and relative humidity at points A3 and B3 on 5 October 1982. Plotted on the right side are the winds from the San Diego sounding at 1700 PDT. The solid lines are the constant altitude flight levels and the dashed lines indicate the layers used for integration of the extinction values in Figure 4.4.

constant θ and high RH layer from the surface to about 425 m; this is the marine boundary layer. Also plotted in Figure 4.3 are the winds from the nearby San Diego sounding at 1700 PDT. Low-level winds were from the northwest in the boundary layer, while an easterly component to the flow appeared above the boundary layer.

4.1.3 Particle Measurements and Radiance Values.

The size distribution measurements were used to calculate extinction due to scattering following Equation (3.1). The weighted-average of the spectral response of Channel 1 (0.63 μm) was the wavelength used for the extinction calculations.

Figure 4.4 illustrates the results of the extinction calculations and the satellite measured radiance values. Figure 4.4a illustrates radiance values from the AVHRR Channel 1 image (Figure 4.1) which correspond to the flight track between points A3 and B3. Figure 4.4b illustrates the calculated values of extinction along the flight tracks between points A3-B3.

Figure 4.4c shows the results of integrating the extinction values in Figure 4.4b. To perform the integration, each flight level was assumed to represent a layer of vertically-constant extinction. Below 610 m, the layers were determined by the midpoint between the flight altitudes. The top of the 610 m layer was set at the top of the layer of increased relative humidity between points A3 and B3 shown in Figure 4.3. The layers used in the integrations are designated in Figure 4.2 and Figure 4.3 by dashed lines. The extinction at each measurement point along a flight level was multiplied by the layer depth. These values were then summed in the vertical giving the optical depth. The narrow lines in Figure 4.4c are the optical depths from the surface to the top

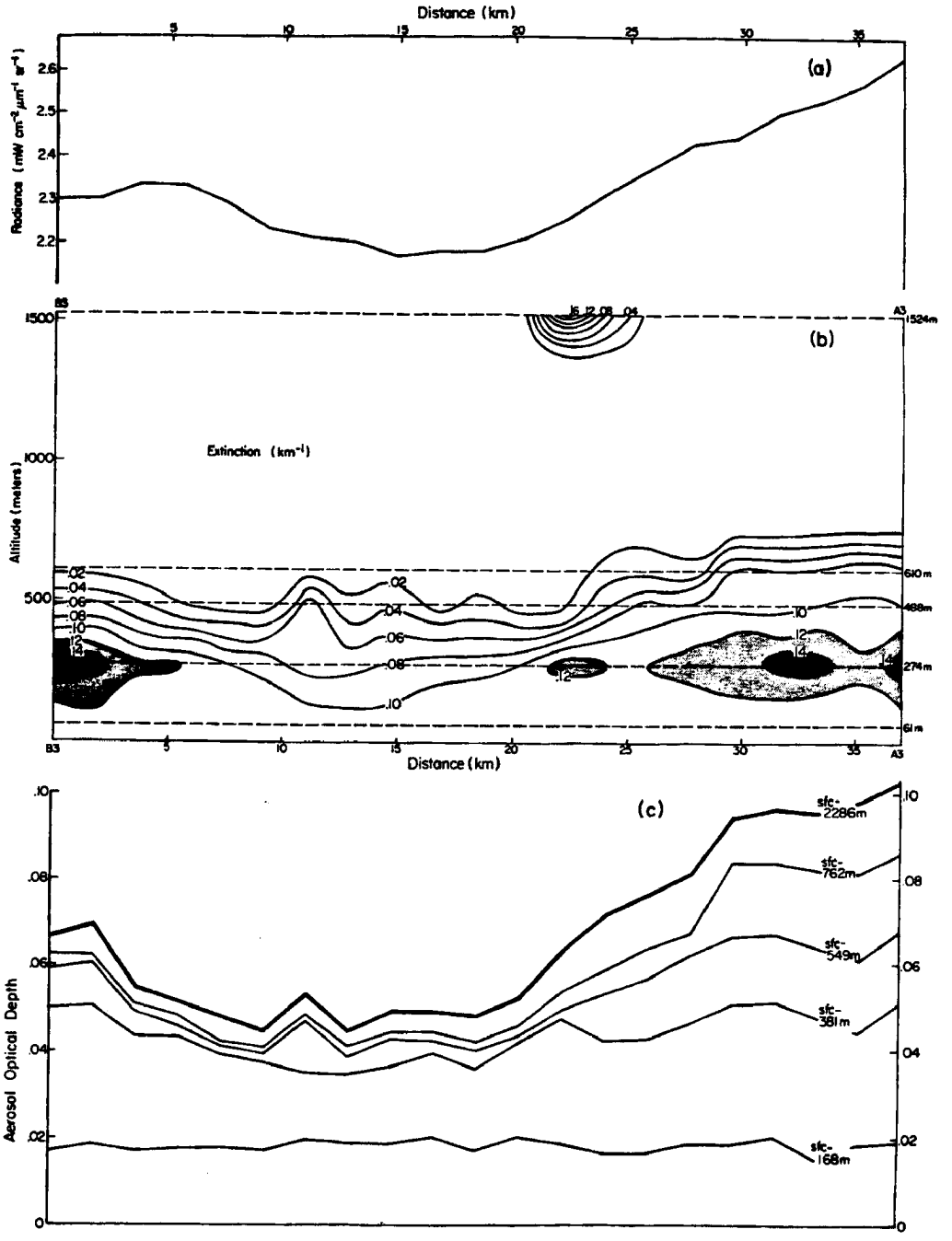

Figure 4.4 Results of the extinction calculations and the satellite measured radiance values between points A3 and B3 on 5 October 1982: (a) radiance values from AVHRR Channel 1; (b) calculated values of extinction; (c) results of integrating the extinction values in (b).

of each layer. The thick line in Figure 4.4c is the optical depth from the surface to 2296 m.

It can be seen from Figure 4.4 that the greatest contribution to the optical depth is from the extinction values at the 274 m flight level. However, much of the variation in satellite brightness between the midpoint of points A3-B3 and point A3 in Figure 4.4a appears to be due to high extinction values above the 488 m level. This higher extinction corresponds to higher relative humidity at A3 than B3 above 488 m as shown in Figure 4.3. The high values of extinction near A3 at 610 m are probably due to off-shore transport of particles by the easterly winds above the boundary layer shown in Figure 4.3

The peak of extinction at 1524 m in Figure 4.4b at about 22 km from point B3 is probably due to a localized effect. The peak could not be resolved in the satellite images and therefore is ignored for our analysis.

In Figure 4.5, the satellite-detected radiance values at 2 km intervals along the flight track A3-B3 (from Figure 4.4a) are plotted against the coincident aerosol optical depth values from the surface to 2286 m layer (from Figure 4.4c). The solid line in Figure 4.5 is the estimated linear relationship. The r-value of 0.93 indicates a high degree of correlation between radiance and optical depth values. This result confirms and expands the preliminary findings of Hindman, et al (1984). The result is also consistent with Griggs' (1975) linear relationship between LANDSAT radiances and surface sunphotometer measurements of total optical depth.

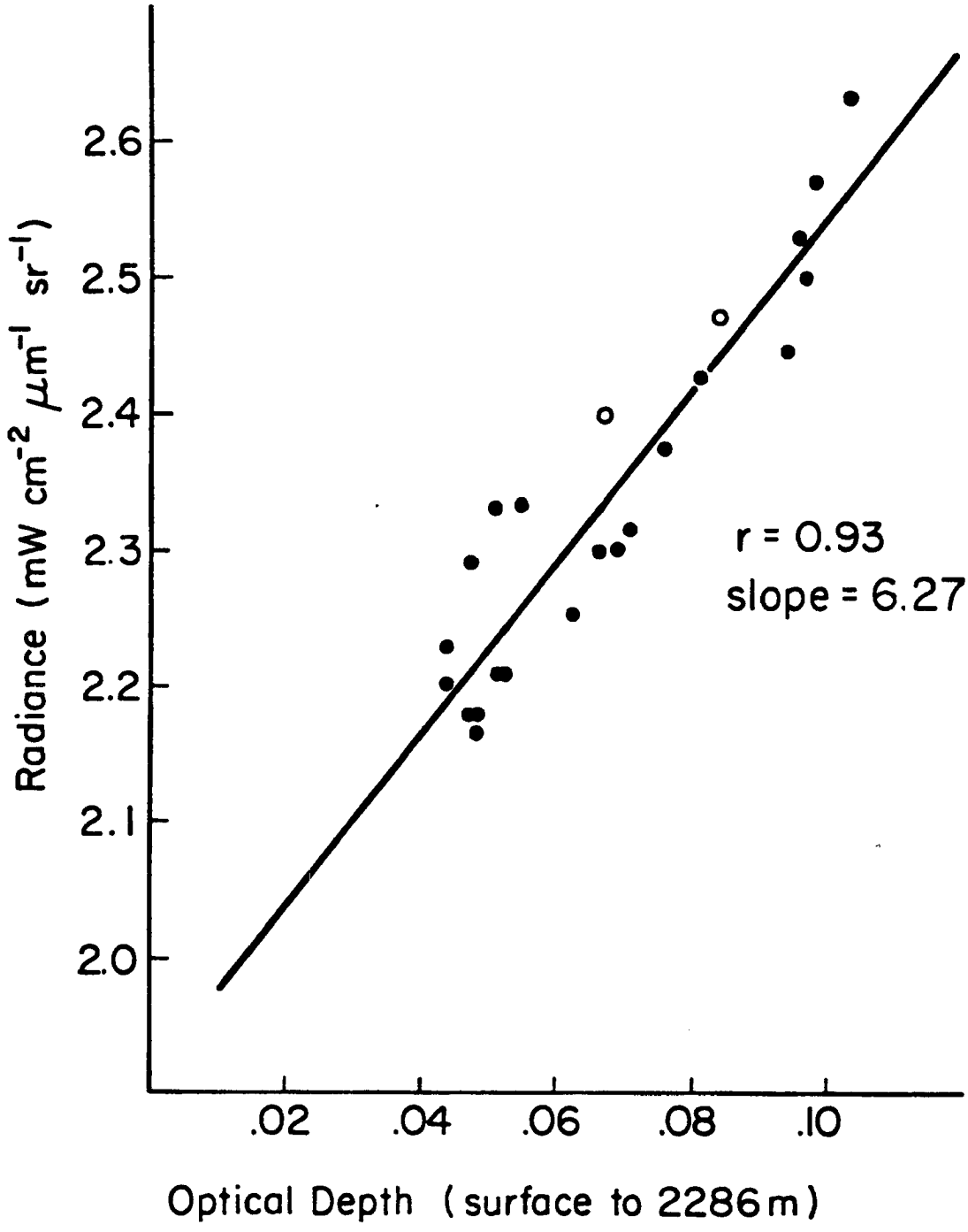

Figure 4.5 Satellite-detected radiance values at 2 km intervals along the flight track A3-B3 (from Figure 4.4a) are plotted against the coincident aerosol optical depth values from the surface to 2286 m (from Figure 4.4c). The solid line is the estimated linear relationship.

The relationship in Figure 4.5 can be tested theoretically. If the optical depth is small and single scattering dominates, the reflected radiance, L_A, for a plane-parallel, finite atmosphere with an aerosol optical depth, τ_A, is approximated by Equation (2.6). From Equation (2.6) we expect the relationship between reflected radiance and optical depth to be nearly linear as shown in Figure 4.5.

From Equation (2.6) the slope of the relationship in Figure 4.5 can be approximated by

$$\text{Slope} = \frac{F_o}{4\mu}\, p(\theta)$$

where $\omega_o = 1$. The value of F_o corresponding to the wavelength of AVHRR channel 1 is 51.4 mW cm^{-2} μm^{-1} (from Neckel and Labs, 1981). The value of μ, from the position of NOAA-7 on 5 October, 1982, is 0.520. From the slope of the regression line in Figure 4.5, $p(\theta)$ is approximately:

$$p(\theta) \sim 6.27\, \frac{4(0.520)}{51.4} \sim 0.254$$

Figure 4.6 shows $p(\theta)$ for the marine model of Shettle and Fenn (1979) at 80% relative humidity. The point corresponding to $\theta = 82^o$ (from the sun-earth-satellite geometry on 5 October, 1982) and $p(\theta) = 0.254$, from above, is indicated on Figure 4.6 (*). This point lies very close to the curve for marine aerosols. Therefore, the relationship between satellite-detected upwelling radiance and aerosol optical depth for 5 October, 1982 (Figure 4.5) is consistent with that which is expected for marine aerosol particles.

Extinction coefficients were also calculated, using Equation (3.1), from the vertical spiral measurements at points A3 and B3. The resulting extinction values are shown in Figure 4.7. The extinction values at point A3 are higher than the values at B3 through most of the vertical extent of the measurements. These measurements, when

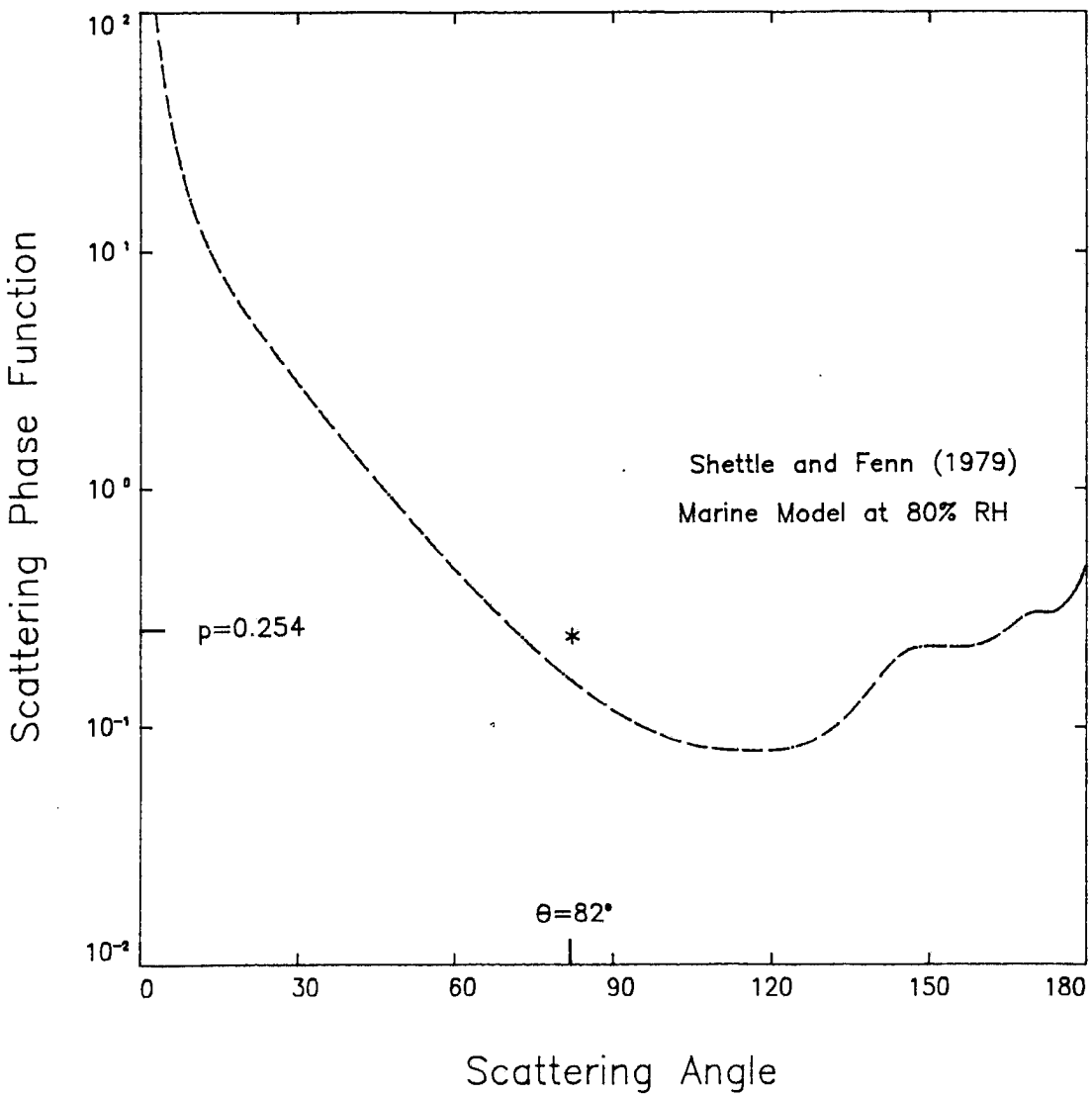

Figure 4.6 Single scattering phase function for the marine model of Shettle and Fenn (1979) at 80% relative humidity. The point corresponding to $\theta = 82^{\circ}$ (from the sun-earth-satellite geometry on 5 October 1982) and $p(\theta) = 0.254$ is indicated by *.

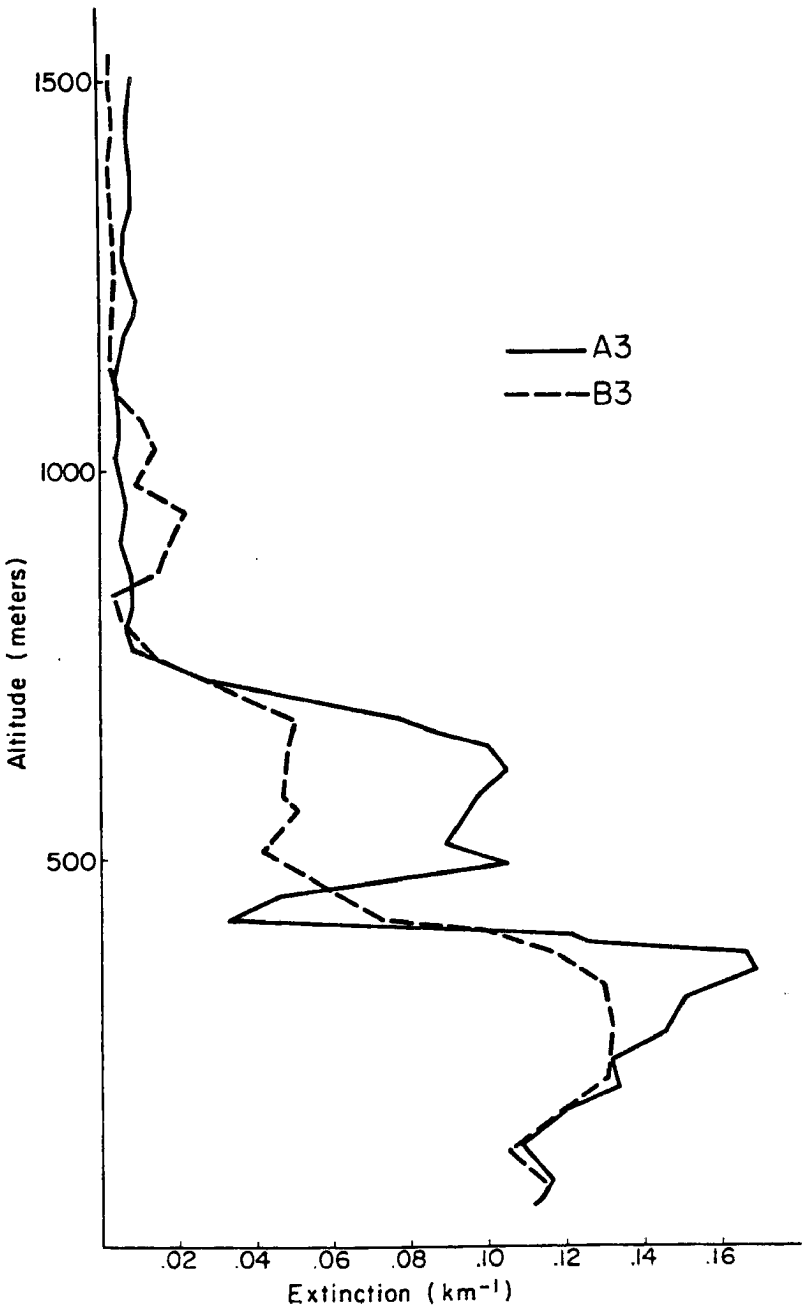

Figure 4.7 Extinction values calculated from the vertical spiral measurements at points A3 and B3 on 5 October 1982.

vertically integrated, give more accurate optical depth values than could be obtained from constant altitude measurements. These optical depth values are plotted as open circles in Figure 4.5. They appear to be slightly less in magnitude than the constant altitude values of optical depth. This may be due to errors induced by the somewhat crude integration of the constant altitude extinction values. Nevertheless, the optical depth values from the spiral data are consistent with the constant altitude data.

4.1.4 Extinction vs. Relative Humidity.

To test the hypothesis of Fett and Isaacs (1979) that the variation of satellite-detected radiance is associated with changes in relative humidity, the extinction calculations from aircraft measurements were compared to aircraft measurements of relative humidity. The extinction values were averaged over half the length of the constant altitude legs flown in the A1-B1 and A3-B3 regions shown in Figure 4.1. The extinction values are plotted in Figure 4.8 against averages of relative humidity for the same constant altitude leg. Covert *et al.* (1972) and Fitzgerald *et al.* (1982) have shown a relationship between extinction and relative humidity using ambient aerosols and theoretical calculations (see Section 2.3 and Figures 2.5 and 2.6) which is consistent with the relationship shown in Figure 4.8. The small scatter about the curve in Figure 4.8 is most likely due to changes in the aerosol populations of the various regions. This confirms the theoretical arguments in Section 2.3.

As shown in Figure 4.5, the satellite detects bright regions which are regions of high aerosol optical depth. The results in Figure 4.8 demonstrate that relative humidity variations are correlated with

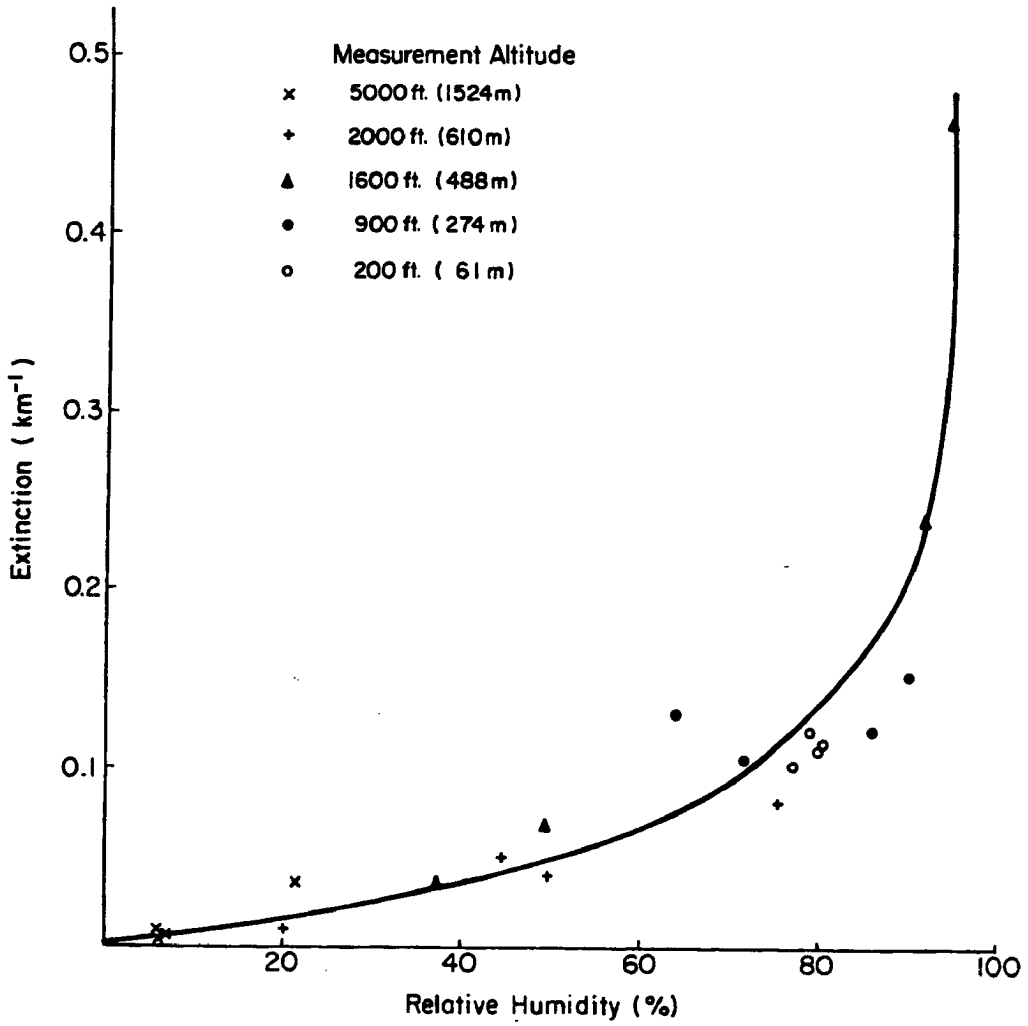

Figure 4.8 Extinction values averaged over half the length of the constant altitude legs flown in the A1-B1 and A3-B3 regions are plotted against coincident averages of relative humidity. The solid line is a hand-drawn estimate of the relationship.

extinction values. Since optical depth is the vertical integration of extinction, it appears that for 5 October, 1982, the satellite-detected bright regions are regions of higher relative humidity and vice versa. This confirms the hypothesis of Fett and Isaacs (1979) and theoretical arguments in Section 2.3.

4.1.5 Particle Characteristics.

Particle samples were collected on exposed slides during the experiment as described in Section 3.1.2. Conclusions from the composition analysis of the collected particles are as follows:

1. The particles collected within the boundary layer were primarily composed of Na and Cl. Small amounts of S, Ca and K were also found. These elements are all common in sea water and therefore the particles are of oceanic origin.
2. The particles collected above the boundary layer were of three types; oceanic particles (as described above), soil derived particles (Si) with some hygroscopic elements (S, Cl, etc.), and purely soil derived particles (Si, Fe, Ti).

From these composition results, the aerosol models of Shettle and Fenn (1979) were used to assign refractive indices and single scattering albedoes to the particles. The Shettle and Fenn marine particle model was used to characterize the boundary layer particles. For the upper level particles, a combination of the marine, rural and urban models was used. The effect of the urban model is to add 20% soot-like particles to the rural distribution. Since the presence of organic compounds could not be detected with the SEM/EDAX analysis, the amount of soot in the upper level particles remains unknown. Therefore, two mixtures of

the Shettle and Fenn models were used for the upper level particles. Mix I used 30% marine particles and 70% rural particles. Mix II used 30% marine particles and 70% urban particles. The difference between Mix I and Mix II is that 14% of Mix II particles are sootlike and thus more absorbing. Mix II is considered as an upper limit on the presence of sootlike particles, since the airborne measurements were usually taken more than 50 km from urban sources.

Figure 4.9 illustrates results of deliquescent analysis from 5 October, 1982, as described in Section 3.1.2. The left hand picture in Figure 4.9 shows the crystaline nature of the dry particles on the slides. The right hand picture shows these particles deliquesced and became spherical at 73% relative humidity (the ambient relative humidity during collection). Consequently, the particles on these slides were nearly spherical before collection.

4.2 Spiral Measurements.

Vertical spirals were flown at 35 locations during the ten flights of the experiment. In this Section, analysis of the measurements from spirals flown within one hour of a satellite overpass will be presented. Figure 4.10 shows the spiral locations off the southern California coast.

4.2.1 Satellite-Detected Radiance vs. Aerosol Characteristics.

Figures 4.11 and 4.12 show examples of the calculated values of extinction, relative humidity, and potential temperature from the vertical spiral measurements. Figure 4.11 shows values from a spiral on 22 September, 1982. Figure 4.12 shows values from a spiral on 2 October, 1982. Figures showing the remaining spiral measurements are located in Appendix D.

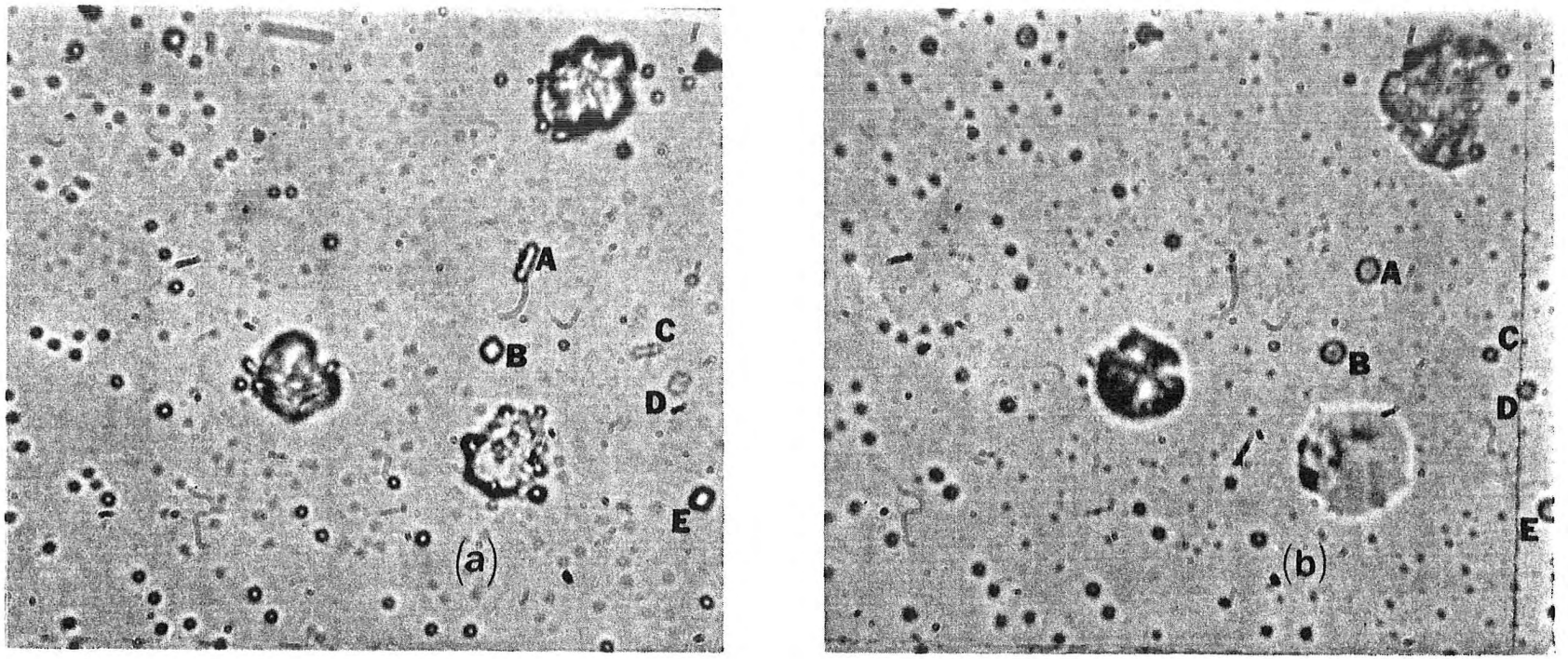

Figure 4.9 Aerosol particles collcted at 274m above the ocean between point A3 and the midpoint between A3 and B3 on 5 October, 1982. (a) Observed at ~ 20% relative humidity in the laboratory (b) after humidified to ~ 73% relative humidity.

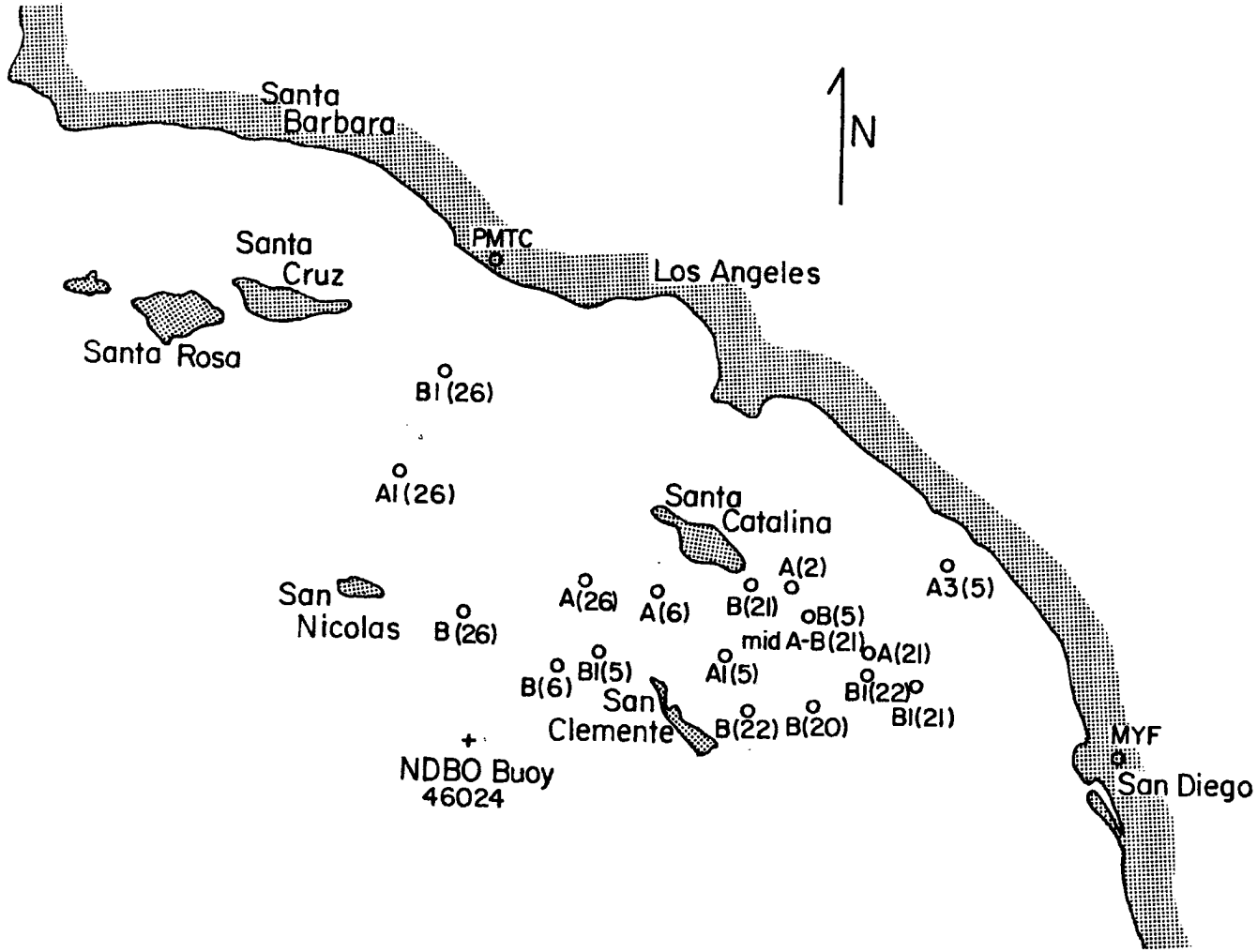

Figure 4.10 Locations of spirals flown within one hour of a satellite overpass.

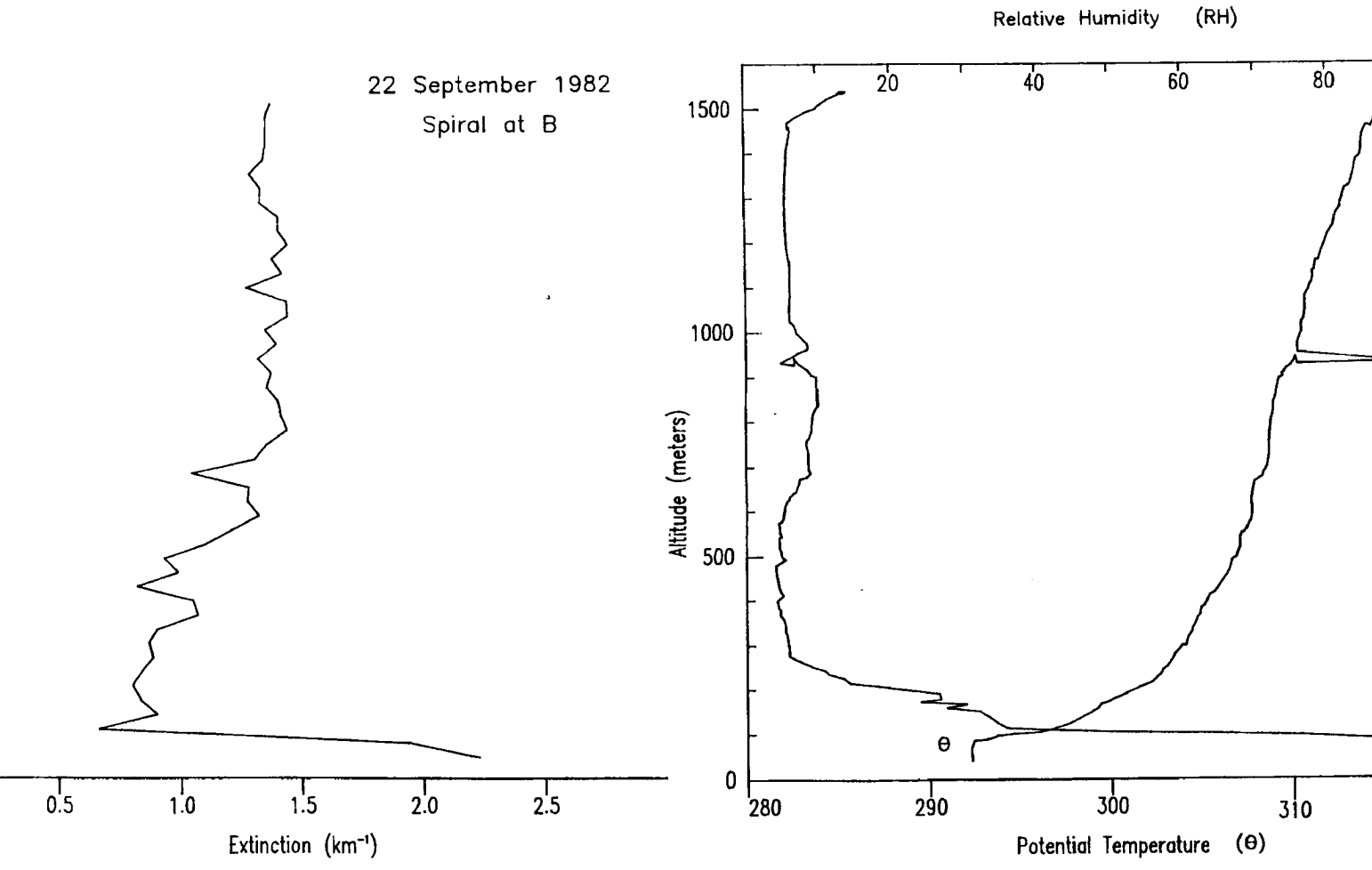

Figure 4.11 Calculated values of extinction, relative humidity and potential temperature from the vertical spiral measurements at point B on 22 September 1982.

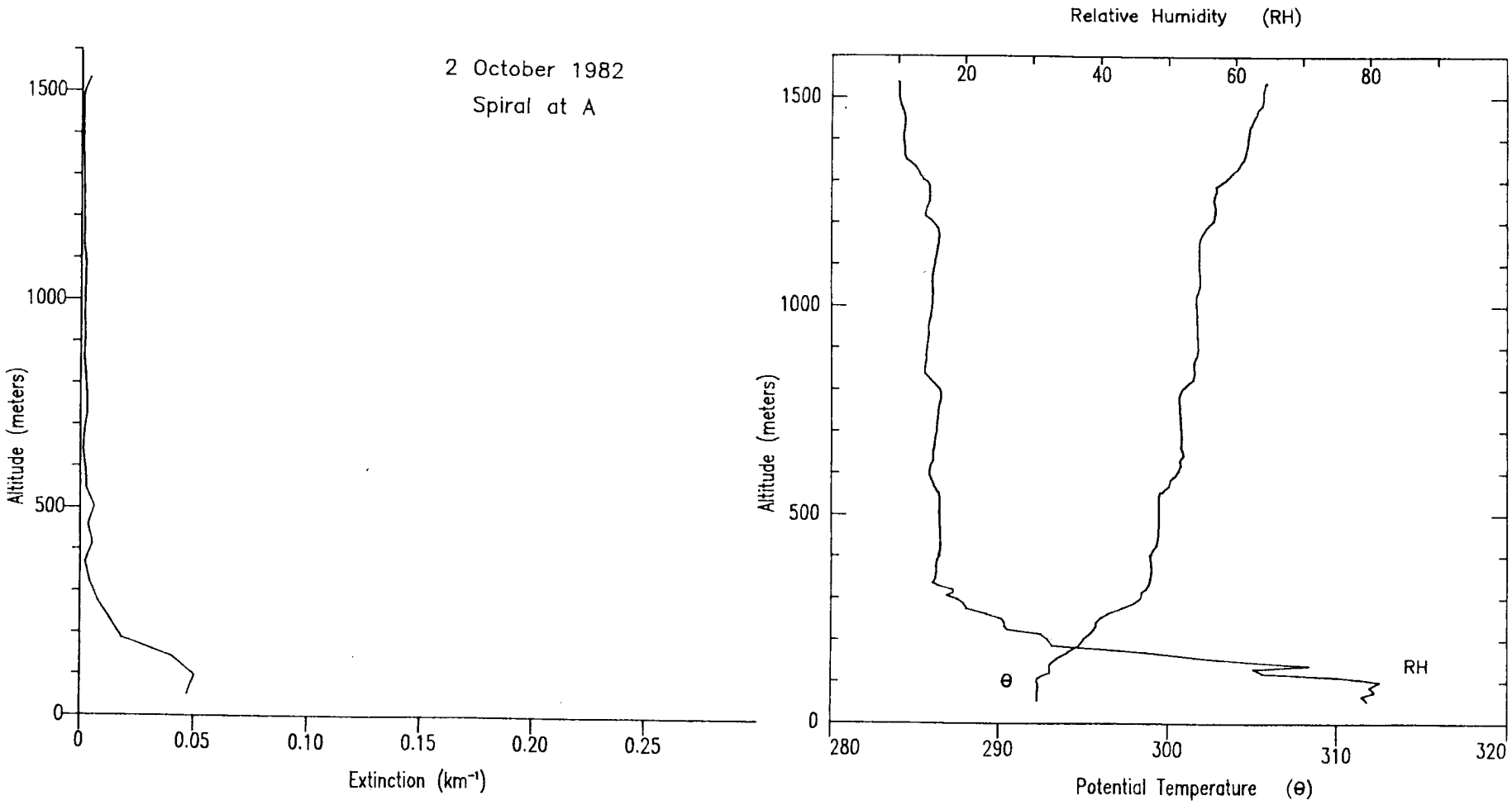

Figure 4.12 Same as Figure 4.11 but for point A on 2 October 1982.

The marine boundary layer is apparent in Figures 4.11 and 4.12 as the layer of constant θ and high RH near the ocean surface. In Figure 4.12 extinction is higher within the marine boundary layer than above it. High extinction above the boundary layer as seen in Figure 4.11 is due to particles above the boundary layer and is discussed in Section 4.4.

The extinction values were calculated at the mean wavelength of the satellite sensor's spectral response. The satellite overpass nearest the time of the spiral was chosen. Within the boundary layer, the particles' index of refraction particle was assumed to follow the Shettle and Fenn (1979) marine model. The index of refraction at each satellite wavelength is given in Table 4.1. Above the boundary layer, the particles were assumed to behave as a mixture of marine, rural and urban particles according to Shettle and Fenn (1979). As described in Section 4.1.5, two mixtures have been used. Mix I contained 30% marine particles and 70% rural particles. Mix II contained 30% marine particles and 70% urban particles. The extinction was calculated using each mix described in Section 4.1.5. The difference between particle models is assumed to be a bound on the extinction variation due to composition differences. The indices of refraction at each satellite wavelength and for each mix are given in Table 4.1.

The aerosol optical depth was obtained when the extinction values were integrated vertically following Equation (2.3). The satellite-detected radiances were compared to the aircraft-measured aerosol optical depth. However, a direct comparison would not account for

Table 4.1 Indeces of Refraction

	Satellite Channel	λ	Boundary Layer	Upper level Mix I	Mix II
AVHRR	Ch1	0.63	$1.38-i(1.6\times10^{-8})$	$1.51-i(4.5\times10^{-3})$	$1.53-i(6.1\times10^{-2})$
	Ch2	0.84	$1.37-i(4.4\times10^{-7})$	$1.50-i(7.0\times10^{-3})$	$1.53-i(6.3\times10^{-2})$
CZCS	Ch4	0.67	$1.38-i(3.3\times10^{-8})$	$1.51-i(4.3\times10^{-3})$	$1.53-i(6.1\times10^{-2})$
	Ch5	0.75	$1.37-i(1.4\times10^{-7})$	$1.51-i(5.3\times10^{-3})$	$1.53-i(6.2\times10^{-2})$

differences due to the sun-earth-satellite geometry. Assuming single scattering dominates, Equation (2.6) can be written:

$$\frac{4\mu L_A}{F_o} \sim \omega_o p(\theta)\tau_A \tag{4.2}$$

The satellite-dependent terms have been put on the left-hand side, while the aerosol-dependent terms remain on the right-hand side of Equation (4.2).

The cosine of the satellite zenith angle, μ, was calculated from the satellite and spiral positions. The solar flux density, F_o, is from Neckel and Labs (1981) and is a weighted mean over the spectral response of the satellite sensor. The satellite-detected radiance was corrected for Rayleigh scattered radiance following Equation (3.2) to give L_A. The values of L_A are averages over the area of the spiral (usually 15-30 pixels).

The single scattering albedo, ω_o, and the phase function, $p(\theta)$, were calculated using Mie theory from the size distributions averaged through each spiral. The index of refraction, m, used in the calculations was a weighted mean of boundary layer and upper level indices;

$$\bar{m} = \frac{\tau_{BL}}{\tau_{BL}+\tau_{UL}} m_{BL} + \frac{\tau_{UL}}{\tau_{BL}+\tau_{UL}} m_{UL} \tag{4.3}$$

where BL indicates a boundary layer quantity and UL indicates an upper level quantity. The total optical depth τ_A is $\tau_{BL} + \tau_{UL}$.

Figure 4.13 illustrates the results of values from the left- and right-hand sides of Equation 4.2, for the spiral measurements made within one hour of an AVHRR overpass. Figure 4.14 illustrates the same

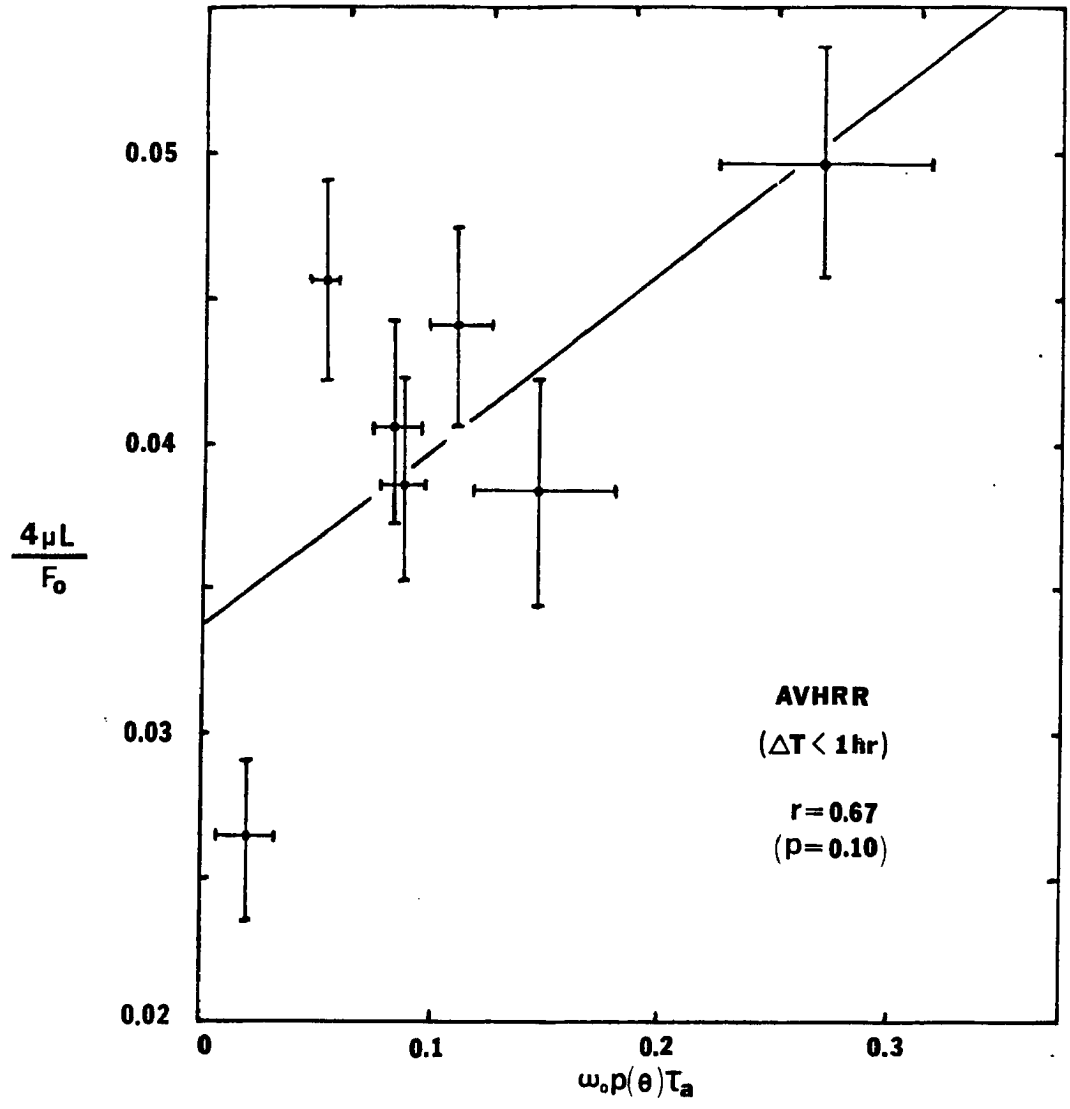

Figure 4.13 Satellite-dependent terms vs. aerosol-dependent terms from Equation (4.2) for spiral measurements made within one hour of an AVHRR overpass. The vertical error bars are due to the uncertainty in the satellite measurements of radiance. The horizontal error bars are due to the application of Mix I vs. Mix II to the upper level particles.

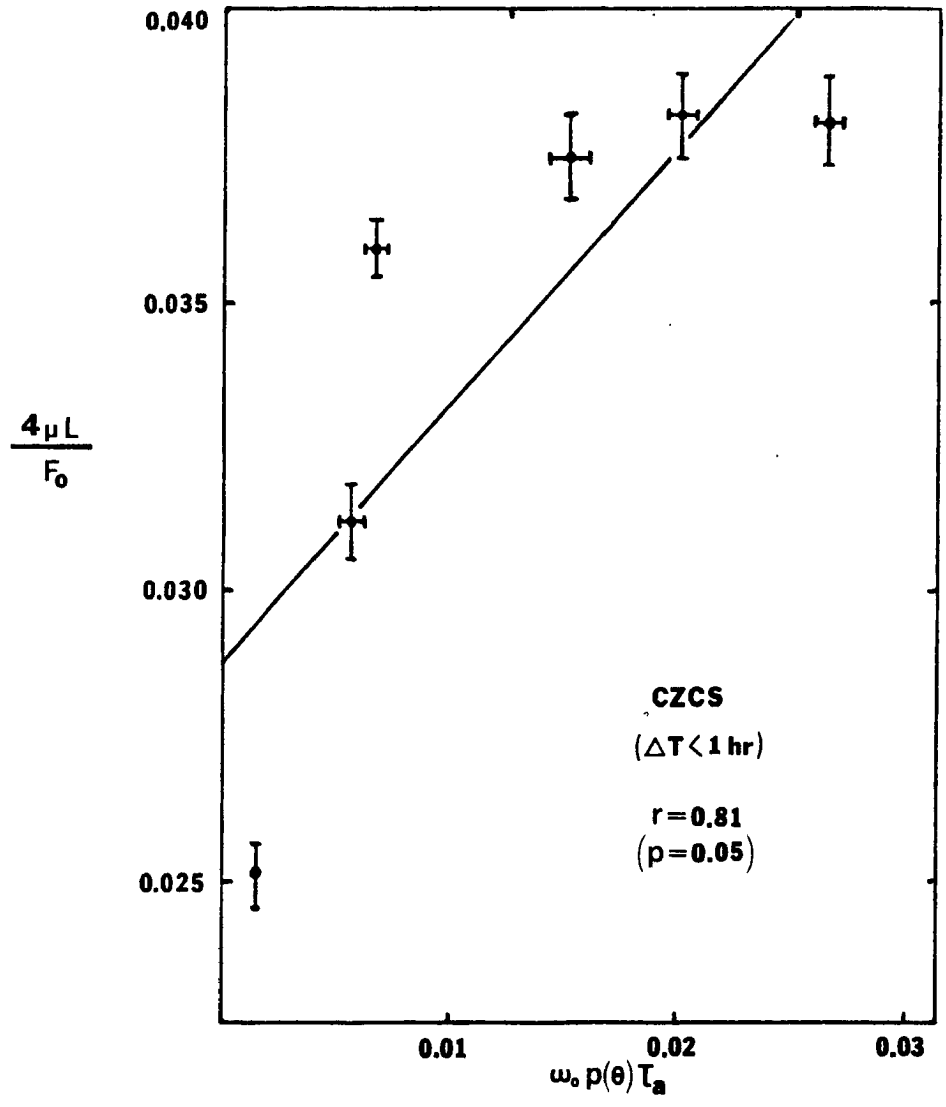

Figure 4.14 Same as Figure 4.13 but for spiral measurements made within one hour of a CZCS overpass.

plot as Figure 4.13 but for values from CZCS overpasses. The vertical error bars in Figures 4.13 and 4.14 are due to the uncertainty in the satellite measurements of radiance. The horizontal error bars are due to uncertainties in assumptions about the composition of particles above the boundary layer. The maximum of the error bar at each point is from application of Mix I (30% marine, 70% rural) to the upper level particles. The minimum of the error bar is from application of Mix II (30% marine, 70% urban; more absorbing than Mix I and therefore a lower value of ω_o).

A positive relationship between values of satellite-dependent terms and aerosol-dependent terms is apparent in Figures 4.13 and 4.14. The correlation for the CZCS cases is higher than for the AVHRR cases. One cause of this difference is the fact that the particle measurements collected near the AVHRR overpasses were significantly affected by aerosol particles above the boundary layer. Examination of figures in Appendix D shows that some of the spiral measurements did not extend high enough to include all of the upper level particles. Therefore, the values of τ_A for those spirals are not total aerosol optical depth. Upper level particles also account for the larger horizontal error bars for the AVHRR cases than for the CZCS cases in Figures 4.13 and 4.14. The affect of upper level particles will be further discussed in Section 4.4.

In the 5 October case, since sun-earth-satellite geometry was constant, a high degree of correlation was found in the direct comparison between L_A and τ_A (Figure 4.5). The same comparison between L_A and τ_A for the spiral measurements, was made and illustrated the importance of the geometry terms in Equation 4.2. Further, adding of

each term in the comparison between satellite-dependent and aerosol-dependent terms will illustrate the importance of each term.

Table 4.2 presents the correlation coefficient resulting from the comparison of various combinations of the terms in Equation 4.2. The results are separated by satellite sensor. From Table 4.2, it is clear that L_A and τ_A are not directly comparable. Inclusion of satellite view geometry (i.e., μ) in the comparison of satellite-dependent and aerosol-dependent terms, increases the correlation considerably. Adding $p(\Theta)$ to the comparison improves the correlation only slightly for the AVHRR cases and, in fact, decreases the correlation for the CZCS cases. Finally, the addition of ω_o to the comparison has no significant affect on the correlation.

The results in Table 4.2 show that satellite viewing geometry is the most important information for the comparison of satellite-dependent and aerosol-dependent terms when applied to measurements from different days and locations. Also, the weak contribution from $p(\Theta)$ and ω_o implies that the composition and size distribution of the particles were not determined accurately enough so that the inclusion of $p(\Theta)$ and ω_o in the comparison would improve the correlation.

4.2.2 Extinction vs. Relative Humidity.

As discussed in Section 2.3.4, if variations of total particle numbers due to wind speed variations are small, boundary layer extinction, aerosol optical depth and thus, upwelling radiance, should depend on boundary layer relative humidity. Figure 4.15 presents values of extinction plotted against relative humidity; the values are averages through the marine boundary layer of the measurements from the vertical spirals. The results in Figures 4.15 and 4.8 are in remarkable

Table 4.2 Correlation coefficient resulting from various comparisons of satellite and aerosol dependent terms in Equation 4.2.

	AVHRR SPIRALS	CZCS SPIRALS
L_A vs τ_A	0.11	0.47
$\frac{4\mu L_A}{\tilde{F}_o}$ vs τ_A	0.56	0.95
$\frac{4\mu L_A}{\tilde{F}_o}$ vs $p(\theta)\tau_A$	0.67	0.82
$\frac{4\mu L_A}{\tilde{F}_o}$ vs $\omega_o p(\theta)\tau_A$	0.67	0.81

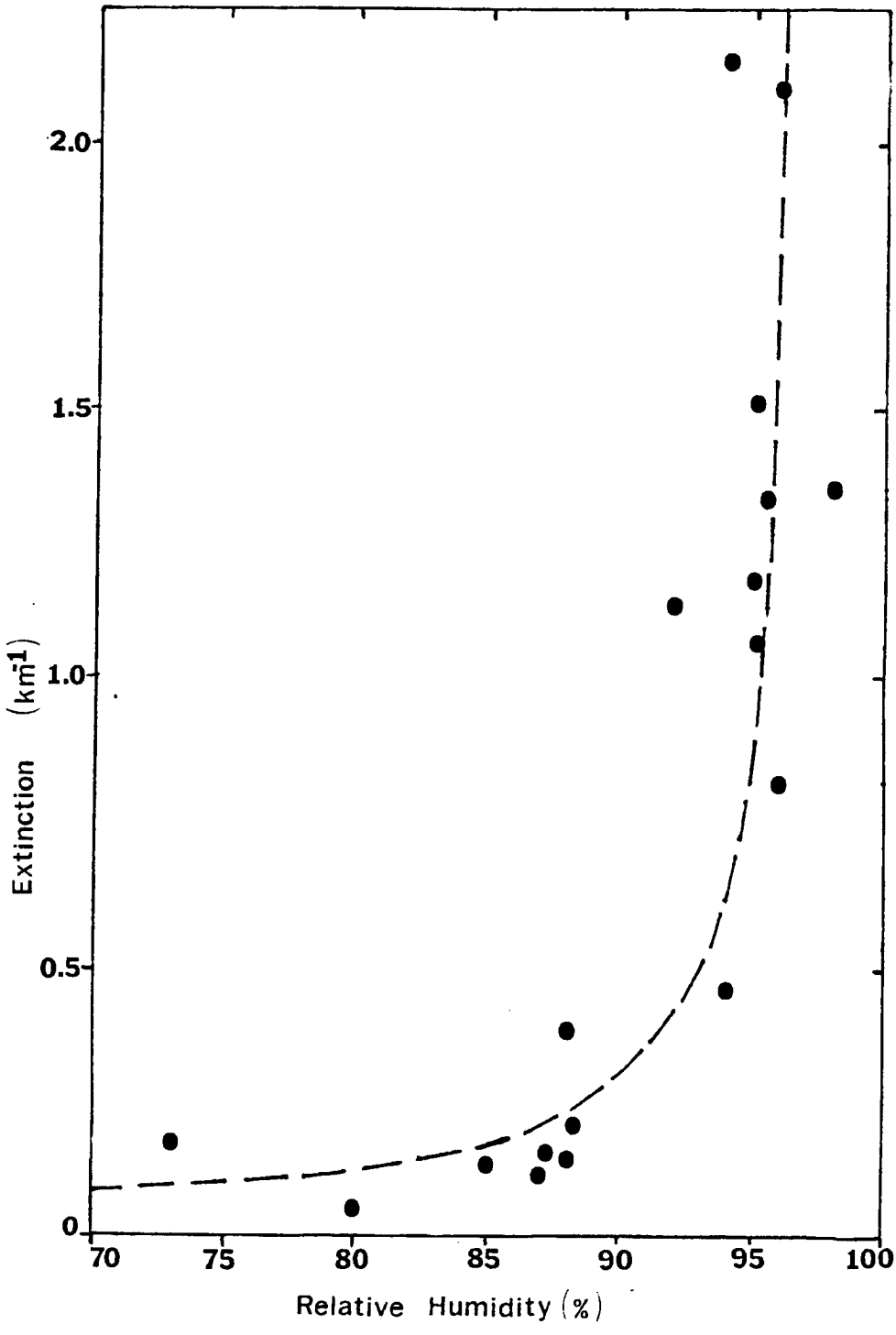

Figure 4.15 Values of extinction plotted against relative humidity; the values are averages through the marine boundary layer of the measurements from the vertical spirals.

agreement. Consequently, the relationship between relative humidity and extinction holds over several days within the marine boundary layer.

The scatter about the curve in Figure 4.15 most likely results from variations of total particle number caused by wind speed variations. Since the scatter in Figure 4.15 is small and a relationship is apparent, wind speed variations during the experiment must have been small. In Section 2.3.2, the effect of wind speed variation on the total number of aerosol particles was shown to be small, relative to satellite sensitivities, if velocity variation is below about 5 knots. During the experiment, surface wind speed was measured by buoy number 46024 operated by the Data Buoy Office of NOAA. The location of buoy 46024 is shown in Figure 4.10. The measurements showed that prevailing wind speed varied by less than 2 knots during the CZCS spiral cases and less than 4 knots during the AVHRR spiral cases. Larger values of wind speed variation would have lead to greater scatter of the points in Figure 4.15.

Since boundary layer extinction relates positively to relative humidity, as shown in Figure 4.15, upwelling radiance should also show some relation to boundary layer relative humidity. Figure 4.16 illustrates the results of comparing the left-hand side of Equation (4.2) with boundary layer relative humidity. A positive relationship is seen in Figure 4.16 with a correlation coefficient of 0.73. The value of $p < .01$ indicates that this relationship in Figure 4.16 is significant at the 1% level.

As dicussed in Section 4.2.1, the AVHRR spiral cases were significantly affected by upper level particles. Upper level particles limit the extent to which total optical depth is dependent on boundary

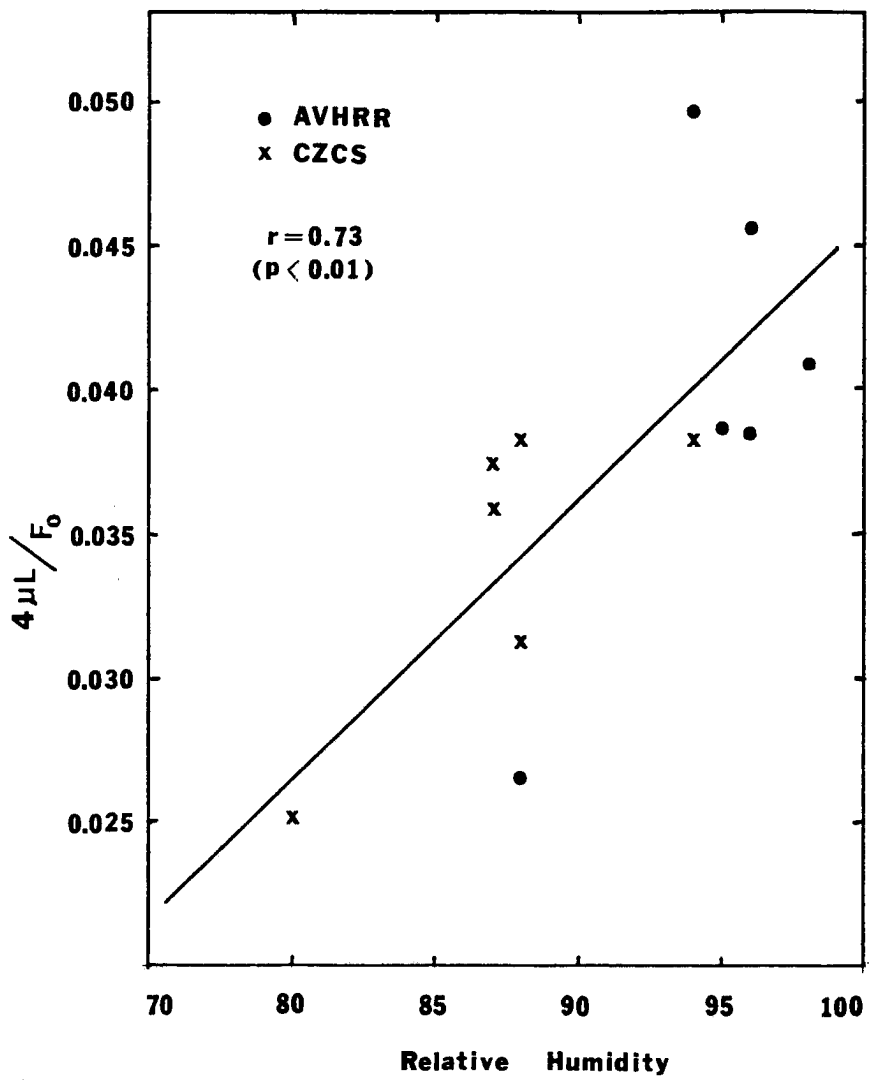

Figure 4.16 The satellite-dependent terms of Equation (4.2) vs. boundary layer relative humidity.

layer extinction and thus boundary layer relative humidity. For this reason, the AVHRR cases in Figure 4.16 exhibit more scatter than the CZCS cases.

4.3 6 October, 1982 Case.

Figure 4.17 shows the CZCS images collected at 1258 PDT on 6 October, 1982. Vertical spirals were flown at points A and B on Figure 4.17. Constant altitude legs were flown (between points A and B) at 30m, 76m, 122m, 183m, 244m, 640m and 1509m. The location of points A and B were determined from examination of GOES images to be in a region free of clouds. The patterns were flown as coincident with the overpass of NIMBUS-7 as possible so no guidance from the CZCS images was used to pinpoint the strongest gradient. The spiral at point B began 14 minutes prior to the overpass of NIMBUS-7 and the spiral at point A began 14 minutes after the overpass.

The extinction values calculated from the aircraft measurements during the vertical spirals at points A and B are shown in Figure 4.18. Figure 4.17 indicates that the satellite-detected radiance is slightly higher at point A than at point B. This implies that the aerosol optical depth is greater at point A than at point B. Integration of the calculated extinction values from the spiral measurements in Figure 4.18 gives $\tau_A = 0.068$ at point A and $\tau_A = 0.058$ at point B. It does not follow, however, that the boundary layer extinction at point A is larger than at point B. Inspection of Figure 4.18 shows that the boundary layer extinction at point B is, in fact, larger than at point A. The difference in the optical depth is made up by a deeper boundary layer at point A (280 m) than at point B (130 m).

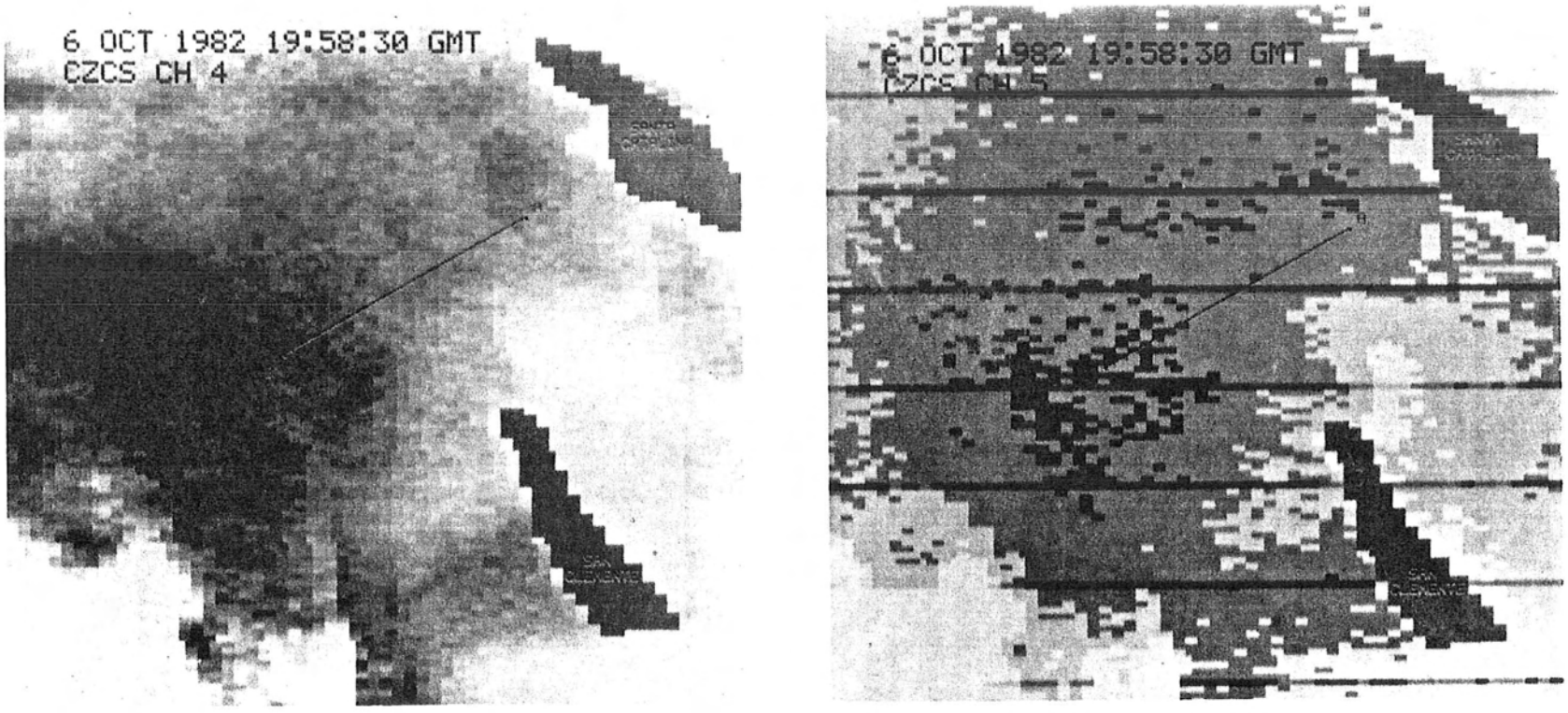

Figure 4.17 NIMBUS-7 CZCS satellite images collected at 1258 PDT on 6 October 1982.

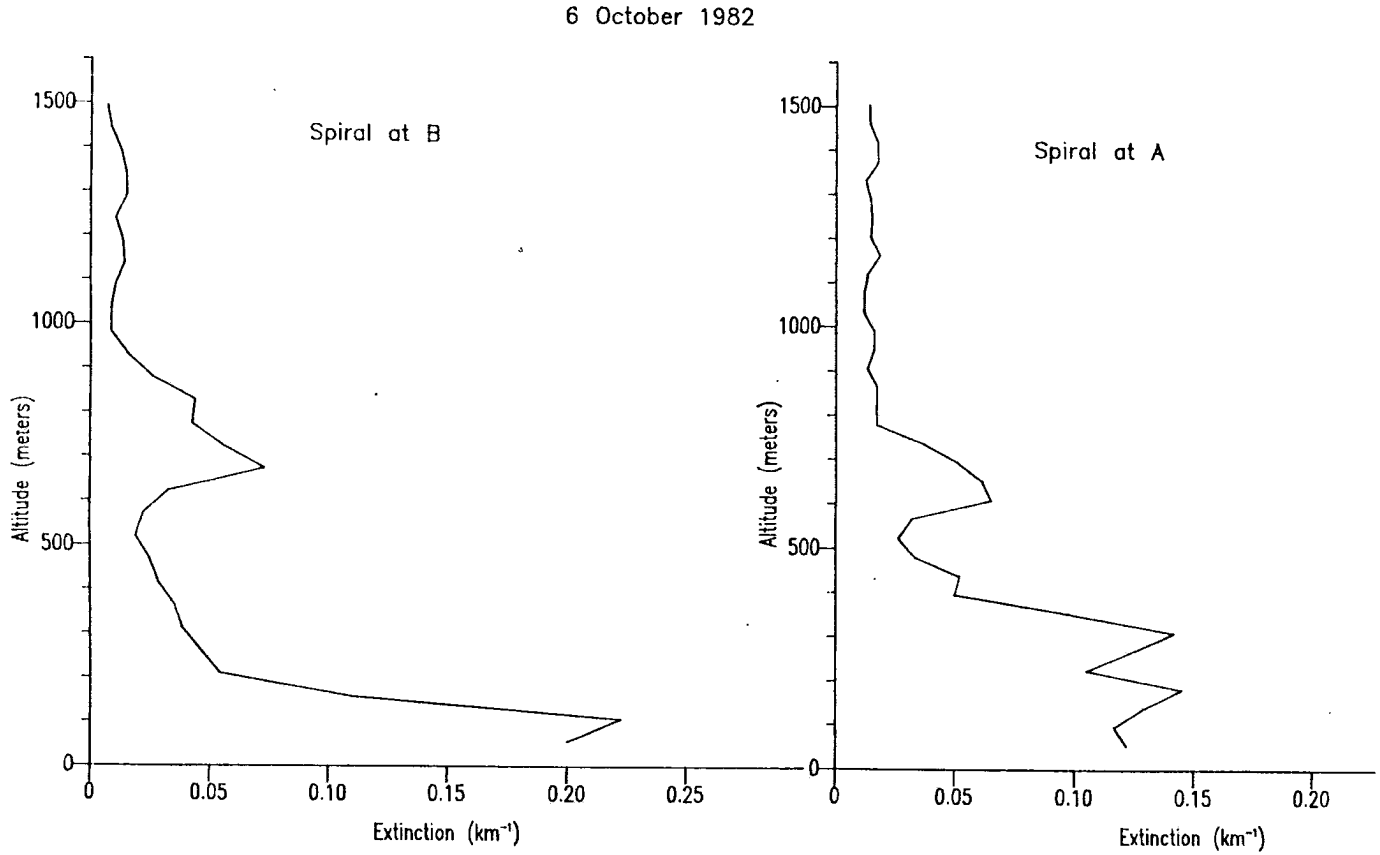

Figure 4.18 Vertical distribution of extinction at points A and B on 6 October 1982.

Figure 4.19 is a combination of the satellite and aircraft measurements on 6 October 1982. Figure 4.19a shows the radiance values from the CZCS Channel 4 and 5 images which correspond to the flight track between points A and B. Figure 4.19b shows the calculated values of extinction along the flight track between points A and B.

As in Figure 4.18, Figure 4.19 shows that although the satellite-detected radiance is greater at point A than at point B, the boundary layer extinction is greater at point B than at point A. Also, the deepening of the boundary layer going from point B to point A is apparent.

The 6 October case illustrates an example of the ambiguity in the relationship between satellite-detected radiance and bounary layer relative humidity which results from boundary layer depth variation. Isaacs (1980) showed by theoretical considerations of DMSP-detected radiance that upwelling radiance is not uniquely a function of relative humidity but also depends on the depth of the aerosol layer. The results here confirm Isaacs' work. Because of this ambiguity, information about the boundary layer depth is needed to more accurately estimate relative humidity from satellite-detected radiance.

4.4 Upper Level Particles and Their Detection by Satellite.

4.4.1 Upper Level Particles.

A distinct change in the vertical distribution of aerosols occurred during the experiment. During the first half of the experiment, the extinction values above the marine boundary layer were 10 times higher than during the second half of the experiment. Figure 4.20 shows the average size distribution of particles above the boundary layer for spirals before and after 26 September, 1982. From Figure 4.20,

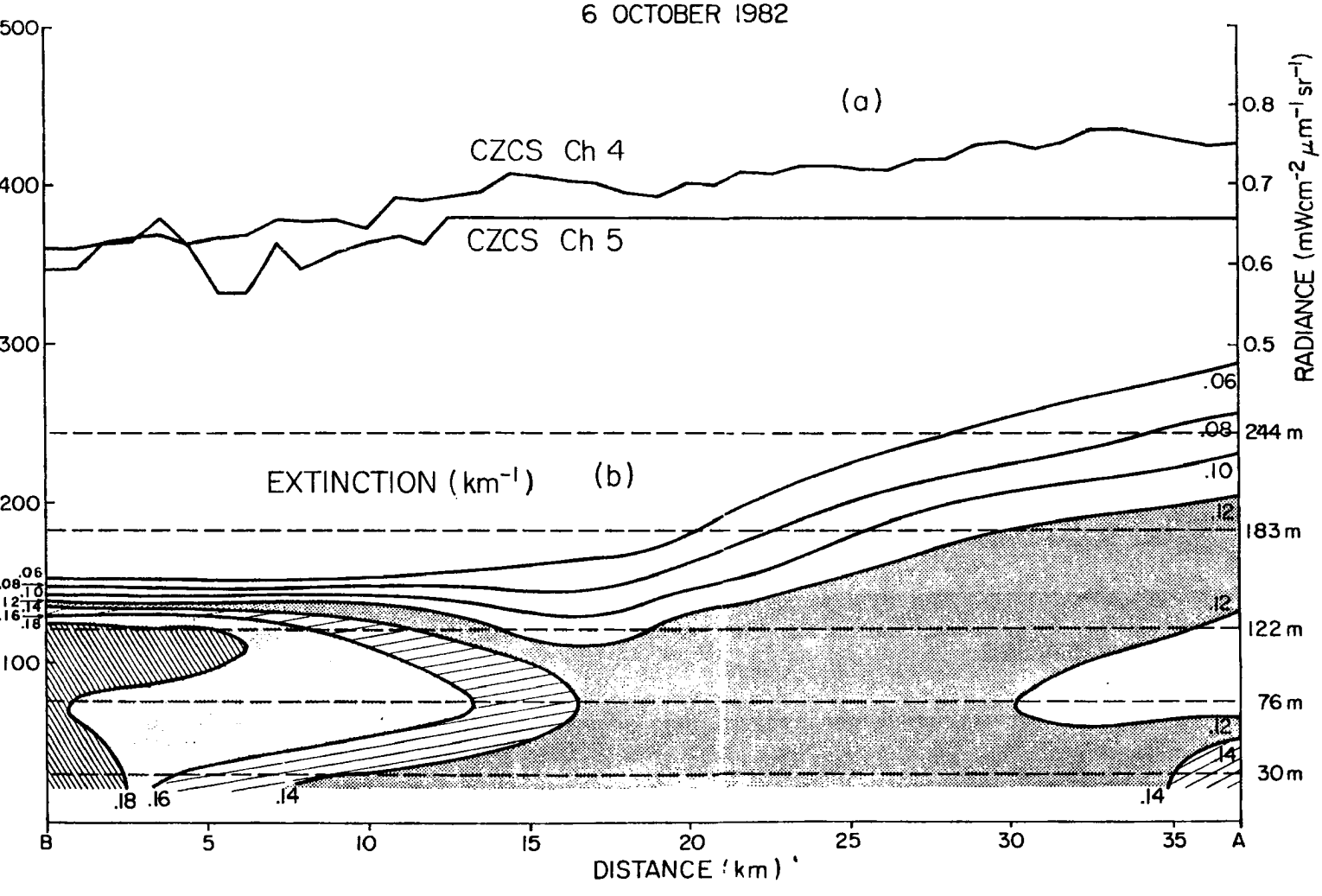

Figure 4.19 (a) Radiance values from CZCS Channels 4 and 5 between points A and B on 6 October 1982. (b) Cross-section of extinction values.

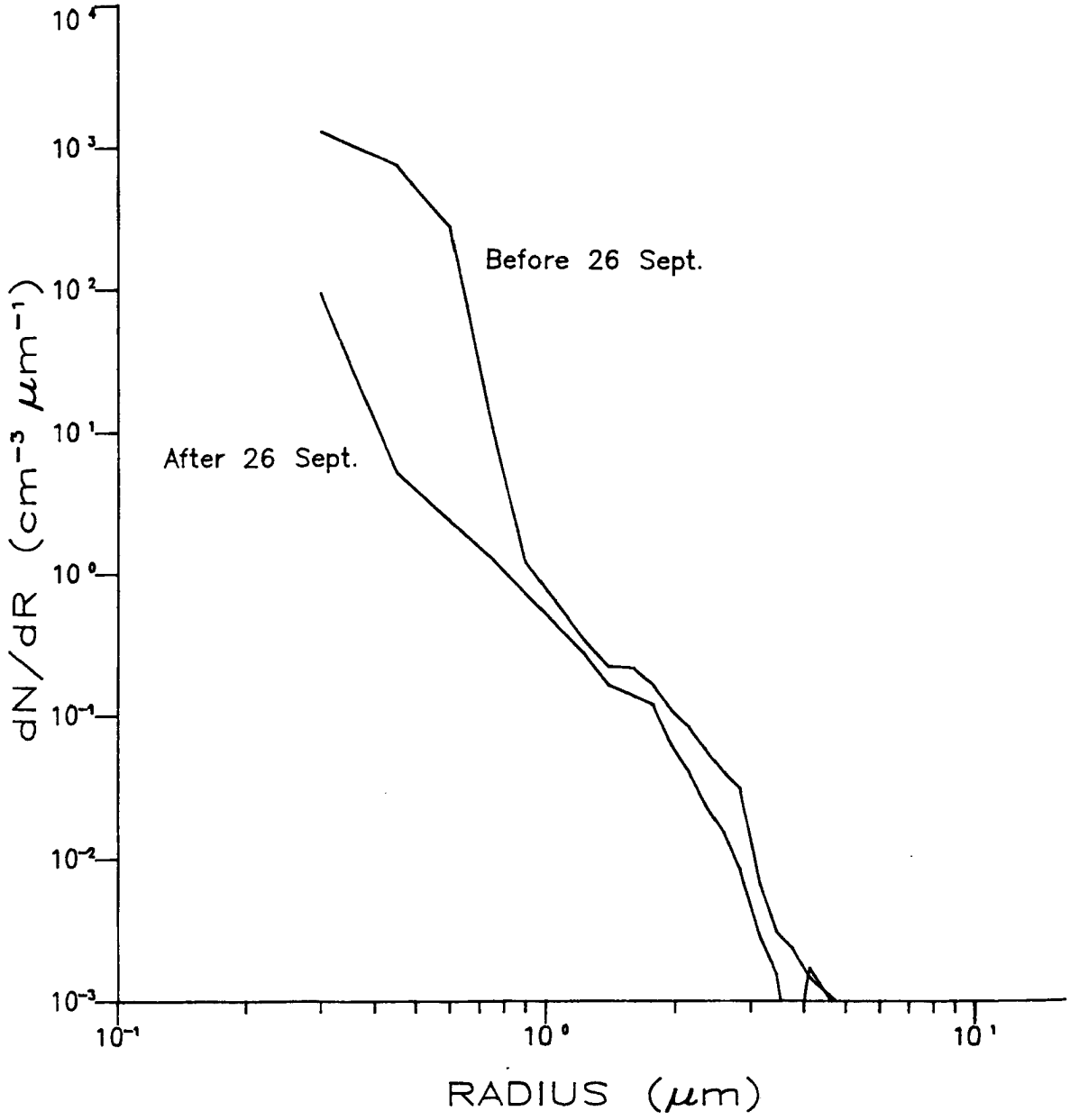

Figure 4.20 Average size distriution of particles above the boundary layer for spirals before and after 26 September 1982.

particles of radius less than 1 μm were found in numbers two orders of magnitude higher before 26 September than after. Also, examination of figures in Appendix D reveals that during the first half of the experiment, the relative humidity above the boundary layer was typically less than 30%. Therefore, the relatively high upper level extinction during the first half of the experiment (prior to 26 September) was due to higher total numbers of relatively small particles ($r<1.0\mu m$) and not due to particle size increase with relative humidity.

Figure 4.21 is a schematic of a mechanism for the formation of significant layers of small particles above the marine boundary layer. The sea-land breeze which develops by early afternoon meets the rising convective plumes on-shore, thereby mixing marine particles with rural and probably urban particles. On-shore, thermal convection then transports the particle mixture throughout the convective mixing layer (up to several kilometers). Since the region is dominated by the subsidence of the eastern side of the sub-tropical high pressure system, the rising convective plumes spread into stable layers above the top of the marine boundary layer.

The absence of these particles after the middle of the experiment can be accounted for by the passage of a precipitating cold front on 26th September, 1982. The front was responsible for up to two inches of rain in the Los Angeles area. The precipitaion scavenged the upper level particles and the post-frontal air mass had very few particles above the boundary layer.

The layers of particles above the boundary layer apparent on the 5th and 6th of October also had higher levels of relative humidity (see Figures 4.6 and 4.18). These layers are argued the beginnings of off-

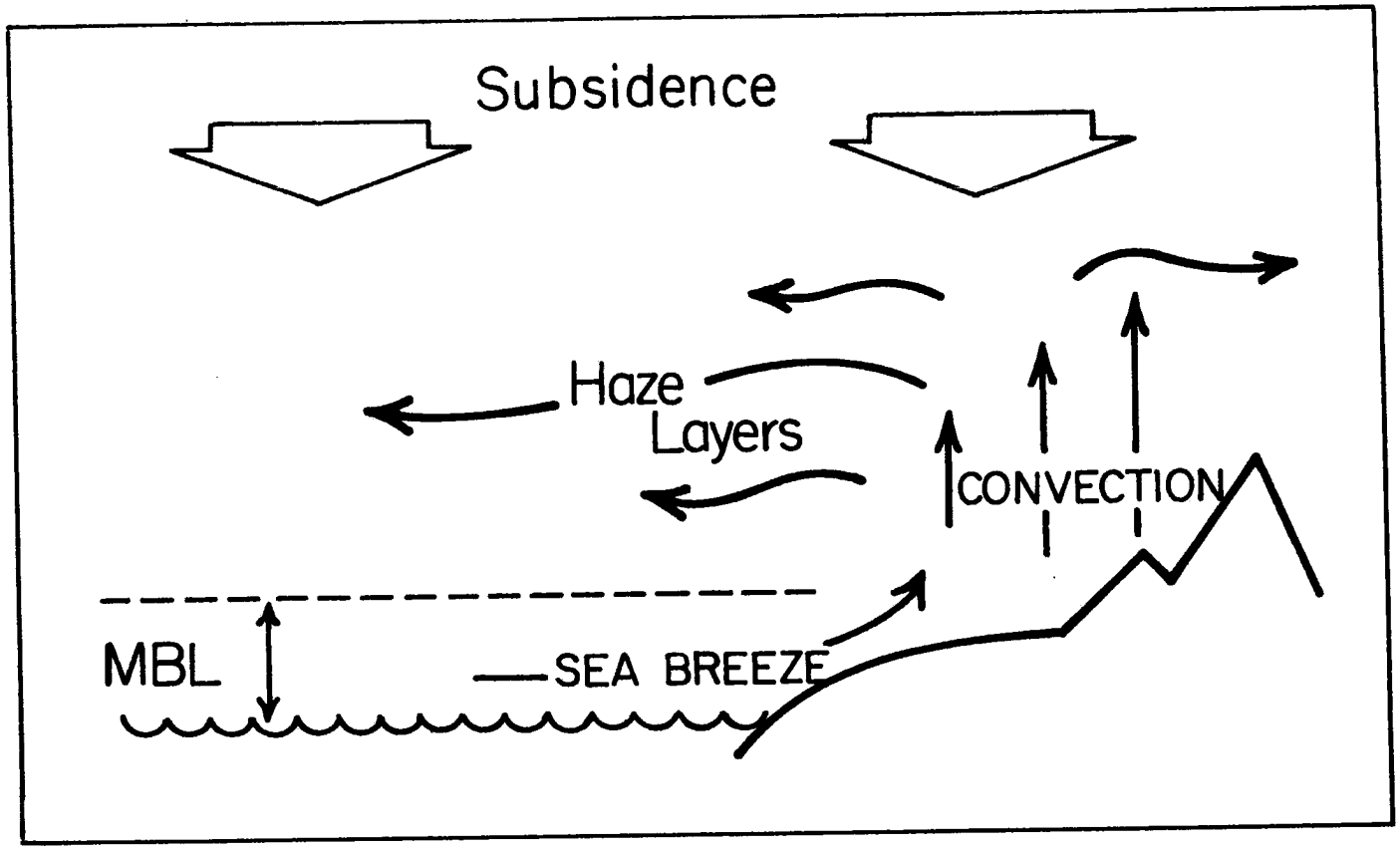

Figure 4.21 Schematic of a mechanism for the formation of significant layers of small particles above the boundary layer.

shore transport of particles and boundary layer moisture by the mechanism described in Figure 4.21.

4.4.2 Satellite-Detection of Upper Level Particles.

The presence of significant numbers of particles above the marine boundary layer limits the extent to which upwelling radiance depends on characteristics of the marine boundary layer. A method to detect the presence of upper level particles is therefore needed if satellite-detected radiance is to be used to characterize the marine boundary layer.

The parameters in Equation (4.2) all vary with wavelength. Particles above the boundary layer, which result from transport off-shore of continental and urban type particles, differ from marine particles in that they are smaller in size and absorb more radiation ($\omega_o < 1$). Therefore, the aerosol-dependent parameters in Equation (4.2) should vary with wavelength differently for upper level particles than marine particles.

Table 4.3 lists the values of scattering extinction coefficient, β_{scat}, and single scattering albedo, ω_o, from the Shettle and Fenn (1979) models of rural, urban and marine particles at .694 μm and 1.06 μm wavelengths. It is clear from Table 4.3 that ω_o and β_{scat} (and thus τ_A) vary more with wavelength for rural and urban particles than for marine particles. Also, β_{scat} and ω_o are larger at .694 μm than at 1.06 μm wavelength. The phase function, $p(\theta)$, varies only slightly over this wavelength change. The net result is that the aerosol-dependent terms, ω_o, $p(\theta)$ and τ_A, are larger at red wavelengths than at near-infrared wavelengths for rural and urban particles. For marine particles ω_o, $p(\theta)$ and τ_A are relatively constant with wavelength.

Table 4.3 Scattering coefficient and single scattering albedo vs composition and wavelength

		50% RH		80% RH
	λ	Rural	Urban	Marine
β_s	0.694	0.106	0.091	0.207
	1.06	0.050	0.049	0.191
ω	0.694	0.934	0.635	0.994
	1.06	0.865	0.567	0.992

A ratio can be formed of Equation (4.2) applied at red and near-infrared wavelengths such that:

$$\frac{L_{RED}}{L_{NIR}} \alpha \frac{(\omega_o p \tau_A)_{RED}}{(\omega_o p \tau_A)_{NIR}} \quad (4.4)$$

The right-hand side of Equation (4.4) will be larger for upper level particles than for marine particles because of the larger variation with wavelength. The ratio of red radiance to near-infrared radiance should, therefore, be larger in cases where total optical depth has significant contribution from upper level particles.

Figure 4.22 illustrates values of the ratio of red radiance (Channel 1 of AVHRR and Channel 4 of CZCS) to near-infrared radiance (Channel 2 of AVHRR and Channel 5 of CZCS) during the experiment period. The ratio decreases after the passage of the precipitating cold front on 26 September. The bracketed values indicate the fraction of the total optical depth which is due to upper level particles. The sharp decrease in these values and the ratio values at frontal passage indicates the front removed the upper level particles present at the beginning of the experiment.

4.5 Discussion of Results.

Results from the 5 October, 1982 case study and the comparisons of spirals throughout the experiment show that satellite-detected radiance is positively correlated with aerosol optical depth. On a given day within a small geographical region, as on 5 October, 1982, the direct relationship between aerosol optical depth and satellite-detected radiance shows a high correlation (see Figure 4.5). When comparing measurements from different days or over large geographical regions,

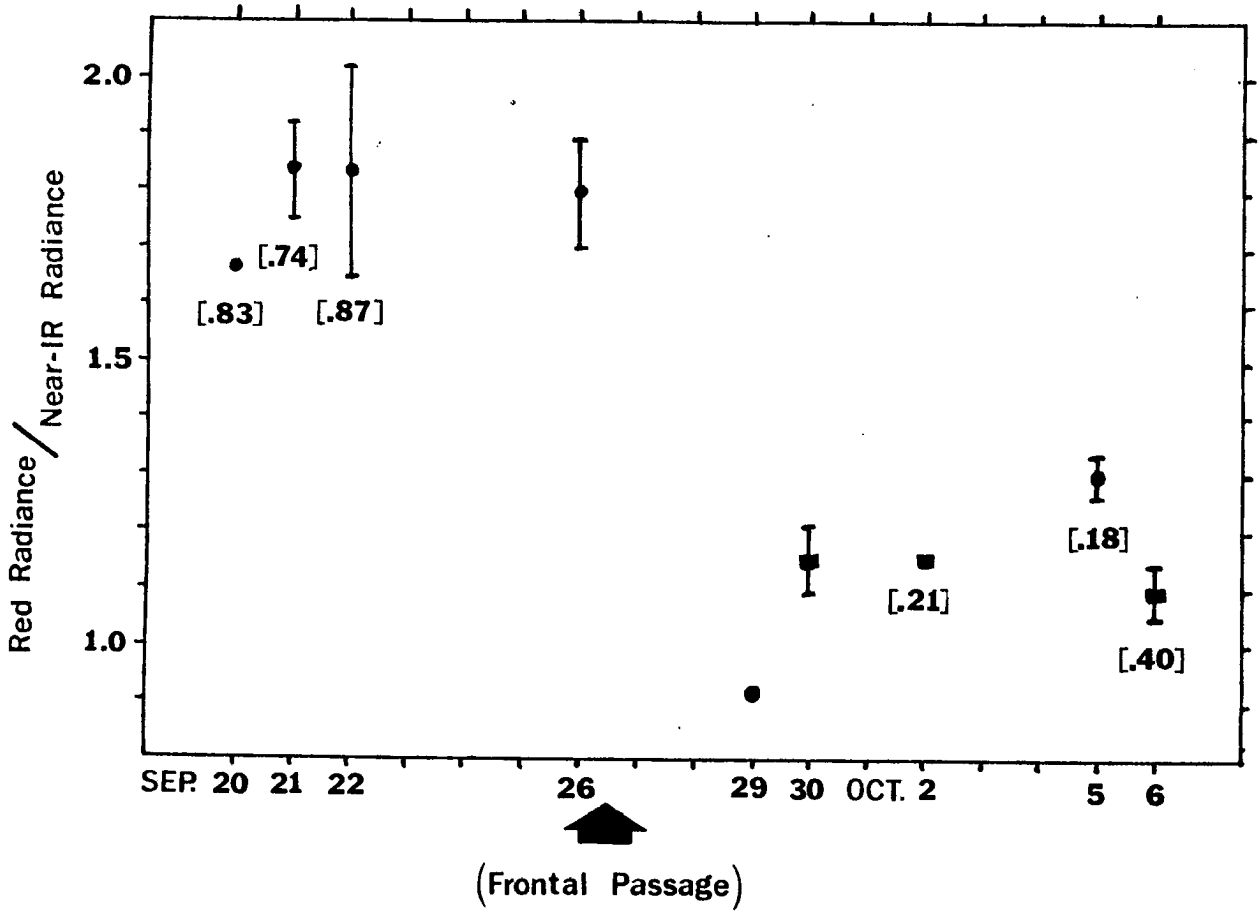

Figure 4.22 The ratio of red radiance to near-infrared radiance during the experiment period. The points indicate the mean of the spiral locations on each day. The error bar shows the standard deviation about the mean. Circles are AVHRR values and squares are CZCS values. Bracketed values indicate the fraction of the total optical depth which is due to upper level particles.

variations due to sun-earth-satellite geometry need to be accounted for. The inclusion of satellite-view geometry into the relationship accounts for most of the variation (see Table 4.2).

Relative humidity measured by the aircraft system and calculations of extinction from the aircraft-measured particle characteristics have been compared. The results indicate that the expected relationship between relative humidity, particle growth and thus, extinction, holds within the marine boundary layer. Further, the relationship holds over several days and in different locations within the experiment region (see Figure 4.15).

The relationship between boundary layer relative humidity and extinction implies that upwelling radiance, which depends on the vertical integration of extinction, should be related to relative humidity. Comparison of satellite-detected radiance, with measured boundary layer relative humidity, verifies this relationship (see Figure 4.16). However, three conditions limit the direct relationship between satellite-detected radiance and boundary layer relative humidity.

First, wind speed variation may contribute to variations in extinction and thus, optical depth. The scatter in the relationship between extinction and relative humidity shown in Figure 4.15 is believed due to variations in the total number of aerosol particles caused by variations of wind speed. The scatter in this relationship adds to the scatter in the relationship between satellite-detected radiance and relative humidity.

Second, contributions to the total aerosol optical depth by particles above the marine boundary layer limit the extent to which upwelling radiance depends on boundary layer extinction and thus

relative humidity. During the first half of the experiment, significant numbers of particles existed above the boundary layer. However, it was found that the ratio of satellite-detected radiance at red and near-infrared wavelengths can be used to detect the presence of significant amounts of upper level particles (see Figure 4.22). Therefore, conditions where upper level particles add uncertainty to the relationship between satellite-detected radiance and boundary layer relative humidity can be detected.

Third, the depth of the marine boundary layer may vary. Since optical depth is the vertical integration of extinction, the value of extinction through the boundary layer and the depth of the boundary layer affect the total optical depth. On a given day, if the marine boundary layer depth remains constant, relative variations of satellite-detected radiance may be related to relative humidity variations. On 6 October, 1982, significant boundary layer extinction and relative humidity variation was masked in the satellite image by boundary layer depth variaion (see Figures 4.18 and 4.19).

This third condition is very limiting. It is apparent from the Santa Ana example described in Appendix A that gross variations of relative humidity are detectable in satellite images. However, the marine boundary layer depth must be known if satellite-detected radiance is to be used to quantitatively investigate marine boundary layer relative humidity variations. Some information on boundary layer depth may be obtained from coastal rawinsonde measurements. Further research is needed, however, to formulate remote sensing techniques which can provide boundary layer depth.

5.0 CONCLUSIONS

Certain new satellite sensors are sensitive to aerosol optical depth variations. For example, brightness variations in satellite images of cloud-free, ocean regions were hypothesized by Fett and Isaacs (1979) to be related to marine aerosol particles. The objective of this dissertation was to quantitatively examine the relationship between marine aerosol particles and satellite-detected radiance. Further, the causes of particle variations which lead to upwelling radiance variation, particularly relative humidity effects, were investigated.

Both theoretical and experimental approaches were taken to attain these objectives. First, a two-stream radiative transfer model was used to calculate upwelling radiance variations caused by calculated aerosol particle variations. Variations of particle scattering characteristics due to composition, total number (due to wind speed variation), and size (due to relative humidity variation) were investigated.

Second, an experiment designed to relate near-simultaneous satellite images to marine boundary layer characteristics was described. Satellite images were analyzed in real-time and used to direct an aircraft to regions of brightness variations detected in the images. The aircraft measured atmospheric state variables and aerosol particle characteristics from the surface to 1524 m in the regions of interest.

This set of measurements was used to compare satellite-detected radiance with known aerosol particle characteristics and atmospheric state variables.

A summary of conclusions from the theoretical and experimental results follows:

1. Satellite-detected radiance is positively correlated with aerosol optical depth; a result consistent with Griggs (1975) and a corroboration of Fett and Isaacs (1979) and Hindman, et al. (1984). Within a small geographical region on a given day, upwelling radiance is directly related to aerosol optical depth (Figure 4.5). However, when comparing measurements from different days or over a large geographical area the effect of sun-earth-satellite geometry must be accounted for (Figures 4.25 and 4.26).

2. Marine boundary layer radiative extinction is related to relative humidity (Figures 4.7 and 4.27). The relationship follows that which is expected from previous measurements and particle growth theory.

3. Since satellite-detected radiance is related to total extinction (optical depth) and extinction is related to relative humidity, satellite-detected radiance is related to relative humidity (Figure 4.28).

4. The relationship between boundary layer relative humidity and extinction is limited by wind-generated particle variations. However, theoretical considerations indicate that if prevailing wind speed variations are less than about 5 knots, typical relative humidity variations cause greater upwelling radiance variations than those caused by wind speed variations.

5. The presence of significant numbers of particles above the boundary layer adds uncertainty to the relationship between upwelling radiance and boundary layer relative humidity. However, the ratio of satellite- detected radiance at red and near infrared wavelengths can be used to detect the presence of significant amounts of upper level particles (Figure 4.34). Therefore, situations where large uncertainties are added to the radiance-relative humidity relationship by upper level particles can be determined.

These results show that satellite images may be used to monitor characteristics of the marine boundary layer. Where there are few particles above the boundary layer, optical properties of the boundary layer are derivable from the relationship between upwelling radiance and aerosol optical depth. Also, when wind-speed variations are small, boundary layer relative humidity variations may be investigated from space. This tool will aid in studies of boundary layer processes, air-sea interactions, cloud development and others which relate to marine aerosol particles, relative humidity and their variation.

REFERENCES

Bolton, D., 1980: The Computation of Equivalent Potential Temperature. Mon. Wea. Rev., 108, 1046-1053.

Carlson, T. N., 1979: Atmospheric Turbility in Saharan Dust Outbreaks as Determined by Analysis of Satellite Brightness Data. Mon. Wea. Rev., 107, 322-335.

Coakley, J. A., Jr., and P. Chylek, 1975: The Two-Stream Approximation in Radiative Transfer: Including the Angle of the Incident Radiation. J. Atmos. Sci., 32, 409-418.

Covert, D. S., R. J. Charlson, and N. C. Ahlquist, 1972: A Study of the Relationship of Chemical Composition and Humidity of Light Scattering by Aerosol. J. Appl. Meteor., 11, 968-976.

Cox, C. C., and W. Munk, 1954: Measurement of the Roughness of the Sea Surface from Photographs of the Sun's Glitter. J. Opt. Soc. Am., 44, 838-850.

Durkee, P. A., E. E. Hindman, and T. H. Vonder Haar, 1984: The Detection of Marine Haze with Meteorological Satellites. In Hygroscopic Aerosols in the Planetary Boundary Layer, 171-180. Edited by L. H. Ruhnke and A. Deepak, A. Deepak Publishing, Hampton, VA.

Dytch, H. E., and N. J. Carrera, 1976: Cloud Droplet Spectrometry by Means of Light-Scattering Techniques. Atmos. Tech., 8, 10-16.

Fett, R. W., and R. G. Isaacs, 1979: Concerning Causs of 'Anomalous Gray Shades' in DMSP Visible Imagery. J. Appl. Meteor., 18, 1340.

Fitzgerald, J. W., 1975: Approximation Formulas for the Equilibrium Size of an Aerosol Particle as a Function of its Dry Size and Composition and the Ambient Relative Humidity. J. Appl. Meteor., 14, 1044-1049.

Fitzgerald, J. W., 1979: On the Growth of Aerosol Particles with Relative Humidity. NRL Memorandum Report 3847, Naval Research Laboratory, Washington, D.C.

Fitzgerald. J. W., W. A. Hoppel, and M. A. Vietti, 1982: The Size and Scattering Coefficient of Urban Aerosol Particles at Washington, DC as a Function of Relative Humidity. J. Atmos. Sci., 39, 1838-1852.

Gordon, H. R., 1978: Removal of Atmospheric Effects from Satellite Imagery of the Oceans. Appl. Opt., 17, 1631-1636.

Gordon, H. R., and D. K. Clark, 1980: Atmospheric Effects in the Remote Sensing of Phytoplankton Pigments. Boundary Layer Meteorol., 18, 299-313.

Griggs, M., 1975: Measurement of Atmospheric Aerosol Optical Thickness Over Water Using ERTS-1 Data. J. Air Pollut. Control Assoc., 25, 622-626.

Griggs, M., 1979: Satellite Observations of Atmospheric Aerosols During the EOMET Cruise. J. Atmos. Sci., 36, 695-698.

Hanel, G., 1976: The Properties of Atmospheric Aerosol Particles as Functions of the Relative Humidity at Thermodynamic Equilibrium with the Surrounding Moist Air. In Advances in Geophysics, 19, 73-188. Edited by H. E. Landsberg and J. Van Mieghen, Academic Press, New York.

Hindman, E. E., P. A. Durkee, P. C. Sinclair, and T. H. Vonder Haar, 1984: Detection of Marine Aerosol Particles in Coastal Zones Using Satellite Imagery. Intl. J. Remote Sensing, 5, In press.

Hobbs, P. V., L. F. Radke and E. E. Hindman, 1976: An Integrated Airborne Particle Measuring Facility and Its Preliminary Use in Atmospheric Aerosol Studies. J. Aerosol Sci., 7, 195-211.

Hovis, W., 1978: The Coastal Zone Colo Scanner (CZCS) Experiment in the NIMBUS-7 User's Guide. Goddard Space Flight Center. Greenbelt, MD.

Isaacs, R. G., 1980: Investigation of the Effect of Low Level Maritime Haze on DMSP VHR and LF Imagery. NAVENVPREDRSCHFAC CR 80-06.

Jensen, D. R., P. Jeck, G. Trusty, and G. Schacher, 1980: Intercomparison of PMS Particle Size Spectrometers. Technical Report 555, Naval Ocean Systems Center, San Diego, CA.

Kaufman, Y. J., 1979: Effect of the Earth's Atmosphere on Contrast for Zenith Observations. J. Geophys. Res., 84, C6, 3165-2451.

King, W. D., D. A. Parkin, and R. J. Handsworth, 1978: A Hot-Wire Liquid Water Device Having Fully Calculable Response Characteristics. J. Appl. Meteor. 17, 1809-1813.

Koepke, P., and H. Quenzel, 1979: Turbidity of the Atmosphere Determined From Satellite: Calculation of Optimum Viewing Geometry. J. Geophys. Res., 84, 7847.

_____, 1981: Turbidity of the Atmophere Determined From Satellite: Calculation of Optimum Wavelength. J. Geophys. Res., 86, 9801.

Lauritson, L., G. J. Nelson, and F. W. Porton, 1979: Data Extraction and Calibration of TIROS-N/NOAA Radiometers. NOAA Tech. Mem. NESS-107.

Lentz, W. J., 1982: The Visioceiliometer: A Portable Visibility and Cloud Ceiling height LIDAR. TR-0105, Atmos. Sci. Lab., WSMR, NM, 4-5 pp.

Liou, K. N., 1980: An Introduction to Atmospheric Radiation. Academic Press, New York.

Lovett, R. F., 1978: Quantitative Measurement of Airborne Sea-Salt in the North Atlantic. Tellus, 30, 358-364.

McCartney, E. J., 1976: Optics of the Atmosphere: Scattering by Molecules and Particles. J. Wiley, New York.

McClintock, M., A. McLellan, and L. A. Sromovsky, 1971: Satellite Measurements of Spectral Turbidity and Albedo, and Their Rates of Change. Report to the Environmental Protection Agency, UWI-SSEC-GAP-71-003, July 30, 1971.

McConaughy, R., 1982: Personal Communication. Ball Aerospace Corporation, Boulder, CO.

Meador, W. E., and W. R. Weaver, 1980: Two-Stream Approximations to Radiative Transfer in Planetary Atmospheres: A Unified Description of Existing Methods and a New Improvement. J. Atmos. Sci., 37, 630-643.

Neckel, H., and D. Labs, 1974: Improved Data of Solar Spectral Irradiance From 0.33 to 1.25 μ. Solar Physics, 74, 231-249.

Noonkester, V. R., 1980: Marine Aerosols and Calculated Optical Properties in a Convective Layer Near San Nicolas Island. Technical Note 925, Naval Ocean Systems Center, San Diego, CA.

Noonkester, V. R., 1981: Aerosol Size Spectra in a Convective Marine Layer with Stratus: Results From Airborne Measurements near San Nicholas Island, CA. J. Appl. Meteor., 20, 1076-1080.

Norton, C. C., F. R. Mosher, B. Hinton, D. W. Martin, D. Santek, and W. Kuhlow, 1980: A Model for Calculating Desert Aerosol Turbidity Over the Oceans From Geostationary Satellite Data. J. Appl. Meteor., 19, 633-644.

Ramsey, R. C., 1968: Study of the Remote Measurement of Ocean Color. Final Report, TRW, NASW-1658.

Schwalb, A., 1978: The TIROS-N/NOAA A-G Satellite Serie. NOAA Tech. Mem. NESS-95.

Shettle, E. P., and R. W. Fenn, 1979: Models for the Aerosols of the Lower Atmosphere and the Effects of Humidity Variations on Their Optical Properties. AFGL-TR-79-0214 Air Force Geophysics Laboratories, Hanscom AFB, MA.

Wiscombe, W. J., 1979: Mie Scattering Calculations: Advances in Technique and Fast, Vector-Speed Computer Codes. NCAR Technical Note NCAR/TN-140+STR. National Center of Atmospheric Research, Boulder, CO.

Wiscombe, W. J., 1980: Improved Mie Scattering Algorithms. Applied Optics, 19, 1505-1509.

Woodcock, A. H., 1953: Salt Nuclei in Marine Air as a Function of Altitude and Wind Force. J. Meteorol., 10, 362-371.

APPENDIX A

Effects of Santa Ana Winds on Satellite-Detected Brightness Variations

An example of a regional-scale satellite-detected brightness variation is presented in this appendix. This example illustrates the use of on-shore meteorological measurements to investigate the causes of near-coastal brightness variations.

Figure A.1 is a time series of potential temperature and relative humidity from soundings measured at Montgomery Field, San Diego, California. The time series is from 8 June through 20 June, 1981. A well defined marine boundary layer, characterized by near constant potential temperature and high relative humidity, is apparent in Figure 1.1 from 8 June through 13 June. At about 0000Z on 14 June a drastic change in the vertical profile of potential temperature and relative humidity occurred. Values of relative humidity at the surface dropped to $< 20\%$ while the potential temperature at the surface increased as the boundary layer dissipated. These changes resulted from warm, dry air flowing off-shore. The winds associated with this off-shore flow are known as Santa Ana winds in southern California.

This particular Santa Ana event lasted from 14 June through about 17 June at San Diego. Several meteorological records were broken during this period. On 16 June the high temperature at San Diego was 99°F, breaking the record high on that date by 16°F. The hot surface temperatures contributed to unusually warm ocean surface temperatures

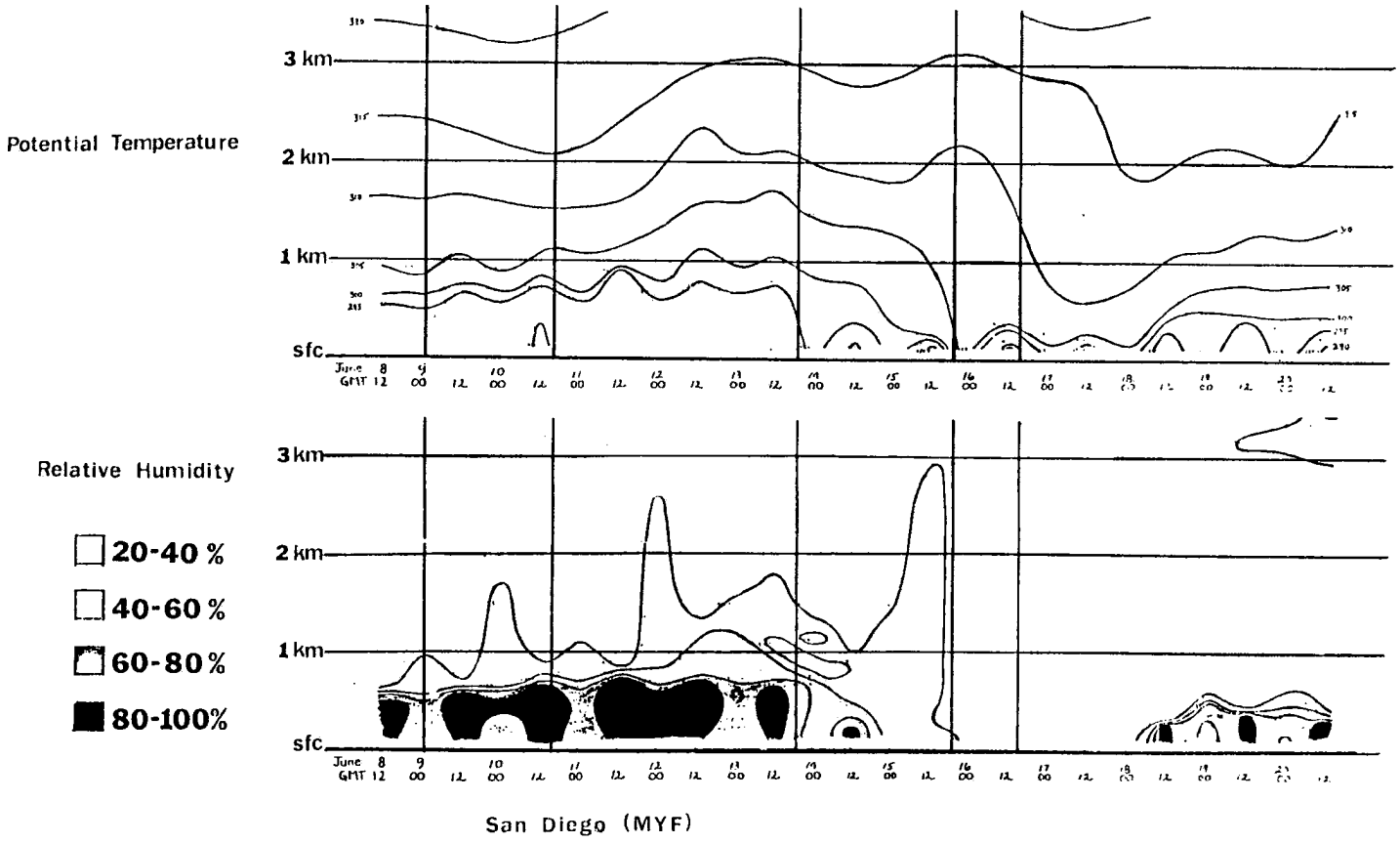

Figure A.1 Time series from 8 to 20 June 1981 of potential temperature and relative humidity from soundings measured at Montgomery Field, San Diego.

near San Diego during this period. One week after this event, the ocean surface temperature, recorded at Scripps Institute of Oceanography near San Diego, reached its all time high of 74°F.

The large decrease of relative humidity during the Santa Ana event should result in a large decrease in the sizes of particles near the ocean surface (Fitzgerald, 1979). According to the hypothesis of Fett and Isaacs (1979), the decrease in particle size results in a decrease of scattered solar irradiance. Satellite-detected upwelling radiance should, therefore, be less in regions effected by Santa Ana winds.

The vertical lines in Figure A.1 indicate the times for which satellite images from the NIMBUS-7 Coastal Zone Color Scanner (CZCS) are available. Figure A.2a-d shows the CZCS Channel 5 images from 9, 13, 15 and 16 June, 1981. In the image from 9 June (Figure A.2a), San Diego is engulfed in stratus clouds. Within the cloud-free regions to the north, the satellite-detected brightness varied from the darkest regions near the coast north of Los Angeles to a generally bright region extending off-shore. By 13 June the stratus clouds had moved south of San Diego. The dark region near the coast extends from Santa Barbara to just north of San Diego. The 15 June image, just after the Santa Ana onset, shows a large dark region extending 300 km off-shore at San Diego. On 16 June, the dark region reaches 500 km off-shore. The dark regions in Figure A.2, apparently indicate areas of lower relative humidity. Therefore, the extent of the dark region near the coast delineates the region affected by off-shore winds. The bright patch within the dark region on 16 June is smoke from coastal brush fires.

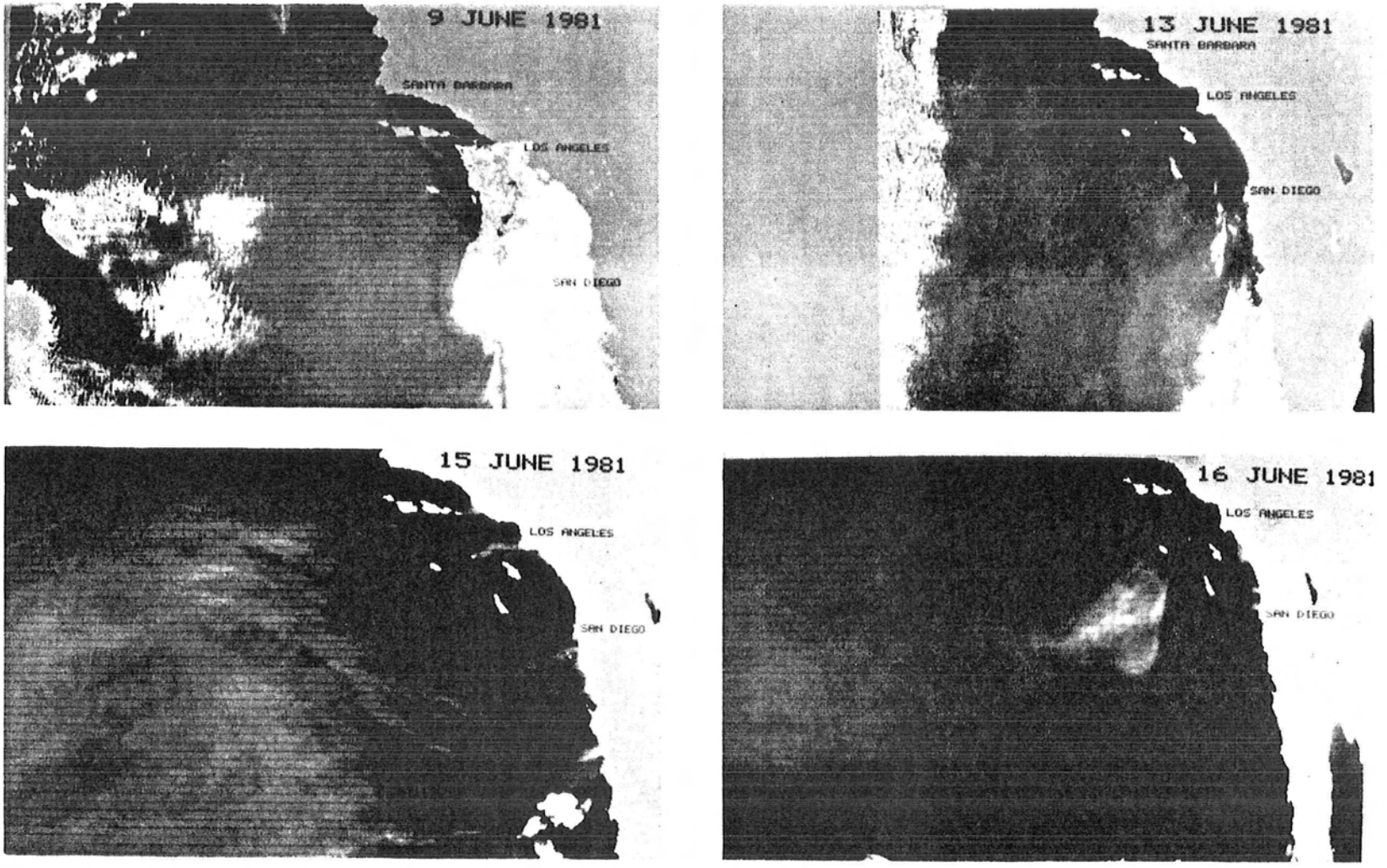

Figure A.2 NIMBUS-7 CZCS Channel satellite images from 9, 13, 15, and 16 June 1981.

APPENDIX B

Conversion of Brightness Counts to Radiance

The NIMBUS-7 CZCS and NOAA-7 AVHRR sensors return image information in the form of digital brightness counts. This appendix describes the conversion of these counts to radiance, a physical quantity.

The NIMBUS-7 CZCS

Eight binary bits are available for digitization of the signal on the CZCS. Thus, brightness counts can range from 0 - 255.

These brightness counts are converted to radiance via the preflight calibration of the CZCS sensor (McConaughy, 1982). The results for Channels 4 and 5 yield the following equations relating brightness count, C_i, and radiance, L_i:

$$\begin{aligned} C_4 &= 88.00\ L_4 - 1.0 \\ C_5 &= 10.62\ L_5 + 0.3 \end{aligned} \qquad \text{(B.1)}$$

These functions are plotted in Figure 3.2. From Equations B.1 and Figure 3.2, it is apparent that CZCS Channel 4 is much more sensitive to radiance changes than Channel 5. Solving for radiance in Equations B.1 yields equations for radiance given the brightness counts:

$$L_4 = 0.0114\ C_4 + 0.114$$

$$L_5 = 0.0942\ C_5 - 0.0282$$

The slope of these functions gives the change of radiance for one brightness count change. These values are used in Section 2.3 to test

the sensitivity of the sensors to calculated upwelling radiance variations.

The NOAA-7 AVHRR

The AVHRR sensor was also preflight calibrated. The system was calibrated with a sun-simulating spherical source. The results are reported by Lauritson, et al (1979) in terms of albedo:

$$A = GX + I \tag{B.2}$$

where A is albedo in percent, X is digital counts, G and I are the calibration constants. The radiance, L, is

$$L = \frac{A}{100} \frac{E_o(\Delta\lambda)}{\pi} \tag{B.3}$$

where $E_o(\Delta\lambda)$ is the solar irradiance over the wavelength band, $\Delta\lambda$, of the sensor. Values of E_o for the AVHRR Channels 1 and 2 are given in Table B.1.

Table B.1 Values of E_o, G and I for the NOAA-7 AVHRR Channels 1 and 2

	λ	$E_o(\mu W cm^{-2} \mu m^{-1})$	G	I
Channel 1	0.6323	162.88	0.1068	-3.44
Channel 2	0.8484	104.04	0.1069	-3.488

The calibration coefficients, G and I, are also given in Table B.1. The result of combining Equations B.2 and B.3 yields the following equations relating brightness count and radiance:

$$X_1 = 18.06\ L_1 + 32.21$$

$$X_2 = 28.25\ L_2 + 32.63$$

These functions are plotted in Figure 3.2. Solving for radiance yields:

$$L_1 = 0.0554\ X_1 - 1.784$$

$$L_2 = 0.0354\ X_2 - 1.155$$

APPENDIX C

Spiral Measurements

This appendix contains figures of the vertical spiral measurements made between 20 September and 6 October 1982. The locations of the spirals are shown in Figure 4.10.

The extinction values were calculated from aircraft measurements of particle size distributions as described in Section 3.1.2. The solid line in the extinction plots is the 20 second mean value (about 40 meters). The dashed lines result from plus or minus one standard deviation from the mean over the 20 second period. The relative humidity and potential temperature values were calculated from aircraft measurements of pressure, temperature and dew-point temperature.

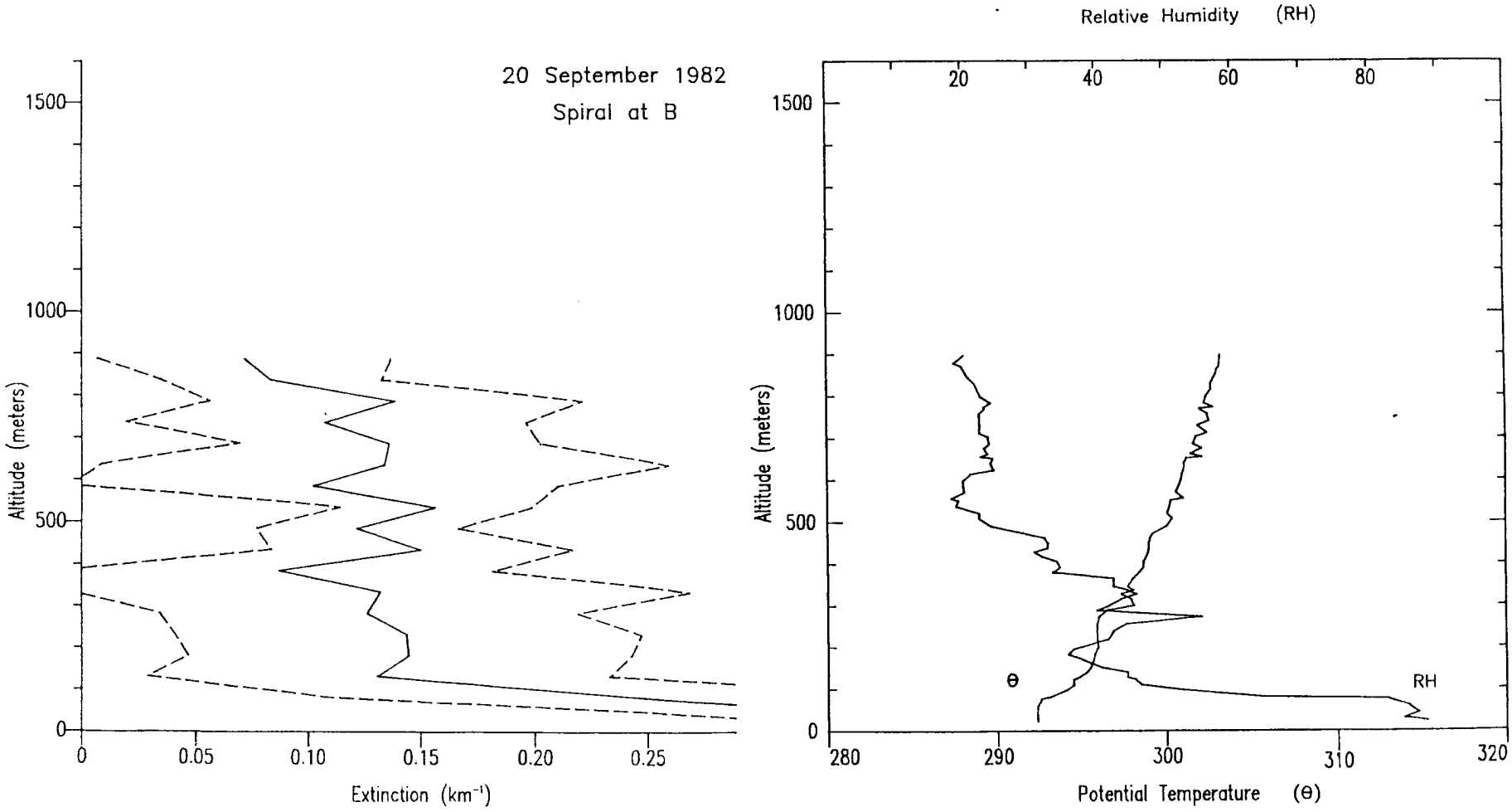

Figure C.1 **Calculated values of extinction, relative humidity and potential temperature from the vertical spiral measurements at point B on 20 September 1982.**

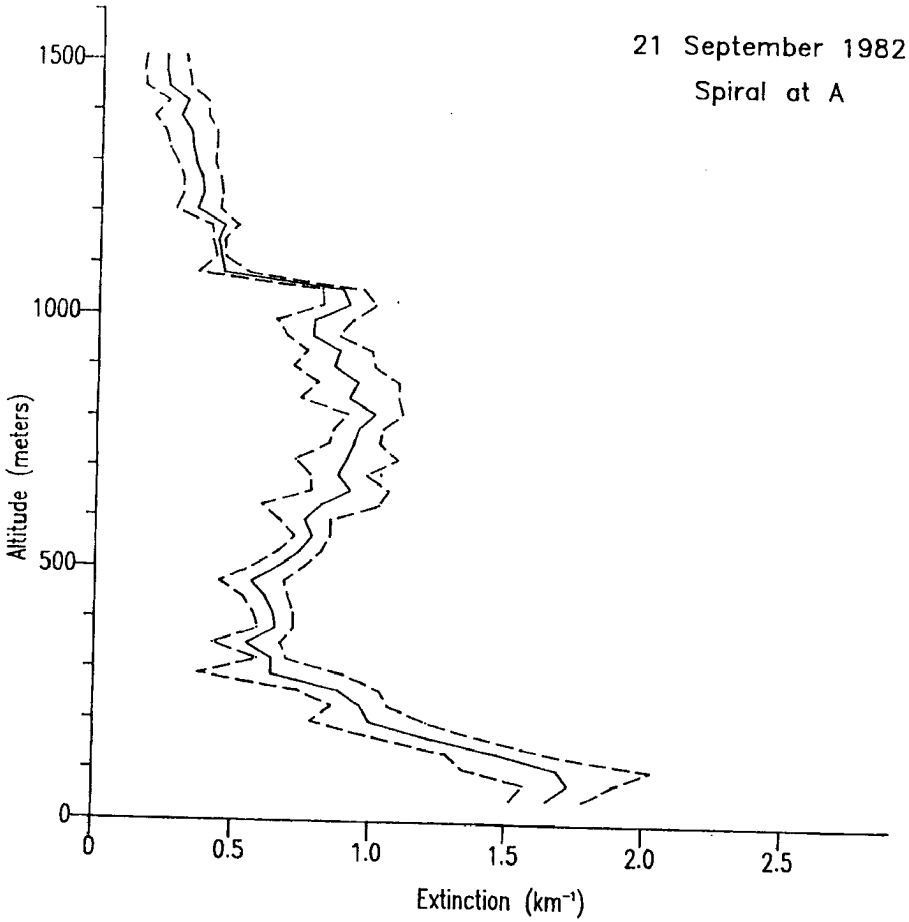

No Data

Available

Figure C.2 **Same as Figure C.1 but for point A on 21 September 1982.**

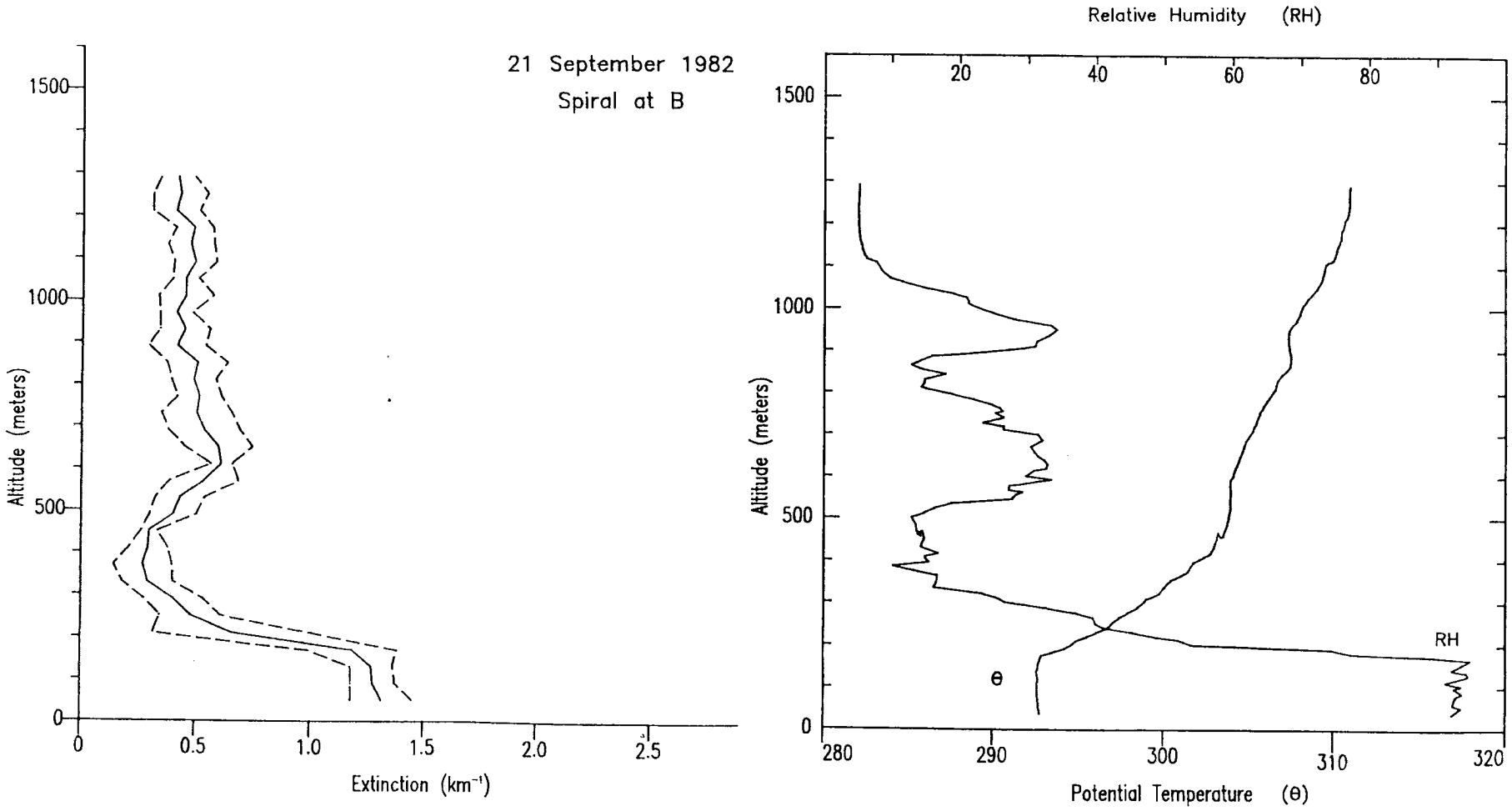

Figure C.3 **Same as Figure C.1 but for point B on 21 September 1982.**

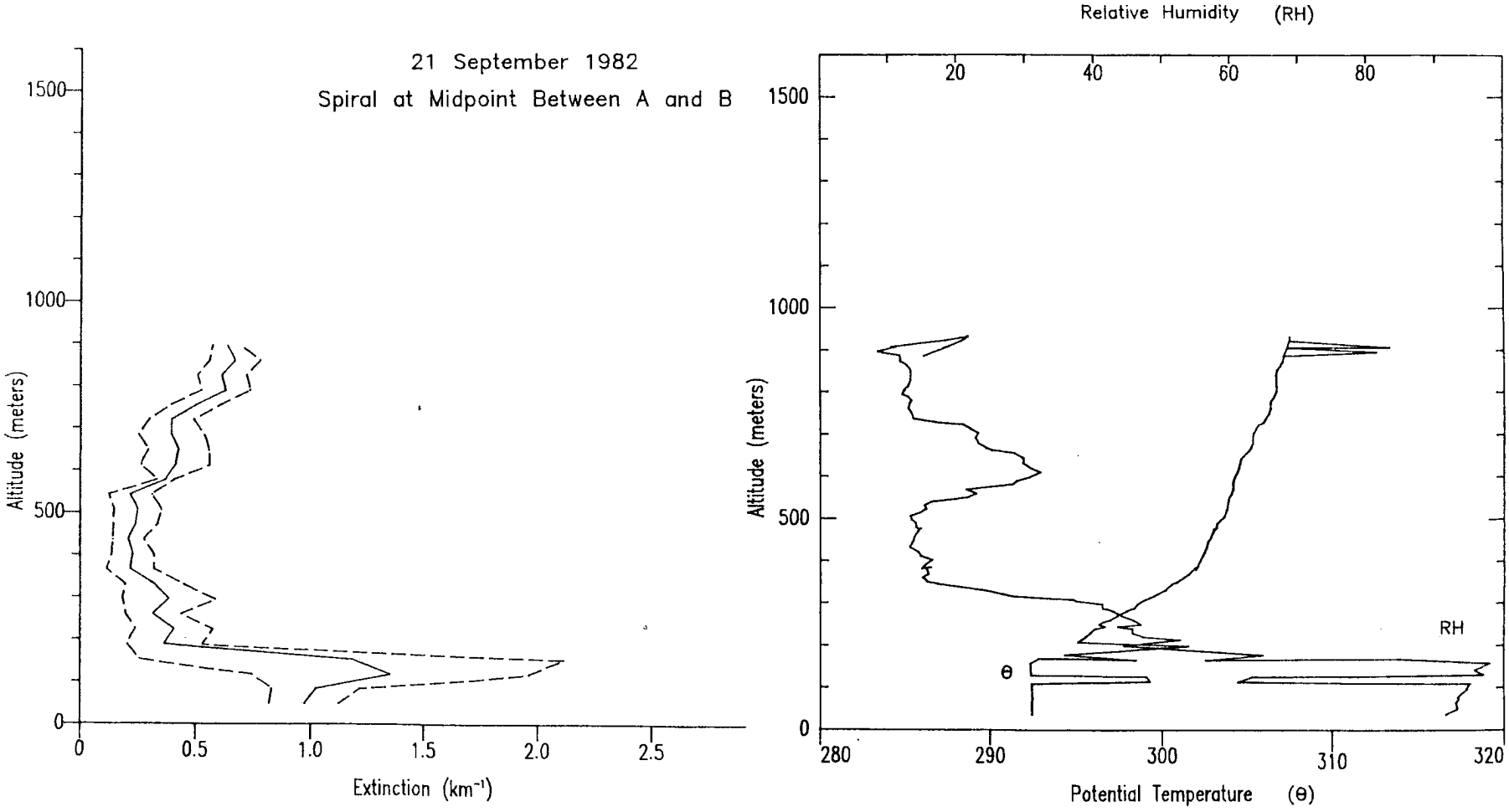

Figure C.4 **Same as Figure C.1 but for the point midway between A and B on 21 September 1982.**

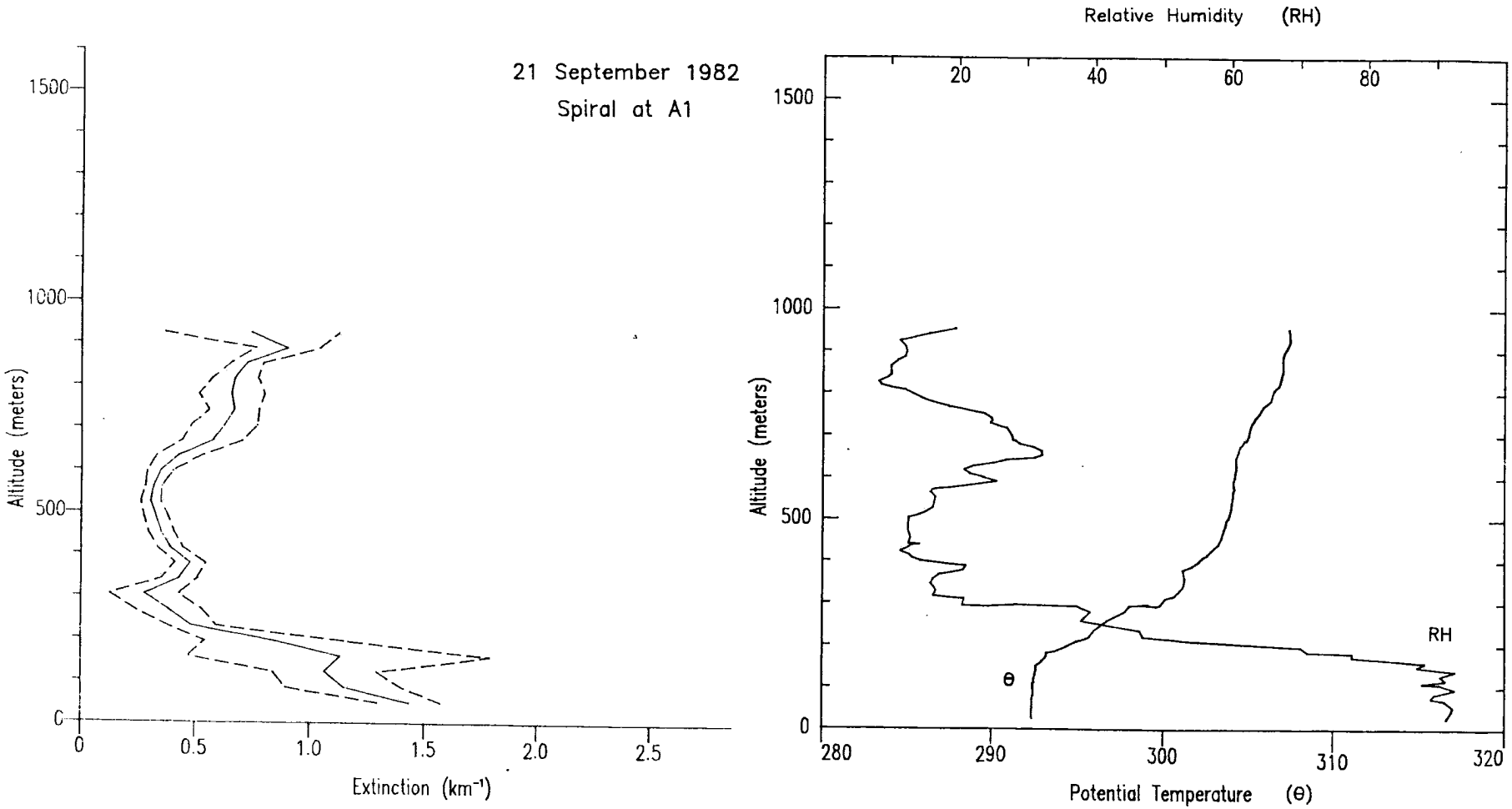

Figure C.5 **Same as Figure C.1 but for point A1 on 21 September 1982.**

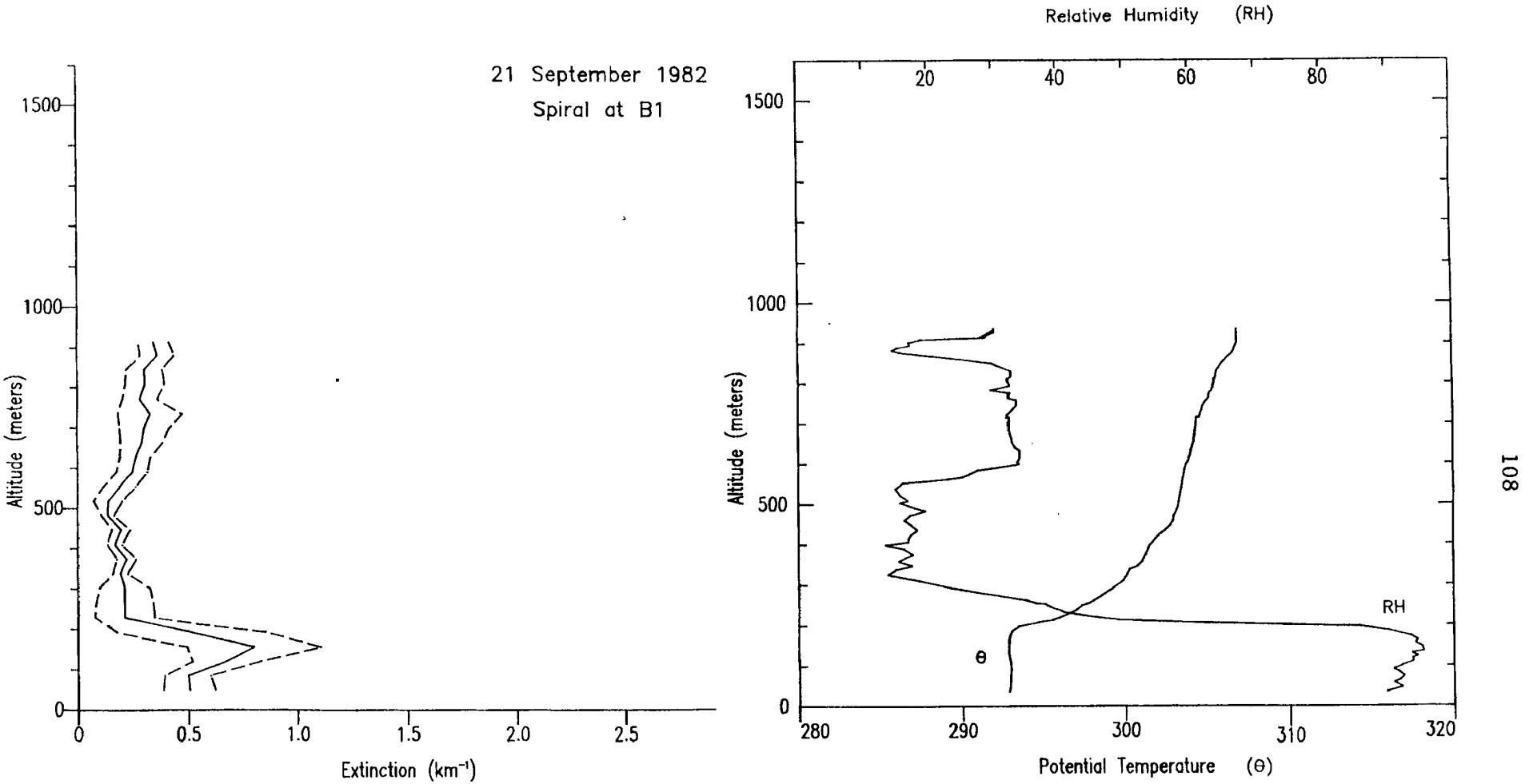

Figure C.6 **Same as Figure C.1 but for point B1 on 21 September 1982.**

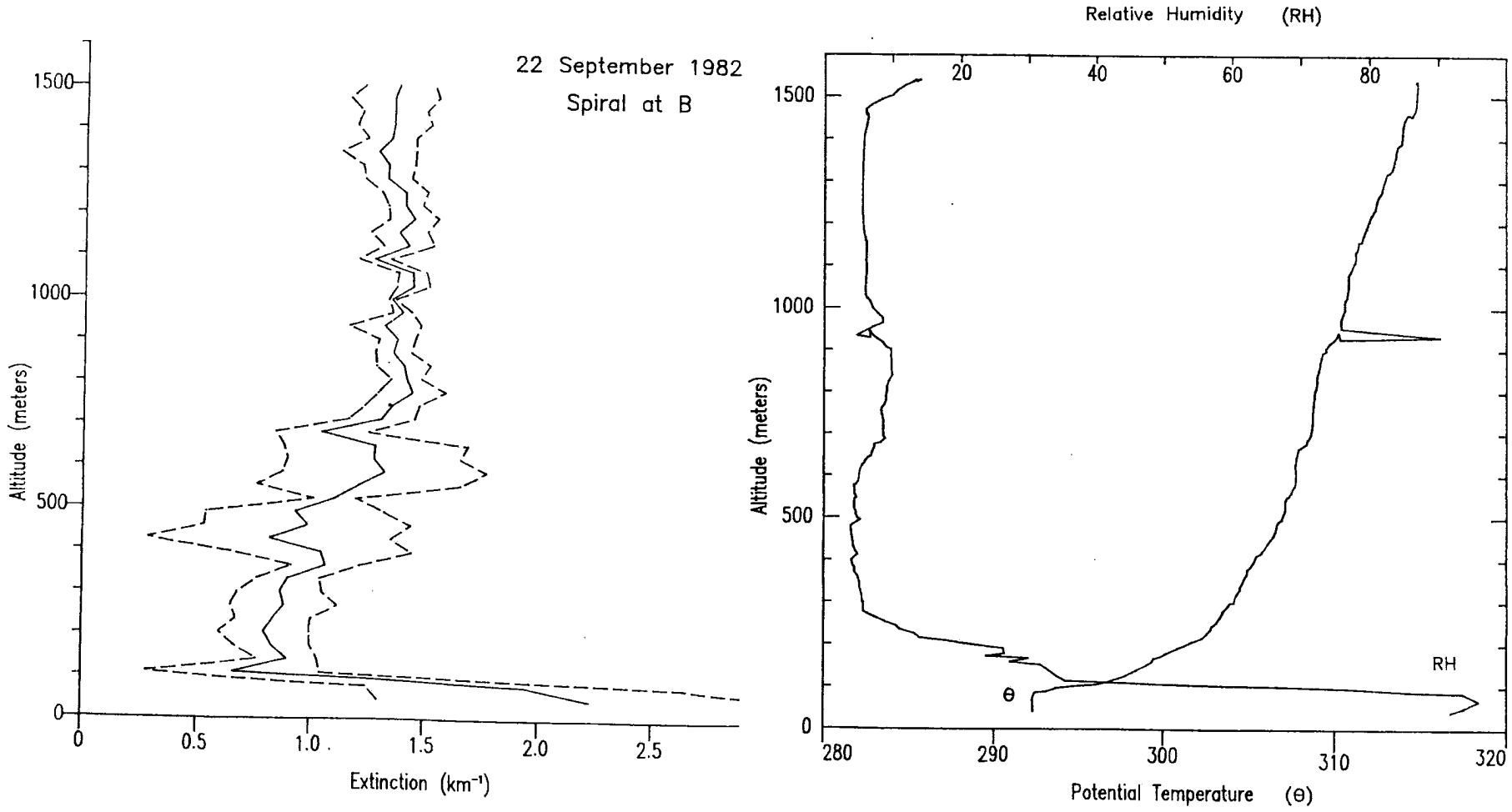

Figure C.7 **Same as Figure C.1 but for point B on 22 September 1982.**

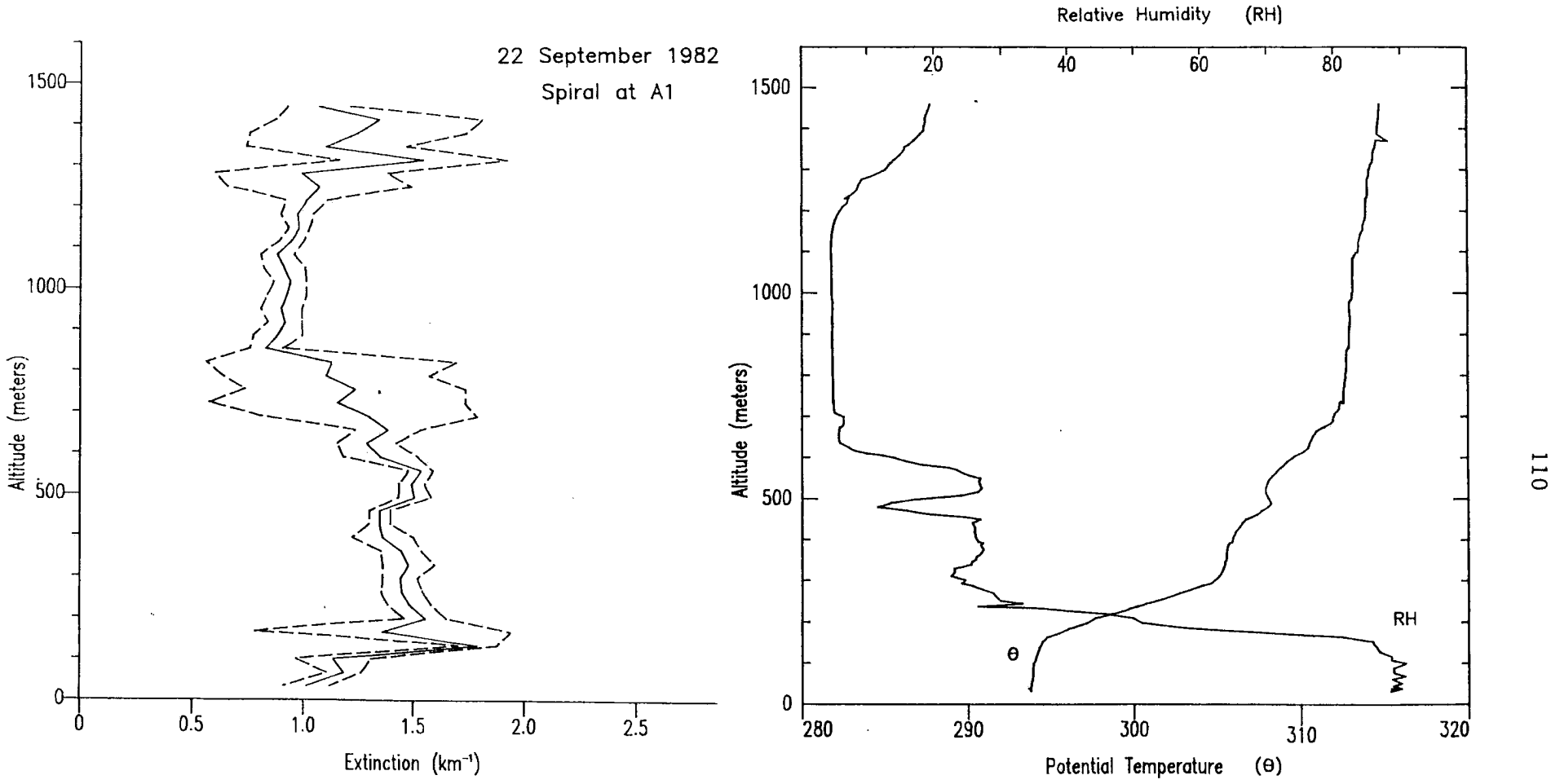

Figure C.8 **Same as Figure C.1 but for point A1 on 22 September 1982.**

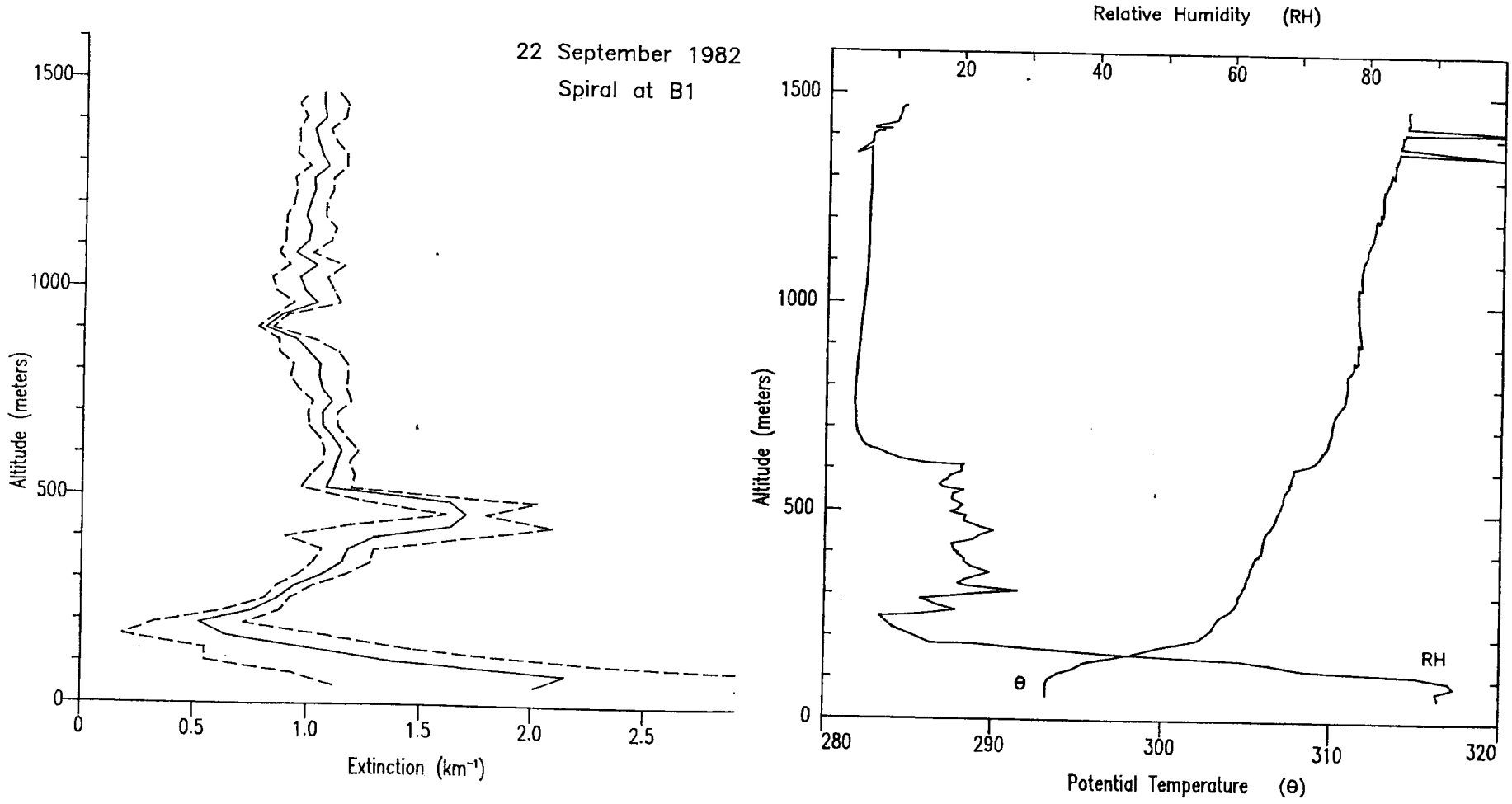

Figure C.9 **Same as Figure C.1 but for point B1 on 22 September 1982.**

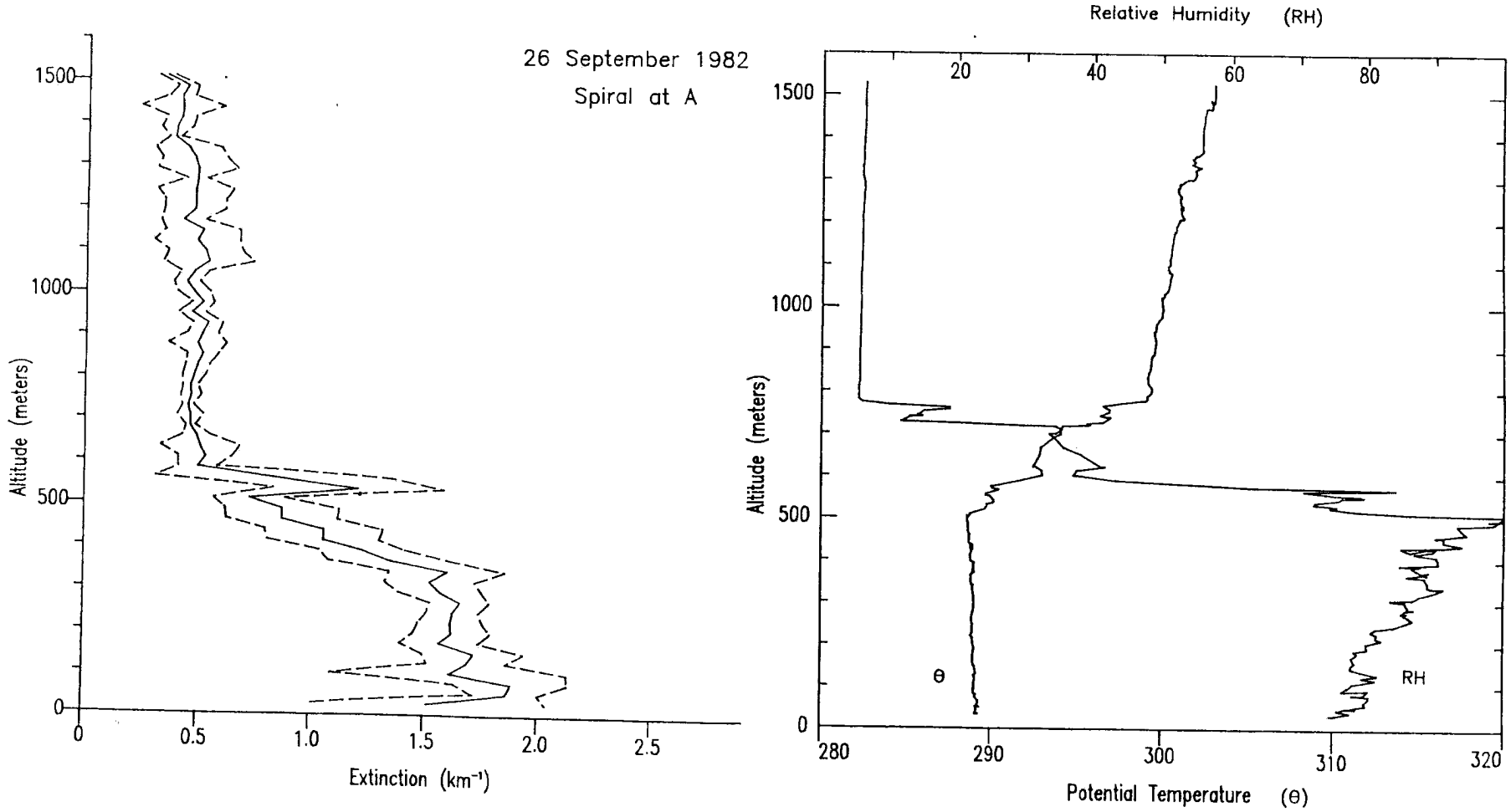

Figure C.10 **Same as Figure C.1 but for point A on 26 September 1982.**

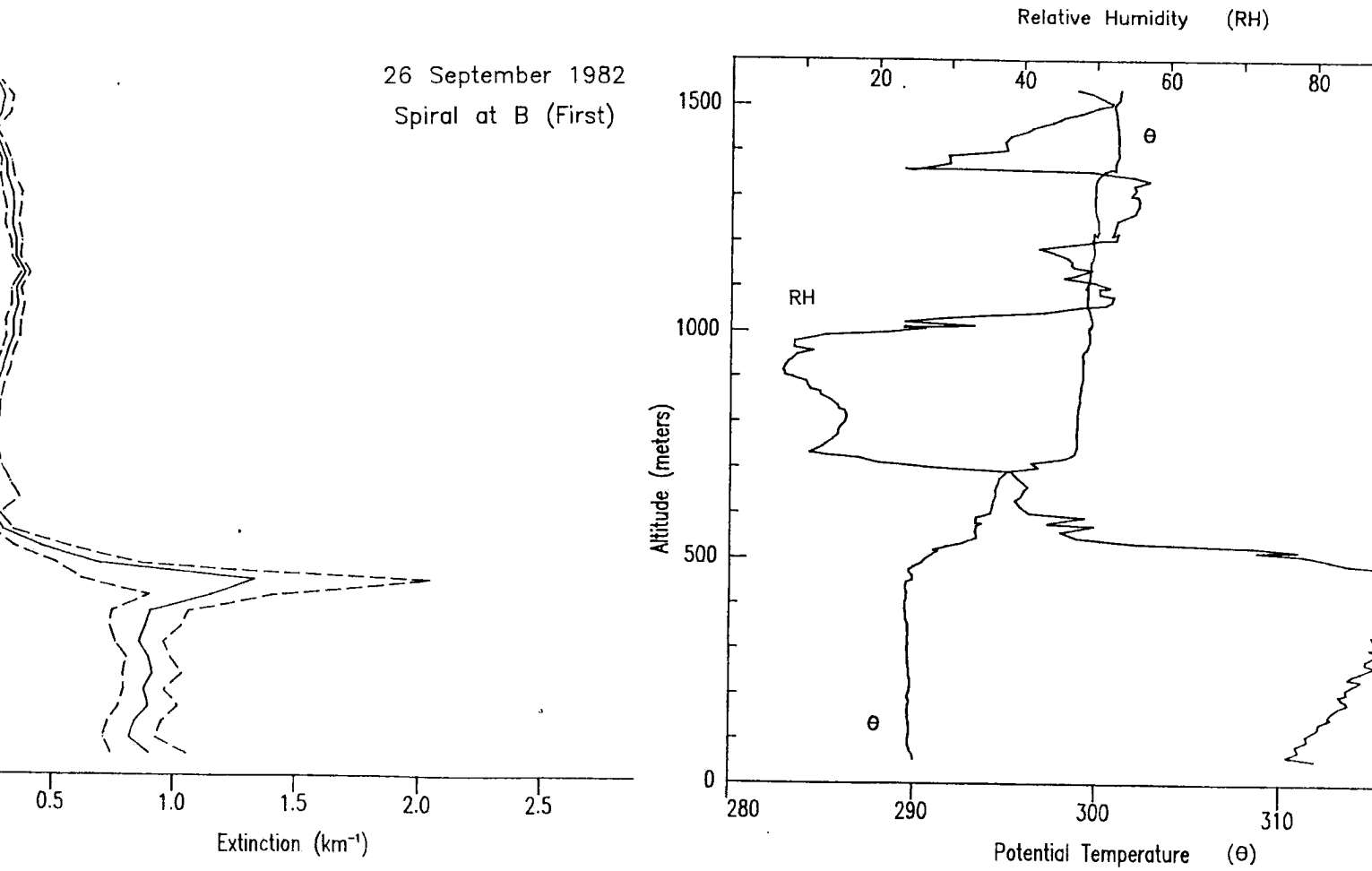

Figure C.11 **Same as Figure C.1 but for point B (first) on 26 September 1982.**

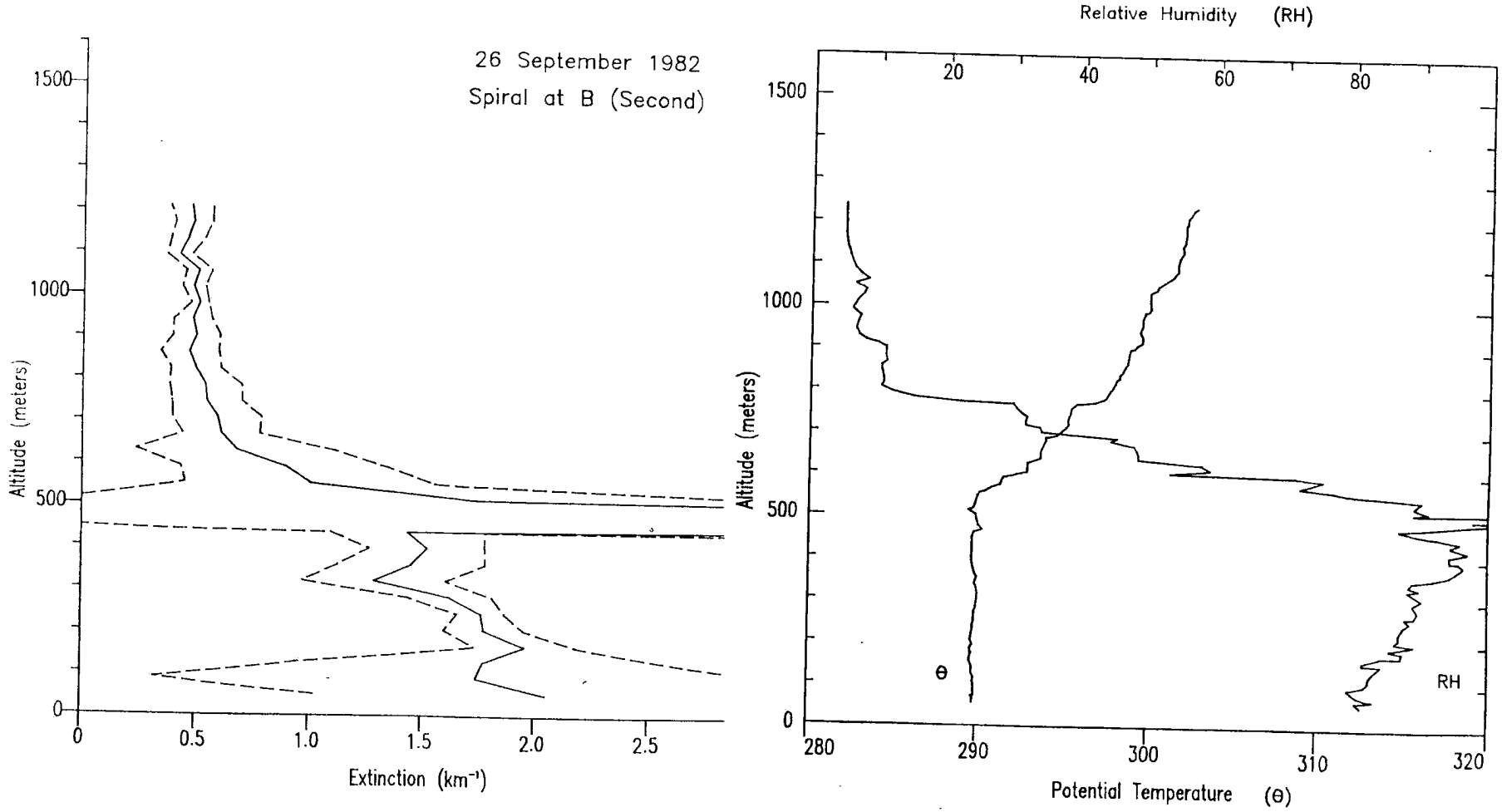

Figure C.12 **Same as Figure C.1 but for point B (second) on 26 September 1982.**

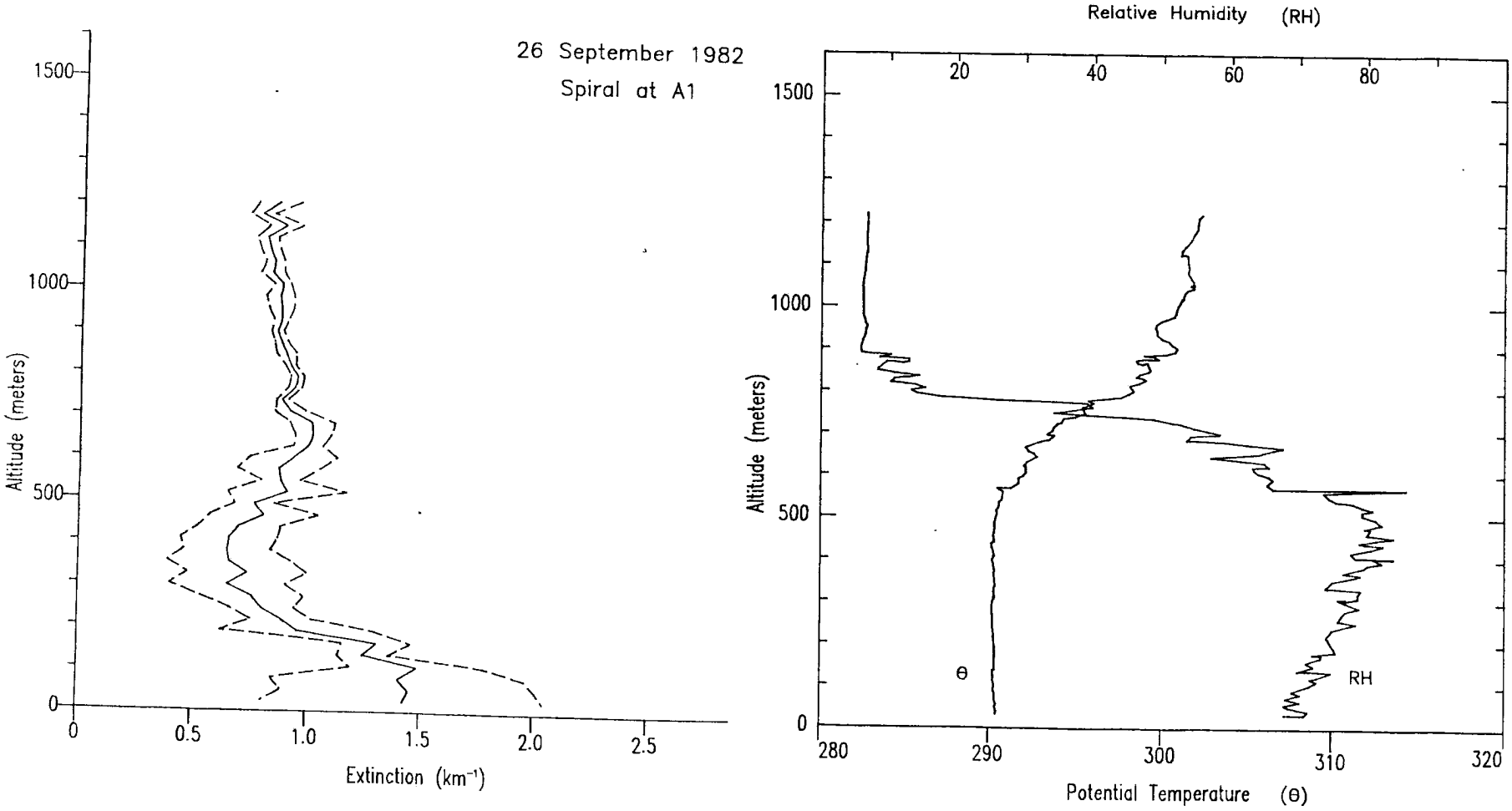

Figure C.13 **Same as Figure C.1 but for point A1 on 26 September 1982.**

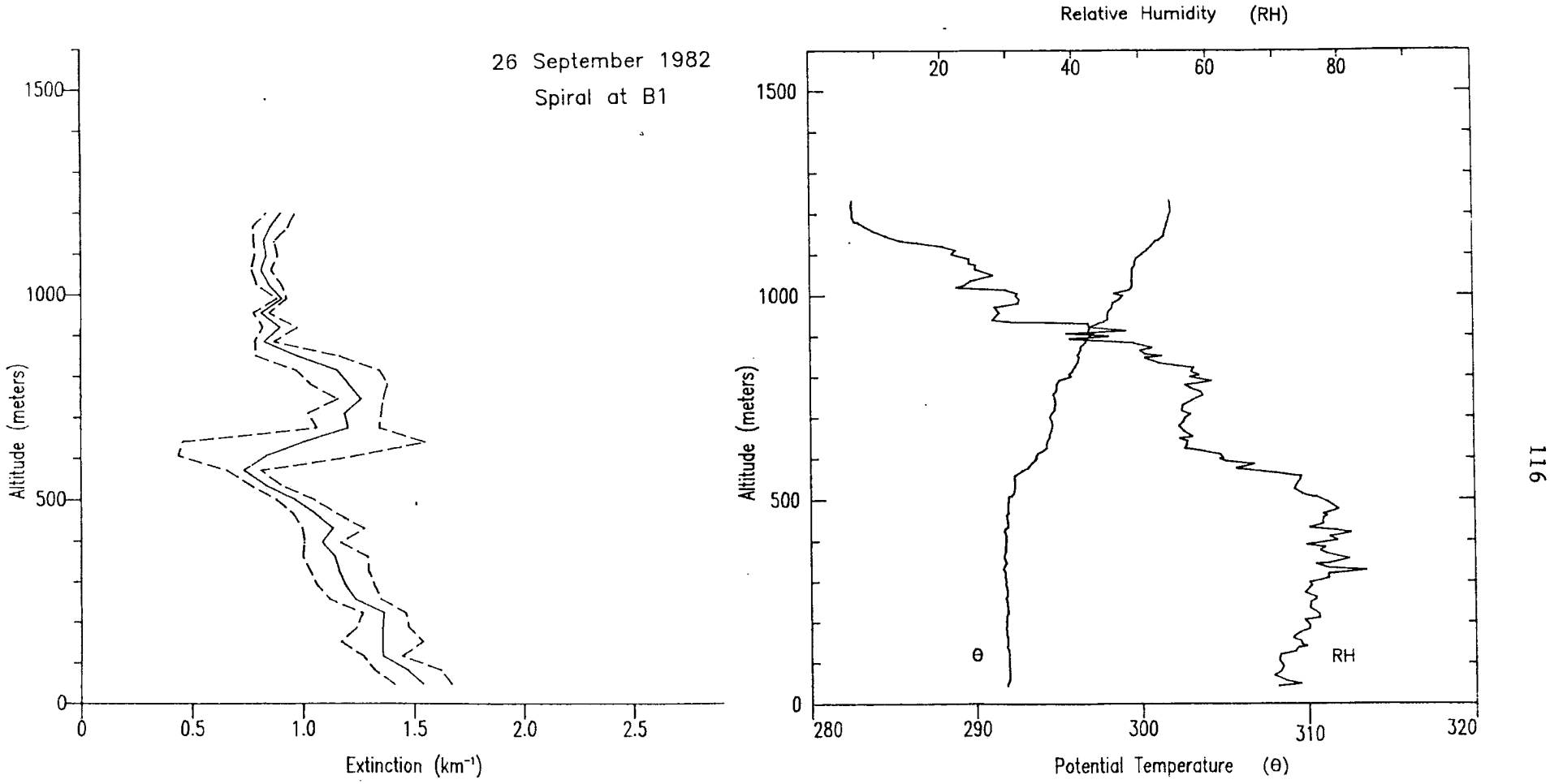

Figure C.14 **Same as Figure C.1 but for point B1 on 26 September 1982.**

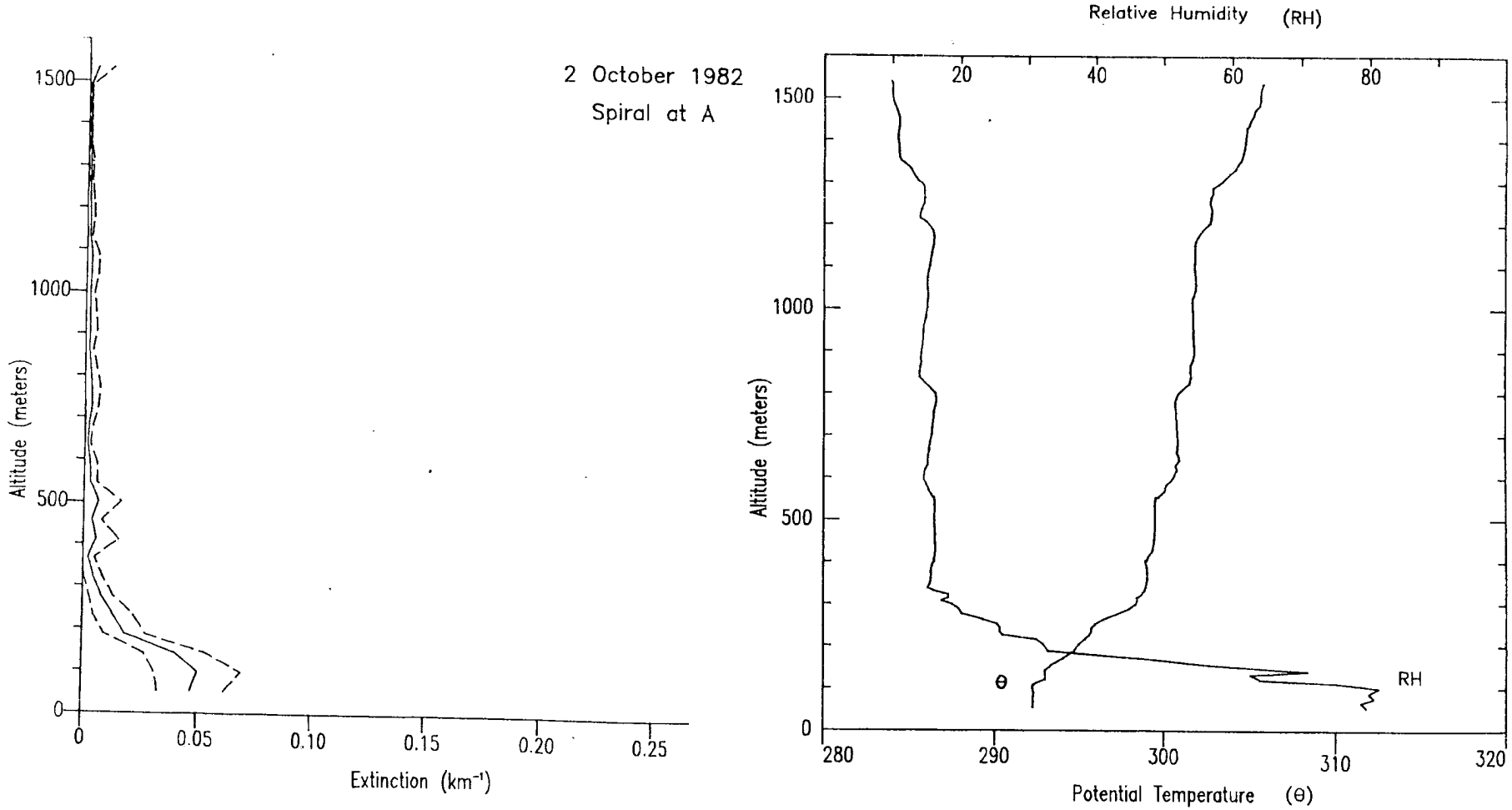

Figure C.15 **Same as Figure C.1 but for point A on 2 October 1982.**

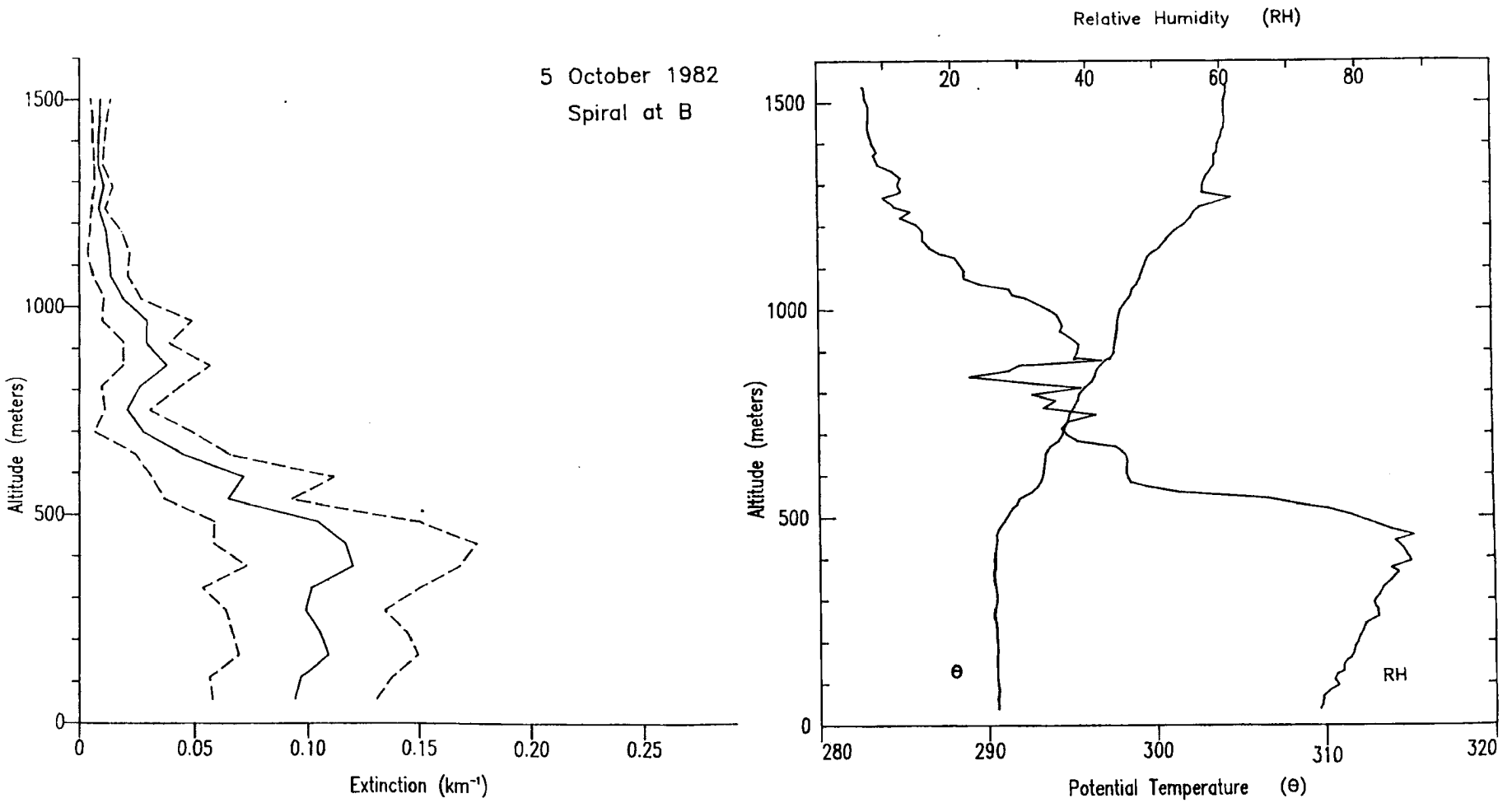

Figure C.16 Same as Figure C.1 but for point B on 5 October 1982.

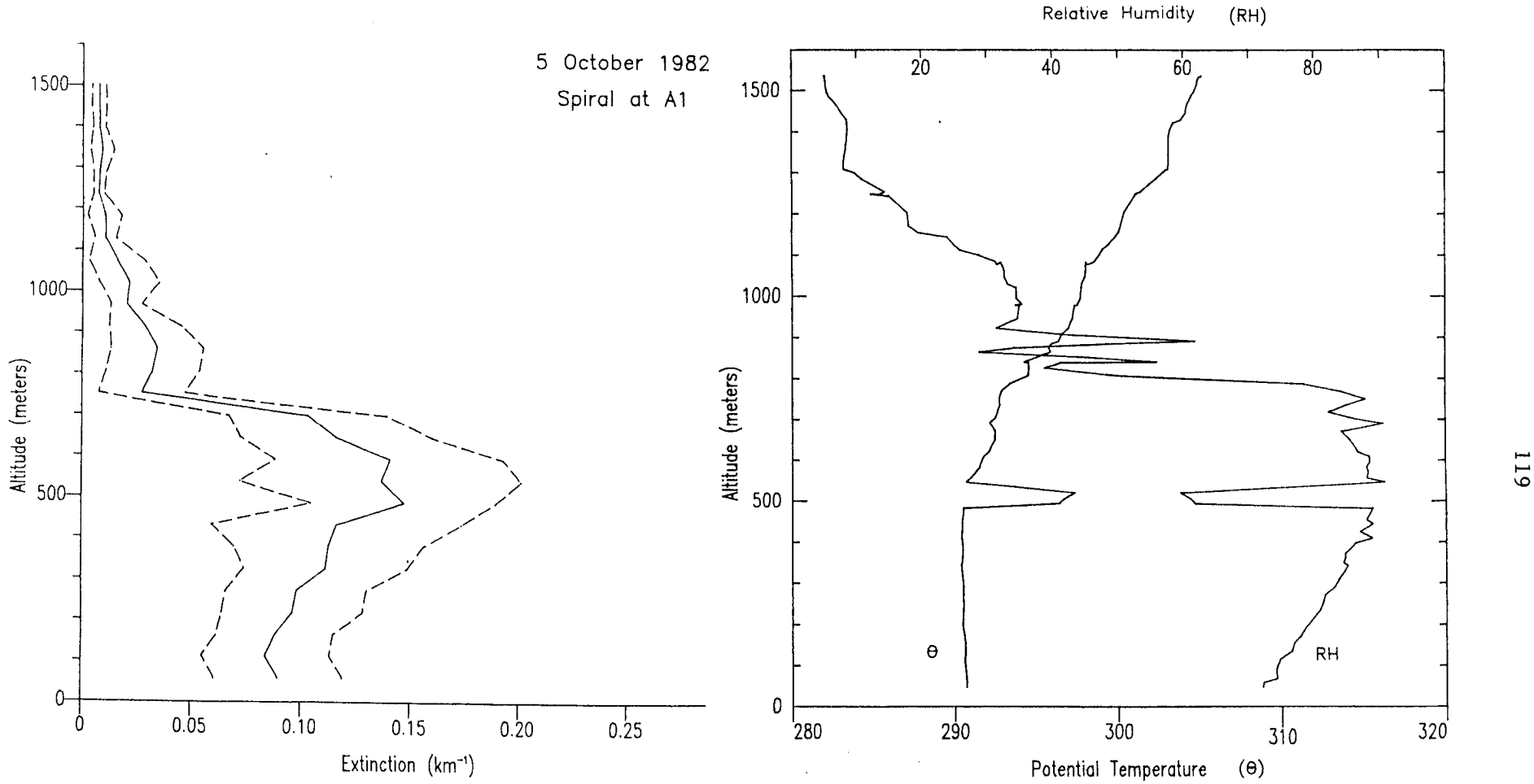

Figure C.17 **Same as Figure C.1 but for point A1 on 5 October 1982.**

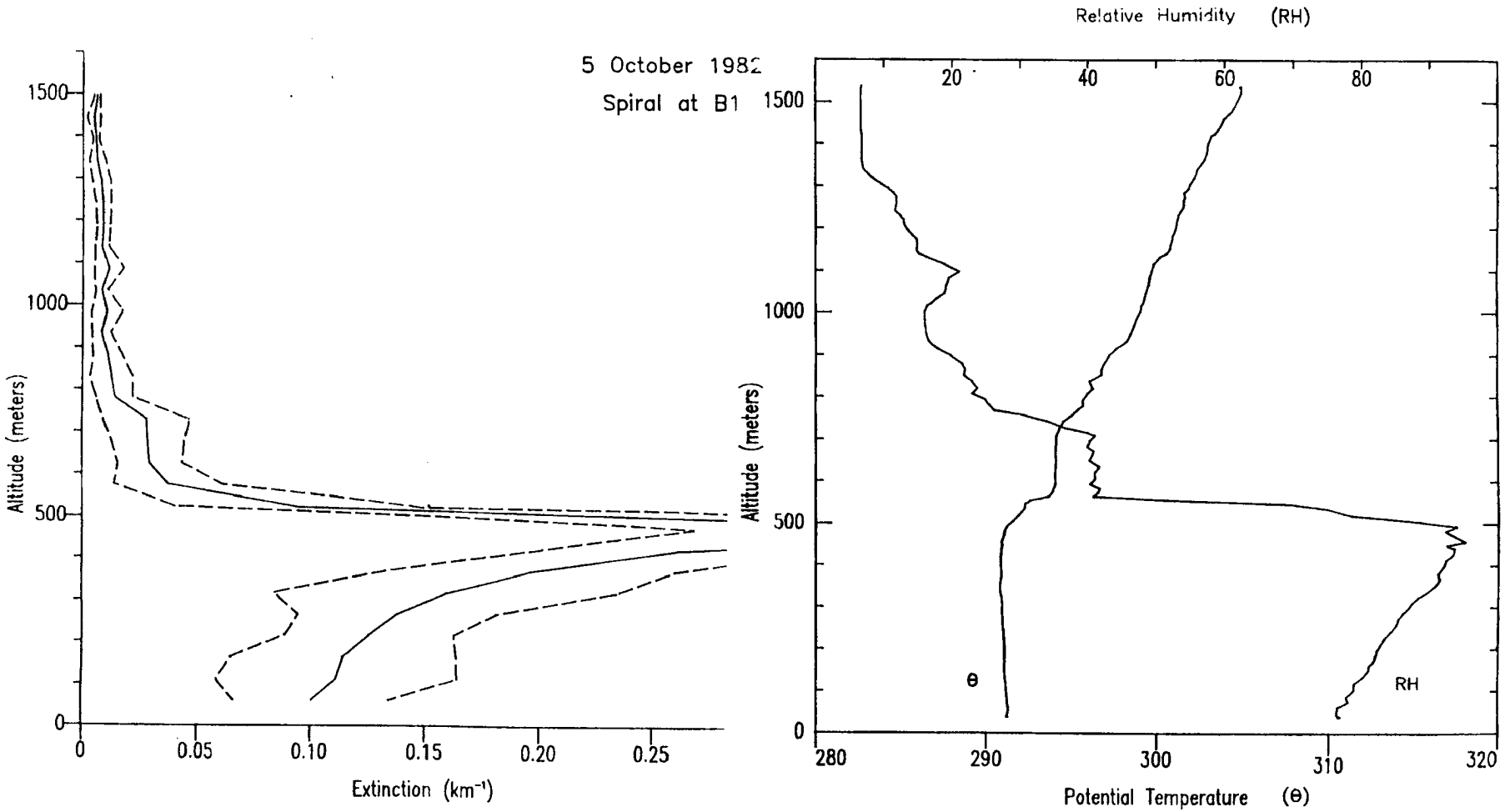

Figure C.18 **Same as Figure C.1 but for point B1 on 5 October 1982.**

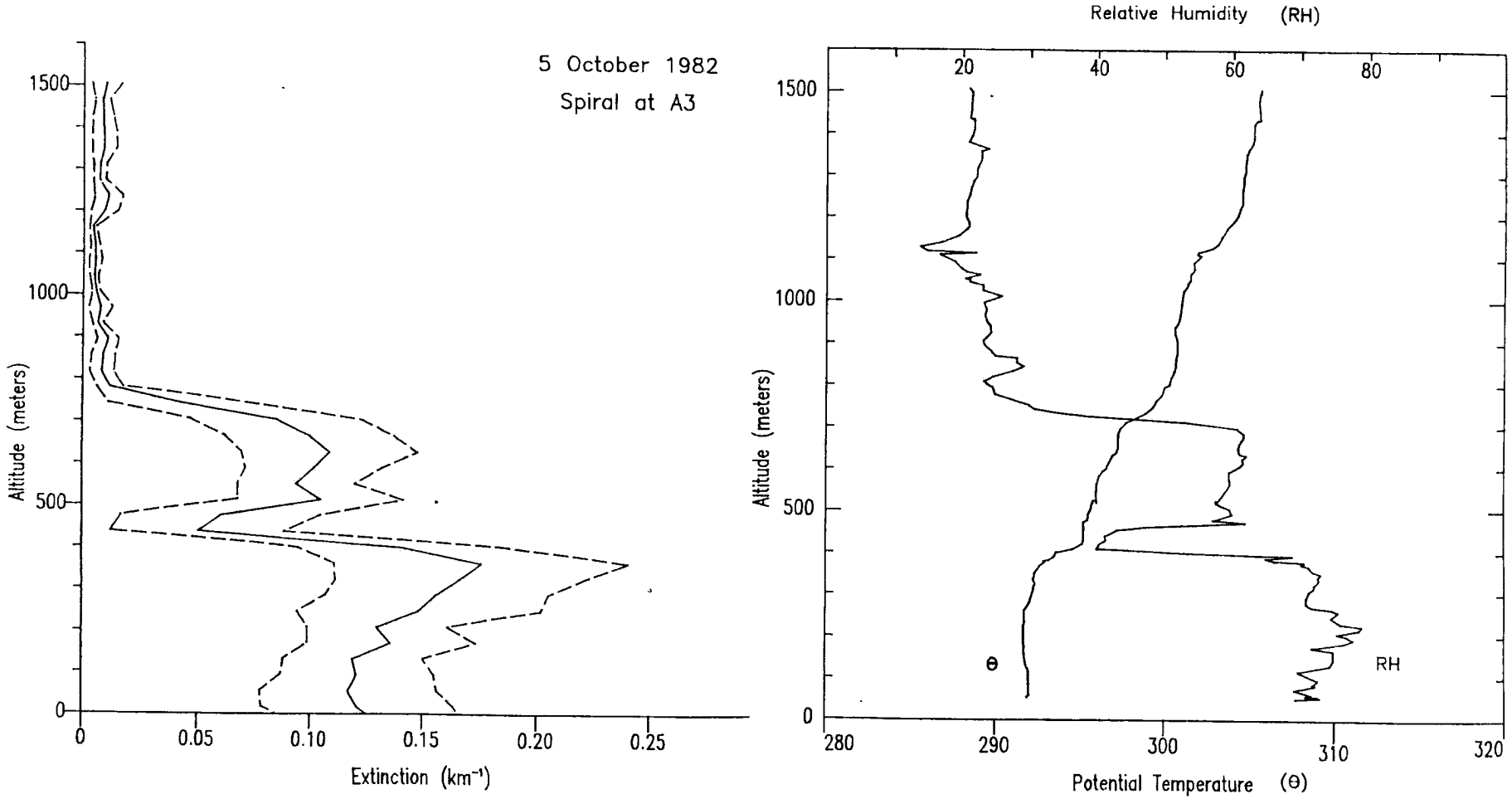

Figure C.19 Same as Figure C.1 but for point A3 on 5 October 1982.

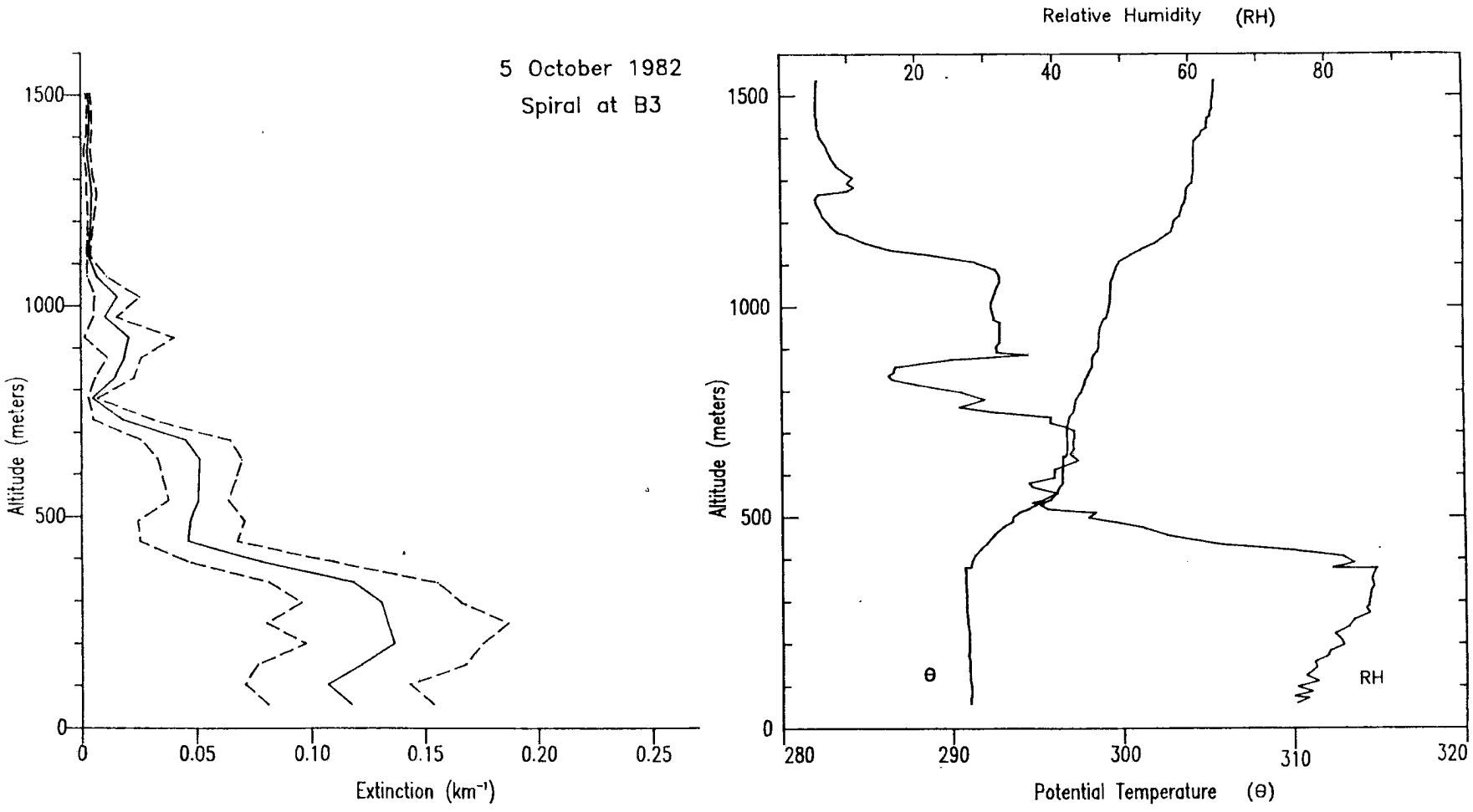

Figure C.20 **Same as Figure C.1 but for point B3 on 5 October 1982.**

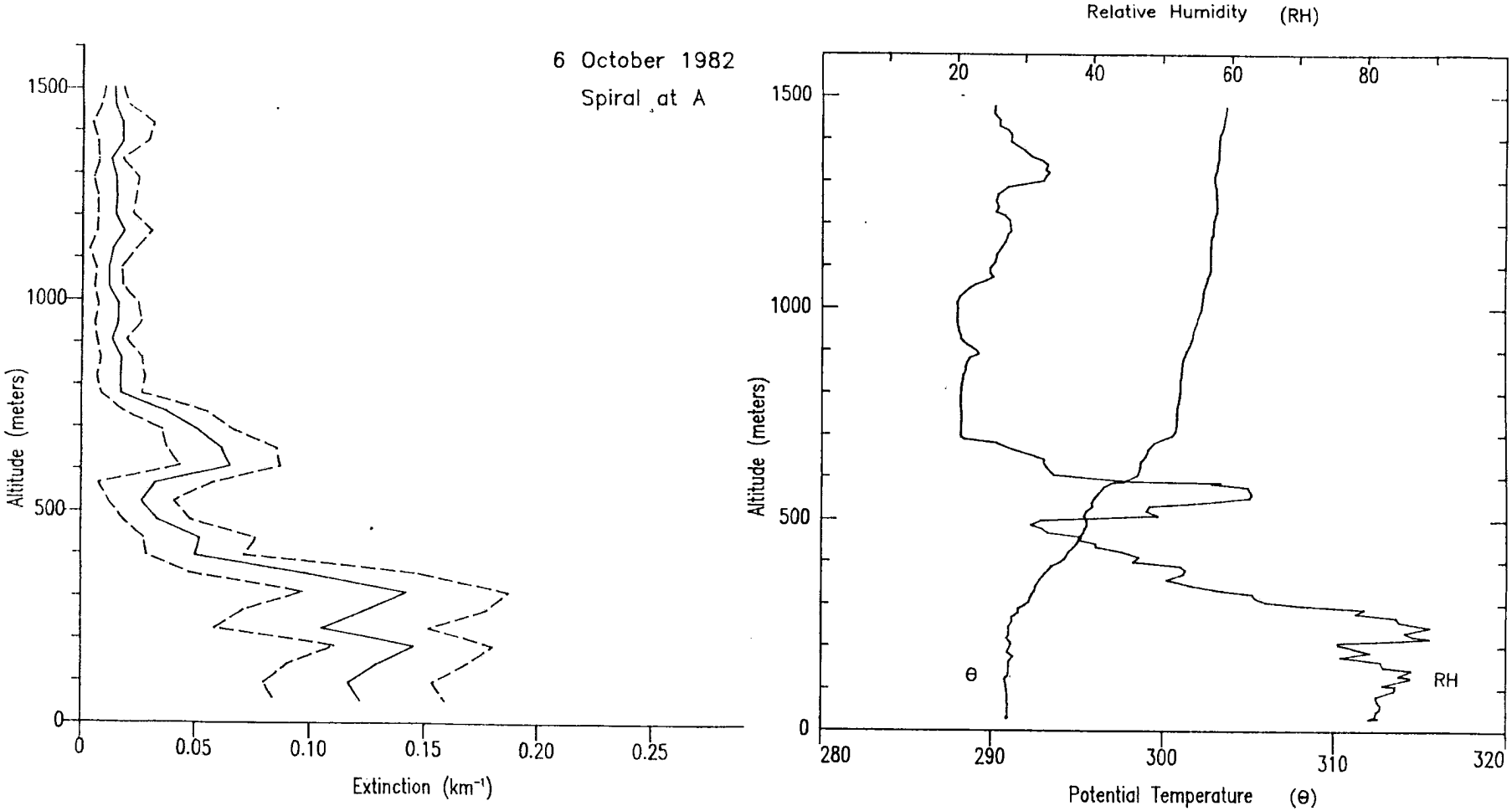

Figure C.21 **Same as Figure C.1 but for point A on 6 October 1982.**

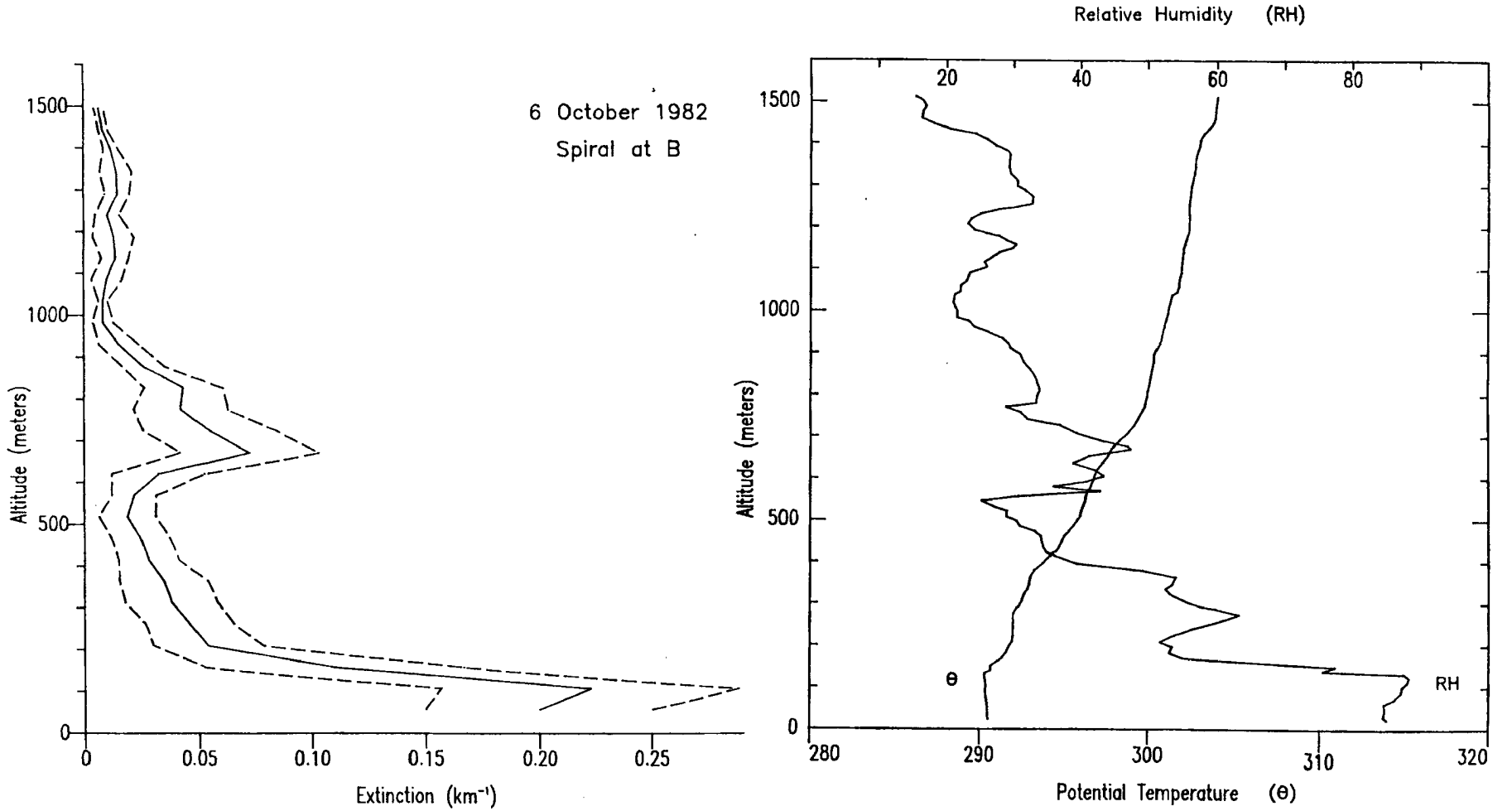

Figure C.22 **Same as Figure C.1 but for point B on 6 October 1982.**